5-20-2019

Nonlinear Optical Studies of Bulk and Thin Film Complex Materials

Joel E. Taylor

NONLINEAR OPTICAL STUDIES OF BULK AND THIN FILM COMPLEX MATERIALS

A Dissertation

Submitted to the Graduate Faculty of the
Louisiana State University and
Agricultural and Mechanical College
in partial fulfillment of the
requirements for the degree of
Doctor of Philosophy

in

Department of Physics and Astronomy

by
Joel Edward Taylor
B.A., Louisiana State University, 2013
August 2019

Acknowledgments

First and foremost, I would like to thank my advisor Dr. Ward Plummer. My path to a doctorate has been very unusual, but your support, patience, and guidance provided a pillar of perseverance, far more than anything I expected. From our interactions, I learned how to think deeply and critically, but at the same time think holistically with vision. You have taught me a lot about life beyond just physics and made a lifelong impression on both my personality and thought patterns. Graduate school is much more than just learning physics, it is about thinking and becoming a physicist. Having the opportunity to learn from someone of your prestige, integrity, and insight is invaluable. For that, I am forever grateful.

I would like to give special thanks to Dr. Rongying Jin and Dr. Jiandi Zhang. Without their support it would be impossible for me to conduct much of my research. From physics discussions to the holiday parties, I am very thankful for everything. Dr. Louis Haber deserves my deep gratitude. I have learned so much from our in lab discussions and collaborations. My sincerest respects go out to my graduate committee: Dr. Daniel Sheehy for his wonderful discussion both in class and in person, Dr. Harris Wong. for his helpful advice from my general exam to my thesis.

There have been many graduate students (and now post docs) along the way who have been paramount in discussions, both science and extracurricular related. Not only has our group formed a wonderful and friendly research environment, but many life-long friendships have also been created. It is truly a blessing to know I am connected to so many great people in both academia and industry all around the world. Looking back at our discussions (sometimes heated!) they ranged all topics from fantasy football to $5000 tuxedos to if it's better to be lucky or skilled. My one piece of advice for the following graduate students is to never forsake the afternoon coffee break. They single handedly strengthened the bonds of friendships, been amazing for stress relief, and provide a great platform to forge collaborations and share ideas.

Two special people deserve independent recognition responsible for my development of optical proficiency, Dr. Zhenyu Zhang and Dr. Kresimir Rupnik. Zhenyu taught me everything I know regarding working a laser lab. From my first task of making a straight line to your final days in the lab, you always taught me that "everything has a reason". Without you, I would not have the skills to continue independent development in the laser lab. I will always remember you in the highest regard. Throughout my graduate school experience, Dr. Rupnik has always been someone I can count on for laser discussion, equipment help, and assistance with the chemistry department. From the chiller used for the temperature-dependent experiments to the ultrafast beamsplitters, your contributions to the laser lab has been paramount in its success. It has been a pleasure to get to know you and work together.

My family and friends deserve special appreciation. Even though at times I am too busy to spend time together, my family and friends never hold it against me and are always available when I need them. It is a privilege to be have so many great people in my life.

Last but not least, my wife. You have sacrificed so much for me to be able to achieve my personal goals, much more than I ever ask of anyone. Your love and support has strengthened me rise above my own limits and kept me focused on the big picture. This doctorate is as much yours as it is mine.

Table of Contents

List of Figures

Abstract

Nonlinear optical studies of bulk and thin film materials provide a vast playground for physical and dynamical characterization. In this thesis, we have implemented experimental methods to probe novel phase transitions in single crystals using rotational anisotropic second harmonic generation (RASHG) and carrier dynamics in thin films with time-resolved pump-probe reflectivity. Furthermore, a novel low temperature ultra-high vacuum system coupled to nonlinear optics has been developed to extend lab capabilities. Doping $(Bi_{1-x}Sb_x)_2Se_3$ with antimony, the surface electronic reconstruction near $x = 80\%$ was identified with RASHG by deviations in the six-fold and three-fold polarization anisotropic patterns. Development of RASHG techniques to include temperature control and vacuum conditions lead to the exploration of the temperature-dependent electronic phase transition of $IrTe_2$. In $IrTe_2$ the surface electronic transition at $T_c \sim 280$ K measured by SHG is immediate and completes within the experimental temperature resolution. Comparing the surface temperate response to corresponding bulk measurements, the surface electronic transition occurs four times faster indicating the surface precedes the bulk transition. With time-resolved pump-probe reflectivity, an acoustic phonon mode in $La_{0.67}Sr_{0.33}MnO_3/SrTiO_3$ has been identified along with an anomalous low frequency oscillation unreported in similar systems.

Chapter 1
Introduction to Nonlinear Optics and Applications for Solid-State Science

1.1 Introduction to Nonlinear Optics

One of the most important technological advancements of the 20th century is the development of the laser. Lasers have become an integral part of nearly every industry and manufacturing process, as well as an essential tool for many scientific endeavors. Lasers offer exclusive optical properties compared to any other light source means, namely their monochromaticity, coherence, and intensity. Such properties are achievable through exploitation of a controlled population inversion and stimulated emission processes, allowing lasers to be the ideal tool for spectroscopic studies of material and molecular systems. Lasers offer many advantages as probes for solid-state materials because they are nondestructive and non-contacting.

Charles Townes[1] was the first to develop a successful self-sustaining stimulated emission source in 1954 using excited ammonia molecules in a resonant cavity [1]. The "maser", coined by Townes, marked the fulfillment of Einstein's 1916 prediction of stimulated emission emission. T. H. Maiman was the first to accomplish the feat in the infrared regime by using ruby as the optical pumping crystal producing continuous monochromatic light at a wavelength of 6943 Å [2]. Using Maiman's laser, the first measured second harmonic signal was generated by P. A. Franken in 1961 [3]. Figure 1.1 Franken's second harmonic spectra located at 3472 Å generated by shining 6943 Å through crystalline quartz. While by today's standards generating a second harmonic is trivial, Franken's measurement served as a spark igniting an entire field of nonlinear optics and creating a race for generating more intense radiation at shorter timescales.

[1] Charles Hard Townes was jointly awarded the Nobel Prize in Physics in 1964 "for fundamental work in the field of quantum electronics, which has led to the construction of oscillators and amplifiers based on the maser-laser principle".

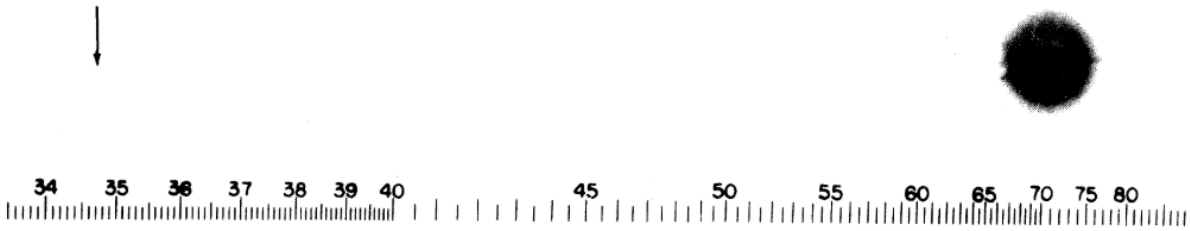

Figure 1.1: Reproduction of the second harmonic signal at 3472 Å generated by a ruby maser centered around 6943 Å. The scale corresponds to wavelength with ticks of 100 Å. Figure adapted from [3]

Normally when light strikes a medium, the resulting interaction can be described adequately by classical means. In the first order, these interactions refer to models laid out in the 19th century by Fresnel, Huygens, and Maxwell. The physics of these elementary laws lie grounded in the superposition principle. However when the incident light becomes powerful enough, i.e. a material's dielectric response becomes strong enough for the higher order terms to become nonnegligible, superposition breaks down producing a variety of frequency/wave mixing and multi-photonic effects. In order for nonlinear affects to become predominate for scientific measurements, strong electric fields only producible by lasers is necessary. As a rough estimate for the order of nonlinear effects, J. A. Armstrong and Nicolaas Bloembergen[2] et al [4] estimated the scaling ratio of n-th order multiphoton processes as $(E_{linear}/E_{multiphoton})^n$. From Bloembergen's estimation, if a medium's linear dielectric response is on the order of unity, then the second order correction will be roughly 10^{-12}, the third order 10^{-24}, and so on. Therefore, one can see that strong electric fields $\sim 10^{12}$ V/m, are essential for the higher order corrections to be detectable.

In 1985 Gérard Mourou and Donna Strickland[3] invented the modern standard for generation of ultrashort high intensity optical pulses called chirped pulse amplification [6]. Figure 1.2 outlines the chirped pulse amplification method. The process can be described as follows. First, optical pulses are created using an oscillator consisting of a Ti:sapphire

[2]Nicolaas Bloembergen was jointly awarded the Nobel Prize in Physics in 1981 "for their contribution to the development of laser spectroscopy".

[3]Gérard Mourou and Donna Strickland were jointly awarded the Nobel Prize in Physics in 2018 "for groundbreaking inventions in the field of laser physics" and "for their method of generating high-intensity, ultra-short optical pulses."

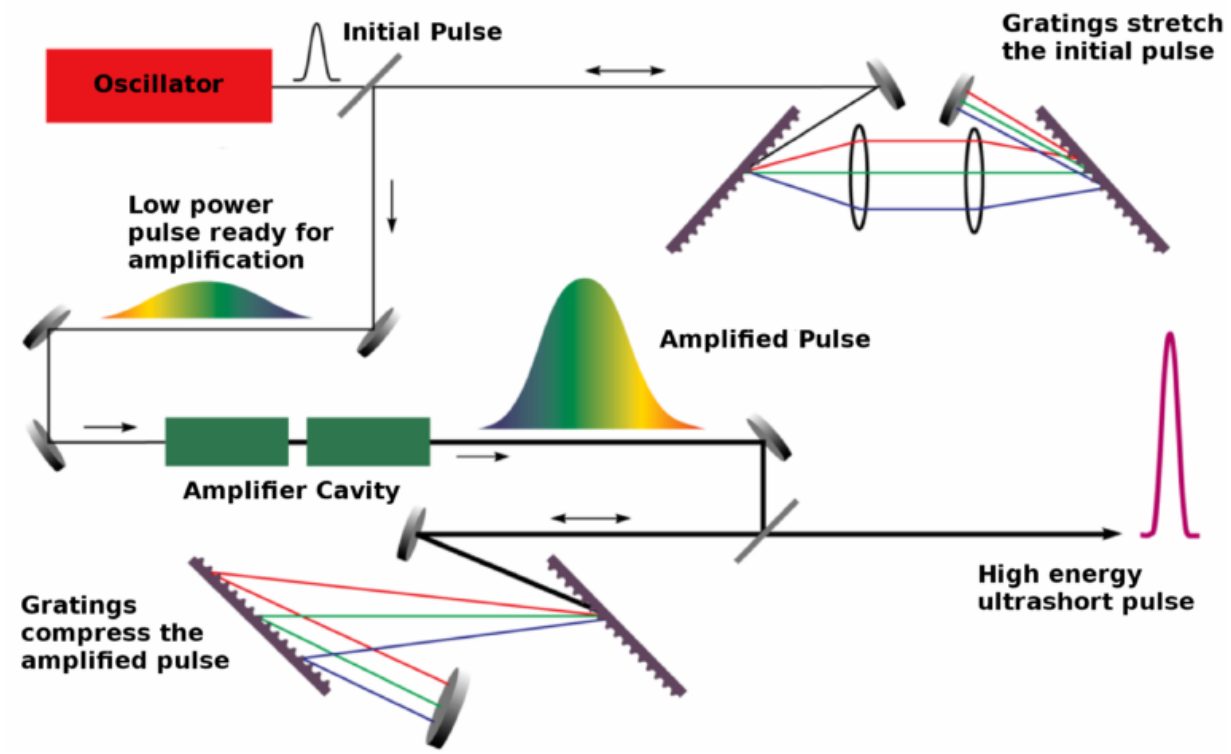

Figure 1.2: Chirped pulse amplification process. An Oscillator produces initial pulses which seed an amplifier cavity. To prep the pulses for amplification, first they are sent through a set of gratings to spectrally stretch the pulse shape. After being amplified in an amplifier cavity, the amplified pulses are recompressed using a set of gratings. The result of the amplification process is a high energy ultrashort pulse. Figure adapted from [5]

crystal gain medium pumped by a high power 532 nm laser. For a pumped Ti:sapphire crystal with a proper optical cavity geometry, Kerr-lens modelocking allows femtosecond pulse generation. Kerr-lens modelocking is the process by which intense light will become self-phase modulated and self focused in a gain medium producing Gaussian pulses. These initial short pulses serve as the amplifier seed where diffraction gratings spectrally stretch the pulse, increasing its bandwidth by a factor of a thousand and lowering the pulse intensity. By lowering the pulse power, energy can be safely added without damaging any optics. Stretched pulses then enter a power amplifier. Inside a power amplifier, the seed pulses become trapped in an optical cavity via polarization manipulation with Pockels cells. Once inside, they make multiple passes through a pumped gain medium (usually another Ti:sapphire crystal), each time growing in energy through the stimulated emission pro-

cess. Once the pulses reach sufficient energy they exit the cavity. A final set of diffraction gratings compress the amplified pulse, creating in a final pulse with massive peak energy compared to the initial.

There are many important multi-photon processes, each characterized by distinct frequency conversions and applications. Second order (two photon) processes include sum-frequency generation ($\omega_1 + \omega_2 = \omega_3$), second harmonic generation - a special case of sum-frequency generation ($\omega_1 + \omega_1 = \omega_2$), difference-frequency generation ($\omega_1 - \omega_2 = \omega_3$), and optical rectification. Of all the second order nonlinear processes, second harmonic generation (SHG) and sum-frequency generation (SFG) are the most prolific for surface studies because under specific material conditions SHG and SFG are directly related to surface properties. More details regarding surface specificity of SHG will be discussed in the following sections. SHG in particular, is an exceptionally versatile tool for understanding many fundamental macro- and microscopic properties. This thesis will serve as an example of manipulating the second harmonic response by changing variables such as temperature, sample azimuthal angle, and time delay. Although many examples of SHG will be covered, it does not scratch the surface of all the possibilities for the use of SHG as a measurement tool.

Both the fields of nonlinear optics and its coupling to modern surface science are relatively young when put in a historical context. Coinciding with the development of the laser in the 1960s and 1970s, modern ultra-high vacuum (UHV) technology was initially finding its identity. At the time, obtaining clean surfaces (by today's standards) was extremely difficult, pushing surface scientists towards improving vacuum technology. Additionally, the discovery of the transistor in 1947[4] and subsequent boom of the semiconductor and electronics industry together increased popularity and interest in vacuum technology and electron spectroscopic surface characterization techniques [7, 8]. As technology improved,

[4]William Bradford Shockley, John Bardeen, and Walter Houser Brattain were jointly awarded the Nobel Prize in Physics in 1956 "for their researches on semiconductors and their discovery of the transistor effect." John Bardeen is also the only person to win two Nobels in Physics, his second was jointly awarded in 1972 "for their jointly developed theory of superconductivity, usually called the BCS-theory."

rapid improvement of many probes lead to significant advancements of low energy electron diffraction, scanning tunneling microscopy [9], x-ray photoelectron spectroscopy [10], angle resolved electron spectroscopy, etc. At the current state, many of the aforementioned difficulties have been greatly reduced, and many new viable probes ranging from photons, electrons, neutrons, and ions have been established.

One of the most challenging problems in physics is probing electronic structure at buried interfaces, where structural and electronic mismatches often produce unique behavior. Recent examples include the two-dimensional electron gas at the interface of two insulating perovskites LAO and STO [11] and interface superconductivity [12]. High-resolution microscopy techniques such as transmission electron microscopy (TEM) or scanning tunneling microscopy (STM) are the standard for resolving atomic structure and morphology. However, TEM fails when there is significant inhomogeneity close to the interface and STM tunneling junctions do not penetrate to the interface. When applied to the cross-section, atomic-scale characterization can be obtained, but sample preparation for these methods inevitably damage the samples. Powerful surface diffraction methods such as low-energy electron diffraction (LEED) can not penetrate to the interface because the mean free path of the scattering is on the order of angstroms. X-ray spectroscopy is exactly the opposite and can provide deep penetration while being angle-resolved, but superimposes information from the entire bulk. Second harmonic generation, on the other hand, is capable of bypassing many limitations of scattering and microscopy methods while theoretically possessing monolayer resolution. Generally SHG is limited by optical penetration alone given a material has inversion symmetry (order of 10s to 100s of nm for visible radiation). SHG does provide many benefits for examining buried interfaces, but SHG does not have the ability to discriminate multiple second harmonic origins without special considerations. One particular challenge for SHG is superlattice heterostructures because the second harmonic will be a composition of the surface as well as each individual interface.

1.2 Introduction to Ultrafast Spectroscopy

Alongside the improvement of laser power over the years is the decrease in temporal pulse width. In the 1960s dye lasers were the first to achieve sub-picosecond pulse widths opening the door to probing ultrafast processes. Now, modern Ti:sapphire solid-state systems are able to achieve sub-10 femtosecond resolution, being able to fully capture carrier and lattice scattering events. Figure 1.3 demonstrates the average lifetimes of electronic carrier and lattice dynamics induced by optical pumping and characterizable with Ti:sapphire lasers [5]. Absorption of photons and carrier scattering occurs on the order of 10s of femtoseconds. As timescales increase, dynamics gradually shift from electrons to lattice. Using femtosecond pulses and probing across longer timescales, a complete mapping of electron-lattice dynamics can be resolved. From Figure 1.3, interactions between interatomic electrons and electrons in atoms/molecules is at the limit of Ti:Sapphire pulses motivating attosecond pulse generation as the next optical frontier for dynamics characterization.

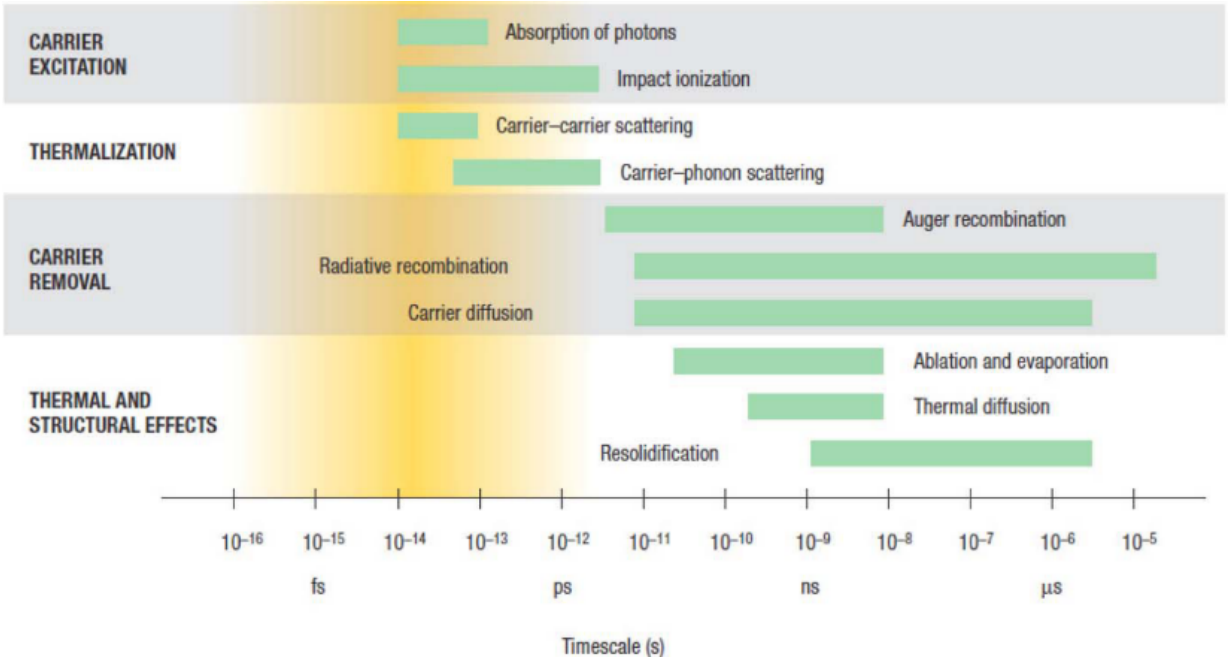

Figure 1.3: Schematic diagram of pump induced relaxation timescales. Fast timescales are dominated by electronic interactions while long timescales are lattice phenomenon. Figure adapted from Ref. [5]

Using a technique called ultrafast pump-probe spectroscopy, electron carrier and spin dynamics, lattice motion, and molecular dynamics can be characterized for surfaces, multilayers, and bulk. Figure 1.4, outlines the process of pump-probe spectroscopy. This method consists of two pulses, a pump and a probe, where the pump drives the system into an excited state (black dotted line) and a much weaker pulse takes a snapshot of the instantaneous decay towards the ground state, given by the red dots in snapshots 1-6. Initially before the pump arrives, the probe beam samples the state of the sample, getting a baseline before pumping (snapshot 1). The pump and probe then simultaneously strike the sample surface together (snapshot 2), causing a large change in the density of states. By convention, this time is called 'time-zero' signifying the beginning of dynamical processes. Following initial excitation, further delay in the probe pulse arrival allows snapshots of the relaxation all the way until it reaches the initial ground state (snapshot 6). As long as the time difference between each probe pulse is sufficiently smaller than the decay process, a complete mapping of the decay can be resolved.

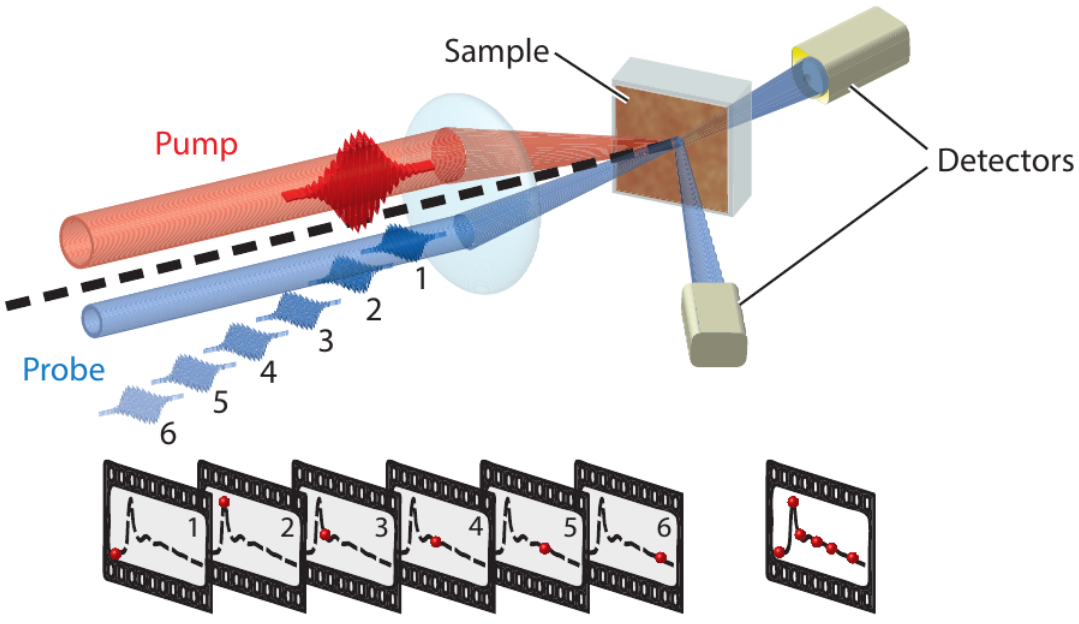

Figure 1.4: Schematic description of pump-probe spectroscopy. A pump drives a sample into an excited state. Six independent and spaced out probe pulses capture a 'snapshot' of the relaxation state. Figure adapted from Ref. [13]

1.3 Second Harmonic Generation as an Essential Surface Spectroscopic Technique

For a rigorous proof please refer to the texts by Shen [14], Bloembergen [15], and Boyd [16]. Following is an overview of essential assumptions and arguments from these sources. The macroscopic interaction of light and matter is governed by Maxwell's equations.

$$\nabla \cdot \mathbf{B} = 0 \tag{1.1}$$

$$\nabla \cdot \mathbf{D} = \rho \tag{1.2}$$

$$\nabla \times \mathbf{E} = -\frac{\partial \mathbf{B}}{\partial t} \tag{1.3}$$

$$\nabla \times \mathbf{H} = \frac{\partial \mathbf{D}}{\partial t} + \mathbf{J} \tag{1.4}$$

To use these equations, we must make a few basic assumptions. First, since we are only interested in a bound charge response to an external field, there are no free charges, no free currents, and the material is nonmagnetic: $\rho = 0$, $\mathbf{J} = 0$, and $\mathbf{B} = \mu_0 \mathbf{H}$. For a plane wave monochromatic electric field of the form $\mathbf{E} = Ee^{-i(\mathbf{k}\cdot\mathbf{r}-\omega t)}$, we assume $\mathbf{k} \cdot \mathbf{r} \ll 1$. Second, the media in question is a lossless and dispersionless media. Under application of these assumptions the linear polarization P can be derived from the Maxwell's equations, given the displacement field $\mathbf{D} = \epsilon_0 \mathbf{E} + \mathbf{P}$.

$$\mathbf{P} = \chi \mathbf{E} \tag{1.5}$$

As evident in Eq. 1.5, the polarization can be understood by the susceptibility χ and a time-varying electric field $\mathbf{E}$. When $\mathbf{E}$ becomes large (i.e. into the nonlinear regime), we can Taylor expand the polarization $\mathbf{E}$ yielding a multi-order response.

$$\mathbf{P}_k = \epsilon_0 \left(\chi^{(1)}_{ik} \mathbf{E}_i + \chi^{(2)}_{ijk} \mathbf{E}_i \mathbf{E}_j + \chi^{(3)}_{ijkl} \mathbf{E}_i \mathbf{E}_j \mathbf{E}_k + ... + \chi^{(n)} \mathbf{E}^{(n)} \right) \tag{1.6}$$

$$= \mathbf{P}^{(1)} + \mathbf{P}^{(NL)} \tag{1.7}$$

All higher orders above the first order are considered nonlinear optical responses, each with a unique susceptibility intrinsic to the material. The simple result in Eq. 1.6 is consistent with the phenomenological derivations by Mizrahi and Sipe [17]. In the phenomenological model, a polarized dipole sheet is placed infinitesimally above a slab to represent the source of the second harmonic signal. The resulting nonlinear source is radiated both into vacuum as well as into the slab and reflected. The response from the slab is encoded in χ^s and the slab properties are given by complex Fresnel coefficients.

Let's focus the attention to the second order response under the electric dipole approximation (i.e. second order contribution is much larger than the higher order terms). If we Fourier transform Eq. 1.6 with respect to a monochromatic plane wave we obtain the generalized form for the frequency dependent second harmonic polarization ($P_i(2\omega)$) or second harmonic generation (SHG).

$$P_i(2\omega) = \chi^{(2)}_{ijk} E_j(\omega) E_k(\omega) \tag{1.8}$$

From Eq. 1.8 SHG is a two photon absorption process where two identical photons of frequency ω are absorbed in a medium possessing a nonzero $\chi^{(2)}_{ijk}$ creating an electric dipole emitting a third photon of frequency 2ω. Unlike typical two-photon absorption into an excited state, SHG is a virtual state absorption. A virtual state, first theorized by Maria Göppert-Mayer in 1931[5], is a short-lived imaginary state described by stationary states that are not eigenstates of the systems Hamiltonian. A visual description of this process is shown in Fig. 1.5 where two 1.55 eV (ω_1 and ω_2) photons are absorbed by a crystal with second order susceptibility $\chi^{(2)}_{ijk}$ into virtual states represented by dashed lines. A third frequency coupled photon ω_3 is generated.

[5]Maria Göppert-Mayer was jointly awarded the Nobel prize in Physics in 1963 "for their discoveries concerning nuclear shell structure."

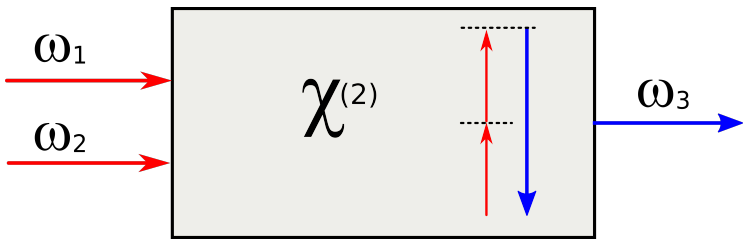

Figure 1.5: Second harmonic generation absorption diagram. Two photons of frequency ω combine through a virtual state excitation and decay to generate a single photon of frequency 2ω.

The intensity of the generated second harmonic signal can be obtained by taking the square of the second harmonic polarization.

$$I(2\omega) \propto |\mathbf{P}^{(2)}(2\omega)|^2 \tag{1.9}$$

For spectrally insensitive measurement tools such as a photomultiplier tube or photodiode, power scaling differences between the second harmonic ($\propto E^4$) and linear responses ($\propto E^2$) are important to determine the origin of the signal. The difference in power scaling is extremely useful to ensure proper fundamental light filtering because SHG as a frequency doubling process is largely inefficient and often buried under the fundamental field signal. Some materials such as beta barium borate (BBO) crystals are optimized for conversion efficiency due to near perfect phase matching, large nonlinear coefficients, and wide transparency windows. In outlier cases, 80%+ power conversion is possible using standing-wave resonators [18].

Coherence of the second harmonic is an important concept for bulk materials. As the fundamental field travels into the bulk, it's wavelength becomes slightly shifted due to the index of refraction. For optical pulses the group velocity becomes broadened and slowed, resulting in a naturally occurring phase difference between the generated second harmonic. Fundamental coherence length l_c has been worked out by P. D. Maker et al. in 1962, as being inversely proportional to the phase mismatch between the first and second order

wavevector [19].

$$l_c = \frac{2\pi}{\Delta k} = \frac{\lambda}{4(n^{(2\omega)} - n^{(\omega)})} \tag{1.10}$$

An example of phase matching in nonlinear crystals is given by Figure 1.6 [20]. At $z = 0$ the fundamental pulse hits the surface of the crystal and propagates into the bulk. Curve C represents a the second harmonic intensity $I_{2\omega}$ for a perfect nonphase-matched crystal. The second harmonic intensity oscillations between a maximum and minimum at integer multiples of the coherence length. Perfect phase-matching is demonstrated in curve A, where the intensity of the second harmonic grows exponentially as the fundamental field propagates and there is no visible destructive interference (oscillatory pattern).

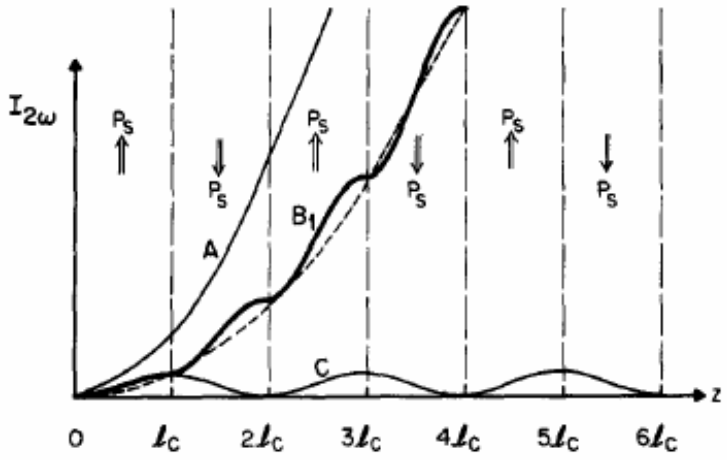

Figure 1.6: Second harmonic intensity $I_{2\omega}$ generated through a nonlinear crystal under the following conditions: A - perfect phase-matching, B - partial phase-matching, C - perfect nonphase-matching. Figure adapted from Ref. [20]

One crucial aspect of Eq. 1.6 is the composition of even and odd functions. Under inversion, odd rank tensors (i.e. $\chi^{(2)}$, $\chi^{(4)}$, etc.) have even parity and are invariant under symmetry operations, implying zero contribution under these conditions. For example, if we examine the second order polarization for an electric field of opposite sign, symmetry

operations implies that the polarization sign must flip in accordance,

$$-P_i(2\omega) = \chi^{(2)}_{ijk}(-E_j(\omega))(-E_k(\omega)) = \chi^{(2)}_{ijk}E_j(\omega)E_k(\omega). \tag{1.11}$$

The only way Eq. 1.11 can be equal to Eq. 1.8 is if $\chi^{(2)}_{ijk} = 0$. When this occurs, the leading contributing term is the bulk quadrupole $\chi^{(3)}$, albeit the intensity from this term is much less than the surface dipole. This result is the entire basis for surface and interface studies using nonlinear optical techniques. For materials that possess inversion symmetry (centrosymmetric), second harmonic can not be generated from the bulk. The relationship between symmetry and the second harmonic will be discussed in more detail in the following section.

1.4 Symmetry and Applications for Physical Property Determination

As demonstrated in the previous section, symmetry is the fundamental consideration for application of second harmonic generation as a surface and interface probe. Depending on the crystalline structure and magnetic ordering two symmetries are relevant, one is the crystalline point group symmetry and the other being time-reversal symmetry (TRS). For structures to possess inversion symmetry, the structure must be identical about a unit cell or molecular center. A beautiful example is shown for the cubic structure for $SrTiO_3$ (STO) in Fig. 1.7(a) ($Pm\bar{3}m$ space group). For ABO_3 materials the A site ion, in this case the green strontium, forms the center of the unit cell surrounded by eight octahedras. All the octahedra are centrosymmetric with respect to the A site. Each octahedra has a central B site ion (blue titanium) surrounded by 6 red oxygen anions, all individually centrosymmetric about themselves.

Out of the seven crystal systems, group theory defines a total of 32 point group symmetries and nearly one third (11) are centrosymmetric. For centrosymmetric point groups there is zero bulk second harmonic signal and the entirety of the second harmonic signal comes from regions of broken symmetry. Symmetry can either be broken at the surface or

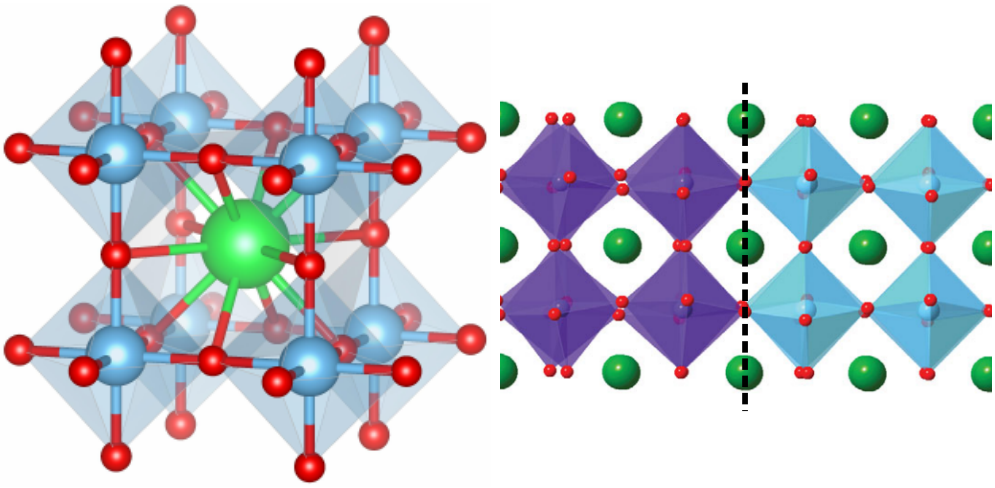

(a) (b)

Figure 1.7: (a) $SrTiO_3$ unit cell with inversion symmetry. (b) Noncentrosymmetric interface of two centrosymmetric materials. Black dashed line indicates the interface. Figure adapted from Ref. [21]

at the interface of two centrosymmetric material (see Fig. 1.7 (b)) making SHG capable of probing electronic structures of buried interfaces. Examples of broken symmetries probed by SHG in this thesis include interfaces of thin film perovskite heterostructures and surfaces of dichalcogenides and topological insulators.

How can we interpret a second harmonic signal? Neumann's principle is a famous crystallographic precept stating the macroscopic physical properties of a system exhibit at least the point group symmetry [22]. Consequently, the tensor $\chi^{(2)}_{ijk}$ must mirror the inherent crystalline and point group symmetries of the lattice. In general Neumann's principle is a good rule of thumb, although some materials such as those possessing nematic phases are exceptions. Depending on the symmetry of the centrosymmetric point group, $\chi^{(2)}_{ijk}$ can be simplified according to the allowed tensor elements for a given symmetry. Returning to STO (shown in Fig. 1.7(a)) application of the surface C_{4v} point group reduces $\chi^{(2)}_{ijk}$ from 27 independent elements to only four tensor elements: $xzx = yzy, xxz = yyz, zxx = zyy, zzz$. Another important simplification is the Kleinman condition [23]. If the frequency of incident photons is much less than the material's smallest resonant frequency, the nonlinear susceptibility tensor becomes independent of frequency. When Kleinman's symmetry is

valid, we can use contracted notation (d_{im}) to reduce the number of elements from 27 to 18, since jk is symmetric about the last indices.

$$d_{ijk} = \frac{1}{2}\chi^{(2)}_{ijk} = d_{im} \tag{1.12}$$

$$\rightarrow \quad jk: 11 \quad 22 \quad 33 \quad 23,32 \quad 31,13 \quad 12,21 \tag{1.13}$$

$$\rightarrow \quad m: 1 \quad 2 \quad 3 \quad 4 \quad 5 \quad 6 \tag{1.14}$$

Each element in the second order susceptibility tensor uniquely contains (before symmetry simplification) directionally dependent information about the surface relative to the crystalline axis. By manipulating the fundamental field polarization, we can tune the electric field to align with either the in-plane or out-of-plane tensor elements. Conventionally in optics, P polarized light is defined as out-of-plane, or parallel to the surface normal while S polarized light is defined at in-plane, or perpendicular to the surface normal (See Fig. 1.8). Snell's Law mandates the reflection angle and polarization relative to the surface normal are conserved. Azimuthally rotating the sample under a constant radiation alters the direction of the susceptibility tensor elements with respect to the fundamental field. The output is an isotropic or anisotropic second harmonic response depending on the electronic point group symmetry. Usually, anisotropic SHG take the form of two-fold, three-fold, etc. curves seen throughout this thesis.

Sometimes, for materials with highly correlated electrons, symmetries of the charge/orbital and spin are not the same as the lattice. When these anisotropies break the lattice symmetry it is referred to as a nematic phase. Often times, nematicity can be observed in high T_c superconducting systems [24], although the relation between the a nematic phase and superconductivity are still largely unexplored. Recently in superconducting $Cd_2Re_2O_7$, Harter et al. have used SHG to identify and temperature-dependent electronic nematic phases transition T_n. Below T_n, two bulk order parameters emerge, the lattice-E_u and a multipolar nematic phase-T_{2u}, and one was modeled to drive the lattice distortion.

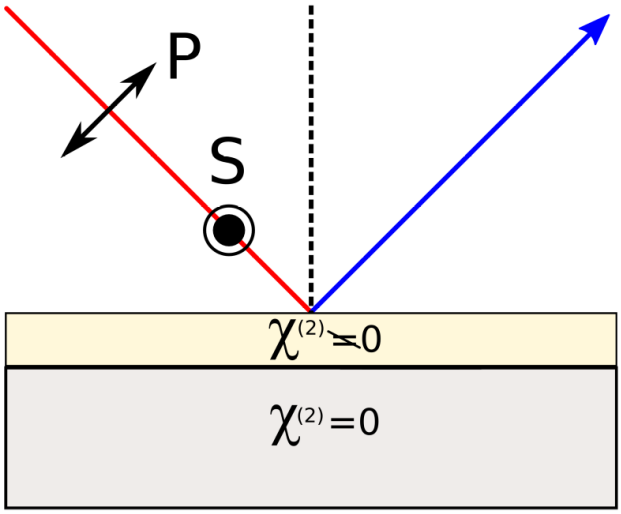

Figure 1.8: Second harmonic generation polarization geometry. P polarization aligns the fundamental electric field with tensor elements directed out-of-plane. S polarization aligns the fundamental electric field with tensor elements directed in-plane. By rotating a sample about the sample azimuth (black dashed line) directionally dependent nonlinear susceptibility tensor elements are activated. Second harmonic generation (blue arrow) is only generated in regions of broken symmetry near the surface $\chi^{(2)}_{ijk} \neq 0$.

The importance of this study highlights the strengths of SHG as a characterization tool for identifying dissimilar lattice electronic responses.

Noncentrosymmetric space groups, including polar or chiral materials will yield nonzero, and often significant second harmonic bulk responses compared to the surface counterpart. In many cases, materials can undergo centrosymmetric to noncentrosymmetric transitions with a second harmonic signature of a large intensity increase. Ferroelectrics are a prime example of such phenomena because all ferroelectrics are noncentrosymmetric due to the permanent electric dipole present in the unit cell. Such phenomena are elucidated in Figure 1.9 where cooling $BaTiO_3$ single crystals incites a phase transition into a ferroelectric phase below $T_c \approx 125°$ [25]. Intensity differences of noncentrosymmetric and centrosymmetric second harmonic generation originates from additional contributions from second order susceptibility tensor elements. For $BaTiO_3$ thin films applying bi-axial in-plane strain through lattice growth mismatch, the ferroelectric transition temperature can be shifted upwards by 300 K compared to the single crystal transition temperature (blue curve in Figure 1.9) [25].

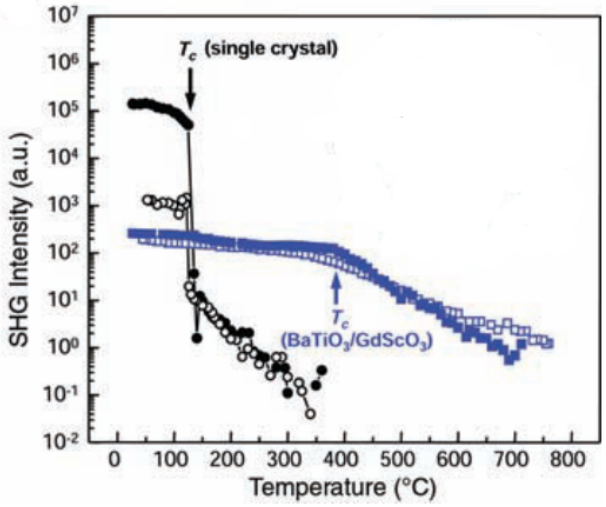

Figure 1.9: Second harmonic generation intensity as a function of temperature for $BaTiO_3$ single crystals (black curve) and in-plane strained thin film (blue curve). Transition into the ferroelectric phase is marked T_c. Figure adapted from [25]

For materials with ferromagnetic (FM) ordering, time-reversal symmetry is broken, leading to magneto-optical second harmonic generation studies (MSHG). Usually when TRS is broken, a newly activated $\chi^{(2)}_{(mag)}$ term, originating from magnetic dipoles in the system will additively impact the total second harmonic signal $\chi^{(2)}_{(tot)}$ Eq. 1.15 [26]. The total second harmonic can now be described as,

$$\chi^{(2)}_{(tot)} = \chi^{(2)}_{(cry)} + \chi^{(2)}_{(mag)} \tag{1.15}$$

When polarized light interacts with a magnetically ordered material aligned, the magnetic dipoles produce a torque which rotates the output SHG polarization, called the magneto-optical Kerr effect. A schematic of this interaction is demonstrated in Figure 1.10 [27]. Electric field polarization $\mathbf{P}$ couples to the net magnetic moment $\mathbf{M}$ and created a toroidal torque, $\mathbf{P} \times \mathbf{M} = \mathbf{T}$. Torque affects the second harmonic polarization by rotating it an angle Θ from the original polarization direction and can be measured in the second harmonic as a phase shift of the analyzer angle. The degree of the phase shift, or Kerr rotation angle, detected by SHG can be directly related to the magnetic field strength. Through changes in the SHG Kerr rotation angle, interface magnetism and electronic dead layers

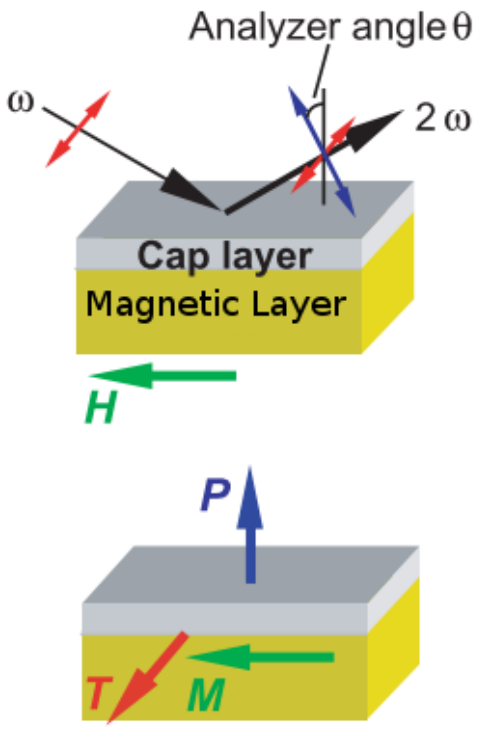

Figure 1.10: Magneto-optical light-matter interaction. Top: Fundamental field of energy $\hbar\omega$ and polarization (red arrows) interact with a magnetic layered material in applied field **H**. The second harmonic polarization (blue arrow) is rotated by an angle Θ. Bottom: Polarization **P** couples to internal field **M** creating a toroidal moment **T**. Figure adapted from [27]

have been identified [27]. At the boundary between FM and antiferromagnetic ordering, the hard magnetization of the AFM pins the FM layers close to the interface, also known as exchange bias. Exchange bias shifts the magnetic hysteresis loop off the zero field position. Interface exchange bias can be difficult to detect for linear bulk magnetic characterization techniques like magneto optical Kerr effect (MOKE). For Fe/MgO interfaces, SHG was able to identify exchange bias at the interface (Fig. 1.11(a)), which was buried by corresponding linear magnetic MOKE measurement (Fig. 1.11(b)) [28]. Such studies demonstrate the versatility and power of MSHG for interface magnetic responses. Although this serves as a brief introduction to MSHG, they will not be conducted in this thesis.

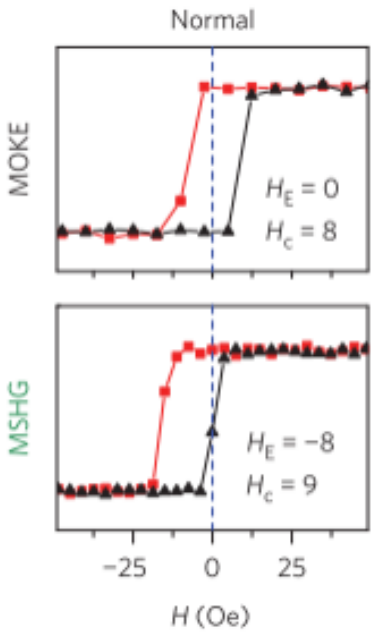

Figure 1.11: Magnetic hysteresis for magneto-optical Kerr effect (MOKE) measurements (Top) and MSHG (Bottom) for Fe/MgO interfaces. The central offset from the blue dashed line for the MSHG hysteresis loop is indicative of exchange bias at the Fe/MgO interface [28].

1.5 Progression of Dissertation

The proceeding dissertation is organized by individual projects each independent of one another. Aside from the experimental technique overview in Chapter 2, Chapters 3-5 can be read out of order without loss of generality. The experimental techniques in Chapter 2 were all designed from scratch, beginning with RASHG to identify concentration dependent electron symmetry of $(Bi_{1-x}Sb_x)_2Se_3$ in Chapter 5. That setup was upgraded to incorporate sample cooling for the temperature-dependent electronic phase transition for $IrTe_2$ in Chapter 3. Ultrafast pump-probe spectroscopy described in Section 2.4 originally started as a unrelated side project, but was adapted for the LSMO/STO study in Chapter 4 once those materials were discovered. Currently, efforts are being made to extend the pump-probe setup to incorporate an electromagnet for time-resolved magneto-optical studies. A lot of time and effort was devoted towards expansion of the optics lab capabilities primarily aimed at material surfaces at low temperatures with clean surface conditions. The

ultra-high vacuum chamber and corresponding optical design in Section 2.3 are nearing completion, serving as a new platform for future experiments.

Chapter 2
Experimental Techniques and Design

This chapter outlines the experimental setups used in this thesis. Each setup was specifically designed and built for a specific investigation. The light source was provided by two commercial Ti:Sapphire (Ti:Sapph) amplifiers: Coherent Libra He and Spectra-Physics (model: Solstice Ace). Both amplifiers output pulses are spectrally centered around 800 $\pm$8 nm with a temporal pulse width of <100 femtoseconds. The pulse train frequency is 1 kHz. Each pulse has a peak energy of <6.0 mJ, corresponding to an average power of 6 W integrated over 1 kHZ.

2.1 Rotational Anisotropy Second Harmonic Generation

As introduced in Sections 1.3 and 1.4, the anisotropic second harmonic response from a surface rotated about its surface normal is capable of determining the electronic symmetry. We will refer to this type of measurement as rotational anisotropic second harmonic generation, or RASHG.

Figure 2.1 schematically illustrates the RASHG design. Starting from the laser, the pulses polarization is rotated using a half-wave plate ($\frac{\lambda}{2}$) in order to match the field polarization to the pattern on the reflective diffraction grating, at the beginning of the pulse shaper. A half-wave plate is a birefringent crystal optimized to manipulate polarization without loss by shifting the phase between horizontal and linear polarization. By shaping a femtosecond pulse, the pulse is reduced in frequency space and broadened in the time domain[1]. For this optical setup, a variable split reduces the frequency bandwidth by attenuating higher and lower frequencies. After pulse shaping, the pulse has a temporal width of $\sim$ 2 ps on average. Following the pulse shaper, another half-wave plate is used for selecting the fundamental field polarization as either in-plane P or out-of-plane S. The laser is focused onto the sample at an angle of $\Theta = 45°$ using a convex lens. Reflected fundamental

[1]Gaussian pulses obey the time-energy uncertainty principle, $\Delta t \Delta\omega \geq \frac{1}{2}$. By increasing the spectral resolution, the pulse must become temporally broadened. If for instance, the pulse was spectrally narrowed to be monochromatic, the pulse would infinitely broaden such that it could no longer be Gaussian and you'd be left with a standard continuous wavelength laser.

and generated second harmonic are collimated using another convex lens. Polarization of the SHG is selected using a Glan-Taylor polarizer. A Glan-Taylor polarizer is a birefringent crystal capable of splitting electric fields into P and S polarized components, and can be rotated to choose either P or S transmission. Lowpass filter are used to attenuate (through absorption) the fundamental 800 nm light prior to a monochromator/spectrometer coupled to a high-sensitivity charge-coupled device (CCD). LabVIEW is used to automate and conduct the RASHG experiment. We use a piezo-motor controlled beam block to block the fundamental beam allowing differentiation between SHG and background. Sample azimuthal rotation, fundamental polarization, and SH polarization are augmented with computer controlled piezo-rotation stages.

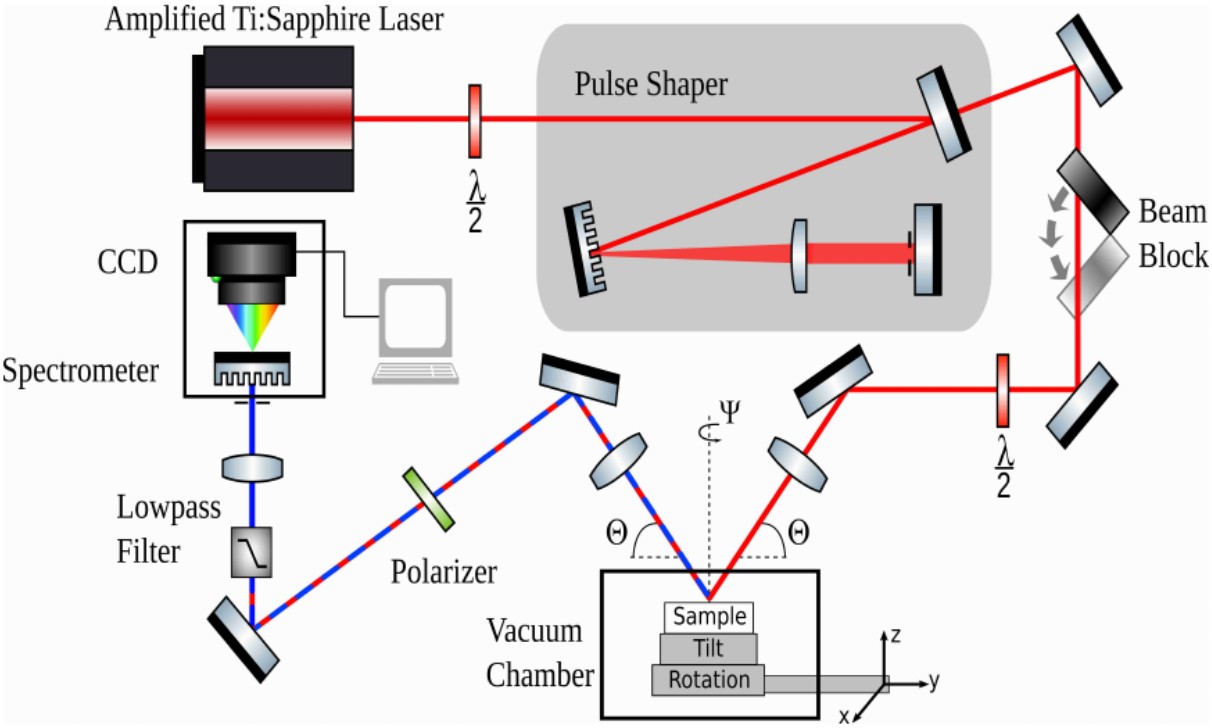

Figure 2.1: Rotational anisotropy second harmonic generation optical setup.

When sample movement is involved in optical setups great care needs to go into sample positioning to ensure alignment. A method for azimuthal rotation without loss of alignment was developed. First a helium-neon (HeNe) laser is used to define a beam path normal to the optical table. This axis serves as the rotation axis for the sample. Next, the sample

rotational axis must be a aligned so that it is identical and centered on the HeNe axis. To do this, the rotation stage must have tilt and translational capability. Once aligned, the sample is mounted on a tilt stage interfacing on top of the rotation stage such that the sample is centered on the rotation axis. The sample's tilt stage is necessary for compensating tilt differences naturally occurring from mounting or sample geometry for single crystals.

Analysis of raw RASHG data is done by a custom Python script. It begins by loading in all spectra and background, while removing any anomalous spikes possibly caused by high energy particle collisions with the CCD chip. The second harmonic peak and its background are integrated using a trapezoidal integration algorithm. All spectra and background at each rotation are averaged together and then subtracted out to generate polar plots.

2.2 Temperature-Dependent Second Harmonic Generation

Many materials undergo transitions in their order parameters (macroscopic number distinguishing two phases) through cooling and oftentimes it very important to track. For temperature-dependent measurements, the sample is placed in a vacuum chamber with a max base pressure of 10^{-3} Torr., limited by our vacuum chamber. This pressure is sufficient to prevent water condensation and ice formation on the sample surface during the cooling process. Optical access to and from the chamber is through a CaF_2 window. Inside the chamber, the sample is mounted on a stack, shown in Fig. 2.2, which includes a thermoelectric cooler[2], flow cell, tilt stage, and piezo-driven rotation stage, all on a three-axis manipulator. Thermally attached below the thermoelectric cooler is an aluminum flow cell, where a closed-loop water flow serves as a cold reservoir to dissipate heat from the hot side of the thermoelectric cooler. Using a chiller to maintain the cold reservoir at exactly 274 K, the minimum temperature obtainable by the thermoelectric cooler is $\Delta T = 70$ K relative to the cold reservoir, or 204 K. By changing the voltage across the thermoelectric cooler, the sample temperature can be precisely controlled. Thermocouples are attached to both the sample as well as the cold side of the thermoelectric cooler.

[2]A thermoelectric cooler a.k.a. a Peltier device creates a temperature difference between two ceramic plates through the Seebeck effect when a voltage is applied across the plates.

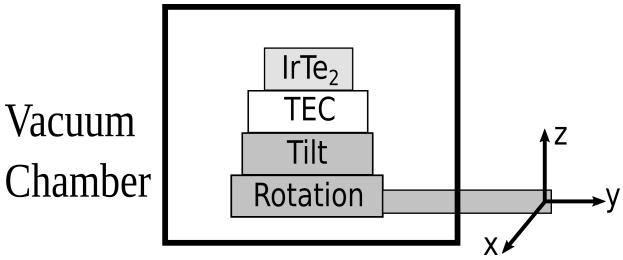

Figure 2.2: Cooling mechanism for the temperature-dependent-setup inside the vacuum chamber. The sample is placed on a thermoelectric cooler (TEC) on top of tilt, rotation, and three-axis translation.

Measurements can be done manually by adjusting the voltage of the thermoelectric cooler and taking spectra of the SHG signal and background, or semi-automated such that the SHG signal and background are continuously taken while the temperature is manually lowered. Before data is collected, the temperature must stabilize. For these experiments, the cooling and heating rate is dependent upon the stabilization time of the sample surface as measured by the thermocouple. Due to the coarse nature of the voltage knob adjustment and sensitivity of the thermoelectric cooler, the uncertainty for the temperature measurements is ± 0.2 K.

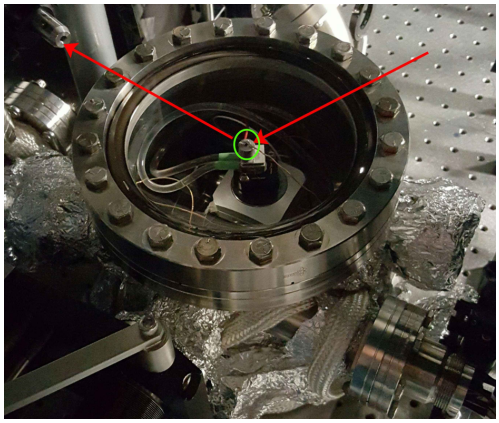

Figure 2.3: Temperature-dependent SHG setup fully assembled and prior to cooling. Red arrows are the laser path and the sample is inside the green circle.

To begin a temperature-dependent SHG run, first RASHG is conducted at room temperature to ensure correct electronic symmetry and alignment. The sample is rotated to the angle that maximizes the second harmonic intensity at that polarization geometry. Finally, the sample is enclosed in the chamber, and cooled once sufficient vacuum is achieved.

The final assembly prior to cooling is shown in Figure 2.3. Red lines demonstrate the laser paths and the green circle is the sample on top of the temperature stack.

2.3 Ultra-High Vacuum System

The future of surface studies coupled to nonlinear optics lies in the ability to conduct RASHG measurements where the surface can be characterized in-situ under low temperatures conditions. Basic ultra-high vacuum (UHV) optical access to chambers is a trivial matter, but conducting sample and laser movement while maintaining low temperates <20 K remains a difficult technological challenge. Special design considerations must be taken to always maintain optical alignment

Design for the UHV system uses of two chambers, a loadlock chamber and combined optical/low-energy electron diffraction (LEED) chamber mounted on a mobile frame in Figure 2.4(a). The loadlock chamber, Figure 2.4(b), is a 4" diameter cylindrical design with 6 ports. When mounted on the support frame, a 6" door is located at the top for sample access. A pump station is mounted on the side of the flange with a base vacuum pressure of $7.5 \cdot 10^{-8}$ Torr, monitored by a cold cathode gauge. The frame support structure for the loadlock is adjustable providing versatility for future development, add-ons, and upgrades. A gate valve separates the two chambers. Samples are moved between the chambers via a transfer rod directly onto the cryostat manipulator in the optical chamber pictured in Figure 2.4(c).

The optical chamber is a 10" diameter cylindrical chamber designed to conduct nonlinear optical measurements and LEED under low temperature conditions. 8" flanges located on opposite sides of the chamber provides optical access of the laser and retractable LEED. LEED measurements are an essential compliment to SHG to verify surface quality and structure. A closed-cycle helium cooled cryostat and 5-axis manipulator is on the top flange. Two angled 4.5" viewports are for additional visibility for all sides of the sample. To achieve UHV, the chamber is equipped with an ion pump and a turbo pump, where a

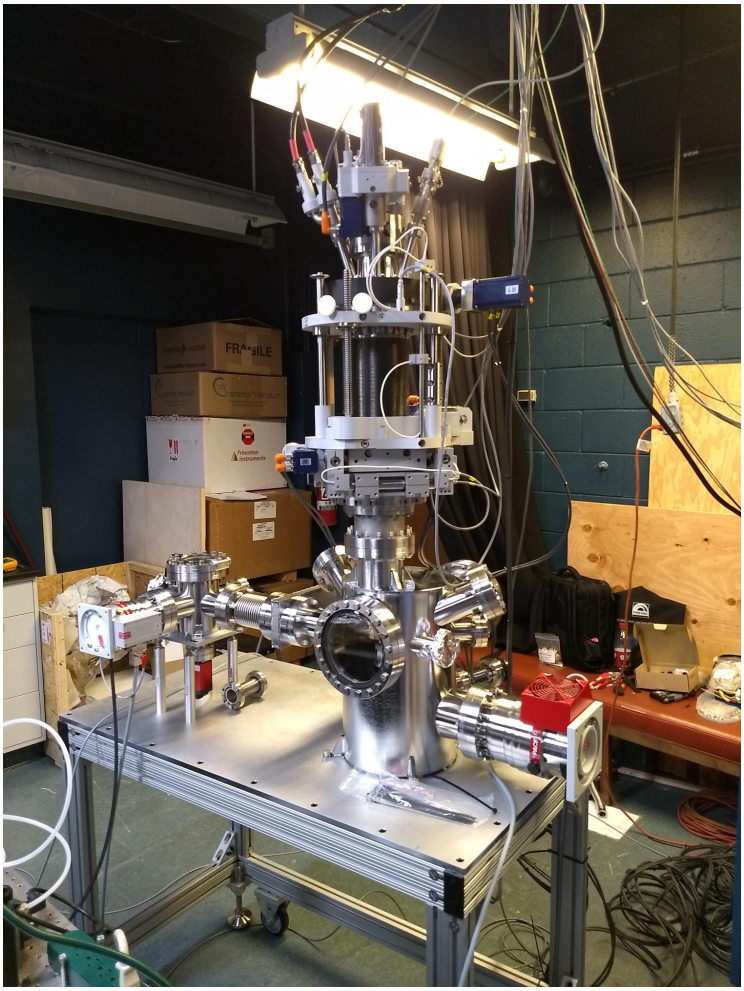

(a)

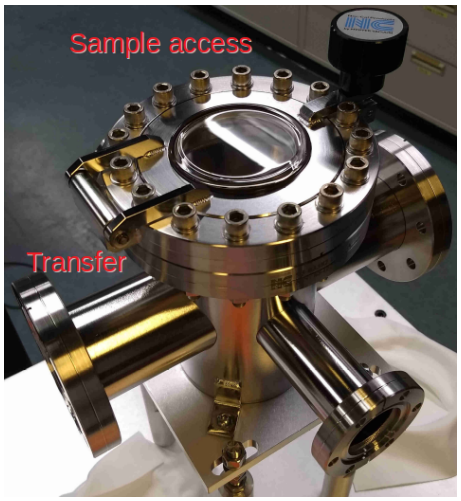

(b)

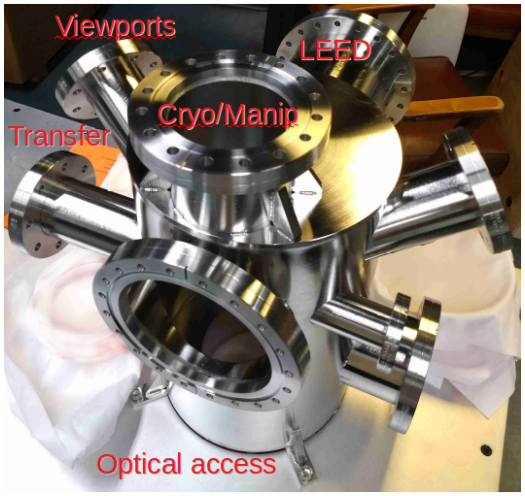

(c)

Figure 2.4: (a) Chamber assembly with the loadlock chamber on the left, optical/LEED chamber on the right, cryostat/manipulator, and mobile frame. (b) Loadlock chamber (c) Combined optical and low energy electron diffraction chamber. Important ports are emphasized.

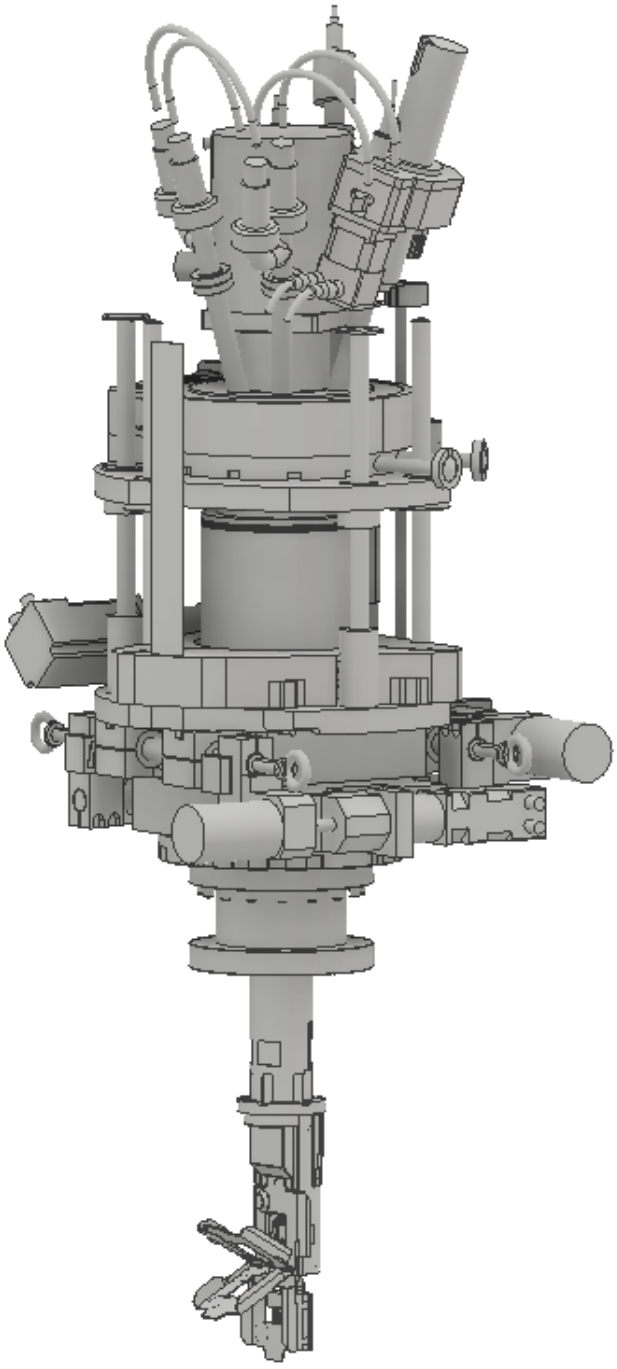

(a)

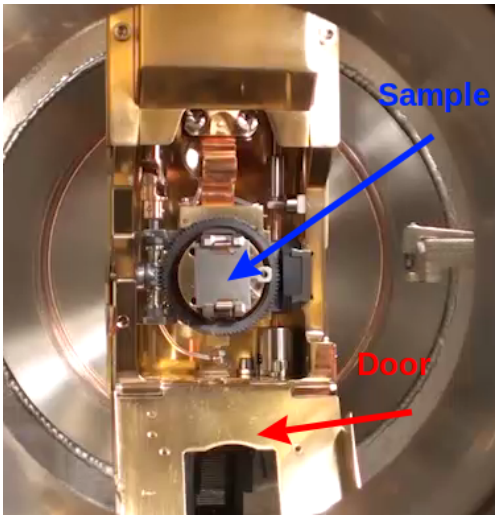

(b)

Figure 2.5: (a) Closed-cycle liquid helium cooled five-axis manipulator. (b) Close-up of the sample holder and shield/door.

base pressure of $\sim 10^{-11}$ Torr can be reached. A 1 - 100 amu residual gas analyzer monitors vacuum quality and detects trace impurities.

The 5-axis cryostat manipulator (Fig. 2.5) from Prevac will be used to cool the sample. Sample motion consists of $\pm$ 13 mm x and y translation and $\pm$ 100 mm of z translation as well as 360° polar rotation and 60° sample tilt. The UHV system will be housed in a building without helium recycling so the manipulator will cool via closed-cycle liquid helium. With this manipulator, sample temperatures as low as 10 K and heating up to 1200 K with electron bombardment can be achieved. A wobble stick can be used to remove a cooled sample for cleaving. Unique to this manipulator is the sample door shown in Figure 2.5(b). The door can be opened and closed with a special wobble stick for sample exchange and when closed provides thermal shielding.

Together the chamber assembly sits on a mobile frame designed to lock to the optical table during SHG measurements. Attached to the base frame is the manipulator's recirculating hose support structure shown in Fig. 2.6. The support was designed and constructed out of T-slotted aluminum framing. At the top of the structure is large 48" diameter wheel made out of water jet cut PVC. A rod and bearing attach the wheel to the top of the

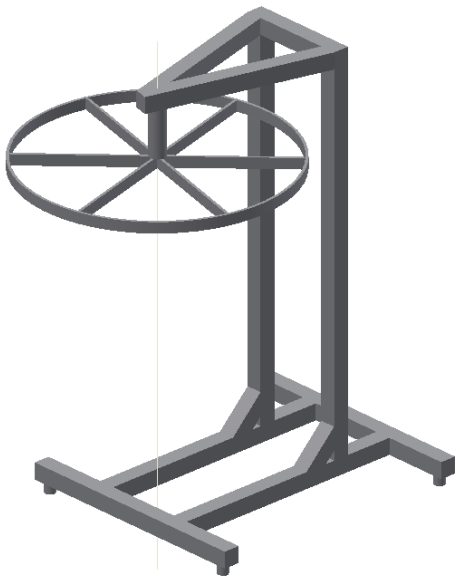

Figure 2.6: Hose support design structure with a rotating PVC wheel.

frame as to bare the weight of the hoses and provide polar rotation of the hoses with the manipulator.

2.3.1 Rotational Anisotropy Second Harmonic Generation With a Rotating Scattering Plane

Single crystal growth methods like the flux method and floating zone, consistently produce high-quality single crystals, yet often times achieving large optically preferred flat/reflective surfaces is not consistent. More often than not, the surface size is on par with the focal size of the laser greatly increasing the difficulty of alignment. Conventional methods for RASHG describe in the preceding sections are no longer viable. In 2014, Hsieh et al. created a new method for SHG measurements by rotating the scattering plane for fundamental and second harmonic fields relative to a stationary sample [29]. By removing movement of the sample, this new approach removes the aforementioned limitations allowing any sample to be studied. Inspired by their breakthrough, we designed a similar system which we will couple to our chambers.

Figure 2.7 showcases the optical setup. The initial laser polarization is selected and sent through a phase mask. A phase mask is a specialized optical element that diffracts a pulse by the +1 order. Following the diffracted beam, a collimating lens placed at the

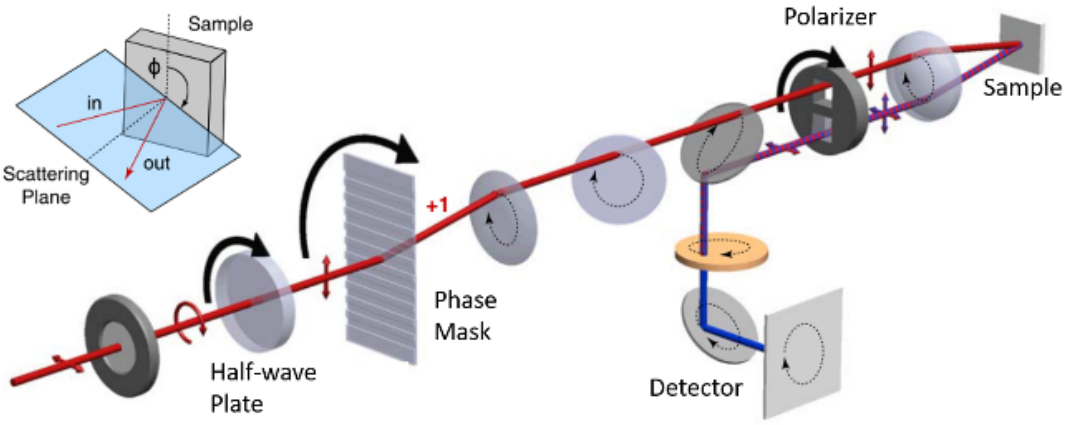

Figure 2.7: RASHG with a rotating scattering plane. The half-wave plate, phase mask, and polarizer rotate simultaneously, rotating the scattering plane around the sample normal. Figure adapted from [30].

focal distance from the phase mask to collimate the laser parallel to the original beam path. The laser is then focused onto the sample and the reflected beam is collimated using the same focusing lens. A dichroic beamsplitter splits the 800 nm and SHG light and redirects the second harmonic to a detector. The logic behind the setup is that the phase mask produces a separation of the laser relative to the initial beam path that is rotated about the beam path. By rotating the half-wave plate, the phase mask, and the polarizer simultaneously the scattering plane can be rotated about a stationary sample while preserving the polarizations of the beams. To integrate this setup. It is built on top of a three-axis translational breadboard so that the focal point of the setup can be placed directly on the sample inside the chamber.

2.4 Ultrafast Pump-Probe Spectroscopy

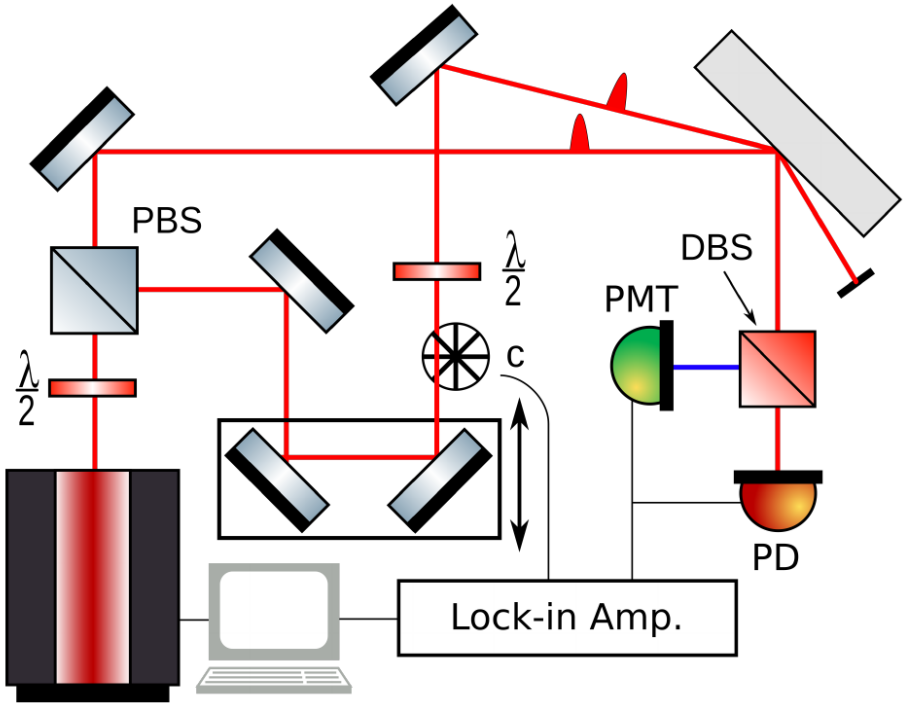

Figure 2.8: Time-resolved pump-probe reflectivity optical setup. PBS - polarized beam splitter, c - chopper, PMT - photomultiplier tube, DBS - dichroic beam splitter, PD - photodiode.

Pump-probe spectroscopy measurements including reflectivity and pump-probe SHG are valuable experiments to capture atomic and molecular dynamics at the timescales of atomic motion. The ultrafast designed reflectivity setup is shown in Fig. 2.8.

Pump and probe beams are separated using a polarizing beam splitter (PBS), and a half-wave plate can control the ratio of pump and probe splitting. The pump line is sent through a computer-controlled delay stage mounted retroreflector, which is a set of mirrors aligned so that the outgoing path is parallel to the incoming path. Moving the delay stage changes the pump pulse timing relative to the probe pulse. A half-wave plate is used to allow preferential pumping of in-plane versus out-of-plane. The probe beam is directed at a 45° angle to the sample surface. For power dependent studies, a neutral density filter in combination with the PBS control the pump and probe pulse energy.

To ensure the probe pulse is measuring a homogeneously pumped excited region, it is important that the beam waist of the probe is much smaller than the pump. The beam waist is the focal spot size of the beam at maximum focus. For a collimated Gaussian beam of initial radius ω_0 normally incident to a focusing lens of focal length f, the focused beam waist ω_f is given by the relation

$$\omega_f = \frac{\lambda f}{\pi \omega_0} \quad \rightarrow \quad \frac{\omega_{f,pump}}{\omega_{f,probe}} = \frac{f_{pump}}{f_{probe}}. \tag{2.1}$$

Conventionally, greater than 4:1 pump:probe beam waist ratios are safe to ensure the probe is within a homogeneous pump region. Therefore, based off Eq. 2.1, focal lengths of 500 mm for the pump and 100 mm for the probe were selected to give a 5:1 ratio of the beam waists.

Using a barium borate crystal as a high-conversion medium, the pump and probe pulse are both spatially and temporally overlapped generating SFG. This condition, commonly named 'time-zero', serves as the zero point in time that the pump pulse timing is varied relative to a stationary probe. Step sizes for the delay stage vary depending on the timescale

of the dynamics under investigation. As a general rule of thumb, a spatial step of 1 mm corresponds to a temporal step of 3.33 ps. The temporal resolution is limited by the probe pulse width of <100 fs.

For detection, a fast photodiode is used for pump-probe reflectivity to collect 800 nm photons. A photomultiplier tube with appropriate 800 nm filtering is used for pump-probe SHG studies to collect 400 nm photons. The pump pulse repetition rate is modulated to a frequency of 500 Hz using an optical chopper wheel coupled to lock-in amplification detection. By altering the sample averaging, the signal-to-noise is greatly increased. When the pump is chopped, the change in the probe with regards to the pump on and off is known as the change in reflectivity (Eq. 2.2).

$$\frac{\Delta R}{R}(t) = \frac{R_{pump,on}(t) - R_{pump,off}}{R_{pump,off}} \tag{2.2}$$

Chapter 3
Electronic Phase Transition in $IrTe_2$ Probed by Rotational Anisotropy Second Harmonic Generation

3.1 Introduction to Transition Metal Dichalcogenides

Transition-metal dichalocogenides (TMDs) rose to popularity in the 1970s, primarily at the time as a candidate for charge density waves (CDWs) [32, 33]. TMDs are a class of materials in which a metallic transition metal sheet (T) is sandwiched between two chalcogen (X) sheets. The sheets can stack according to three configurations, illustrated in Figure 3.1: trigonal (H), octahedral (T), or distorted (T'). The TX_2 sandwiches are bonded together typically through weak van der Waals bonding creating the bulk compound [35]. Furthermore, significantly weaker out-of-plane bonding compared to in-plane makes TMDs easily exfoliated down (by mechanical and liquid means) to the monoatomic limit [31]. Depending on the transition metal ion group (IV to X) or chalcogen (Te, Se, or S), versatile structures and electronic phases from insulators (HfS_2) to semiconductors (MoS_2) and metals ($IrTe_2$) are possible. As an example, Fig. 3.2 showcases the known electronic and structural phases for TMD compositions grouped by transition metal elements [31]. Coupled to the rich elec-

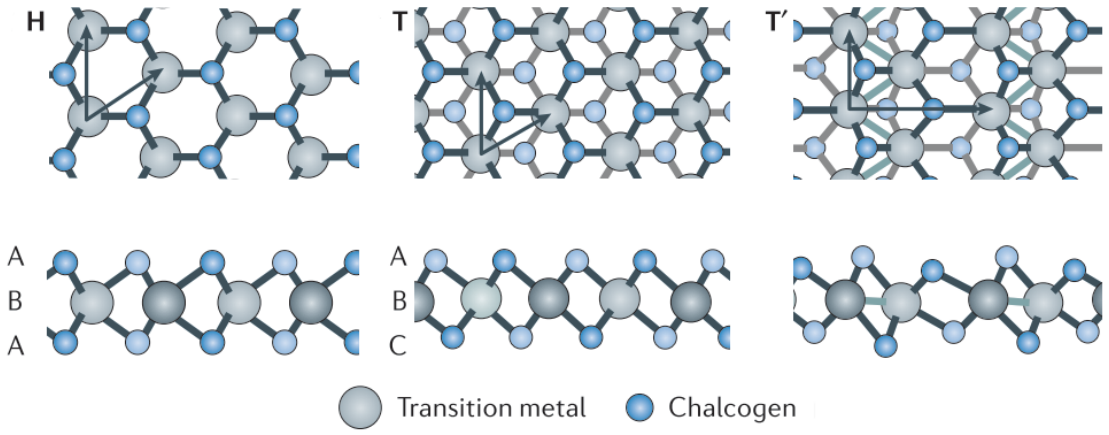

Figure 3.1: Three transition metal dichaolcogenide stacking configurations: trigonal (H), octahedral (T), or distorted (T'). Figure adapted from [31]

The work in this chapter is published as: J. E. Taylor, Z. Zhang, G. Cao, L. H. Haber, R. Jin, and E. W. Plummer, "Electronic Phase Transition of $IrTe_2$ Probed by Second Harmonic Generation," Chinese Physics Letters, Vol. 35, No. 9, 097102 (2018) [34].

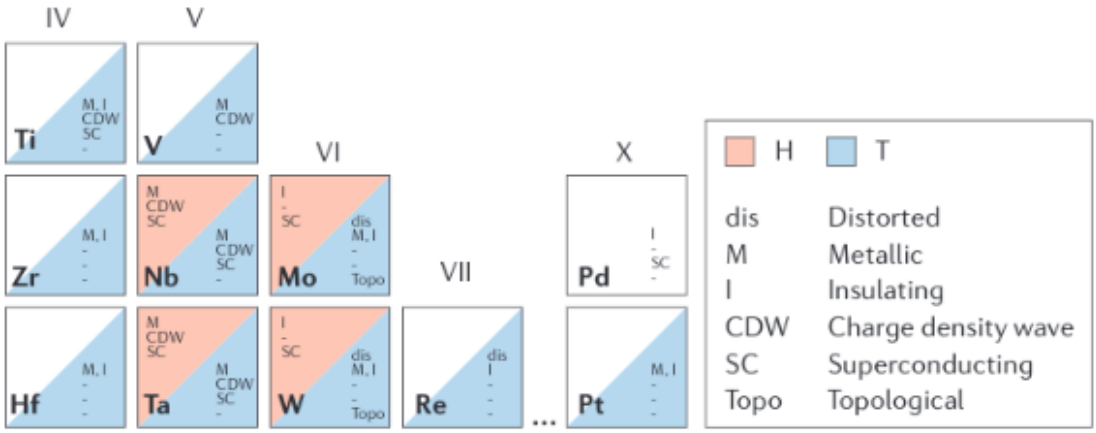

Figure 3.2: Periodic table for structure and electronic phases of transition metal dichalcogenides organized by transition metal groups. Stacking configurations H and T are highlighted in red and blue respectively. Figure adapted from [31]

tronic properties are exotic interesting physical behaviors, notably superconductivity [36], topological behavior [37], charge density waves [38], and large magnetoresistance in WTe_2 [39]. Heavy d orbitals from the transition metal ions with inversion symmetry in spin-split conduction and valence band due to strong spin-orbit (SO) coupling. In two-dimensional TMDs spin-split bands occur at opposite high symmetry points across the Brillouin zone generating a plethora of excitons, valley physics, and topological phases [40].

Since the creation of graphene was first reported in 2004 (the first free standing 2D atomic crystal) by Geim and Novoselev [41][1], the field of two dimensional materials has expanded rapidly towards device development. Graphene while promising due to its strength, flexibility, and electron mobility, lacks the bandgap necessary for optical applications. TMDs, however, have a tunable band structure with layer thickness. At the monoatomic limit for many semiconductor TMDs, such as MoS_2, the indirect bandgap can become direct and located at high symmetry points in k-space, making them an important alternative as low-dimensional materials [42]. Consequently, W. Choi and collaborators report that the citation rate for two-dimensional TMDs has increased accordingly, from less than 1000 citations per year in 2004 to greater than 5000 per year in 2015 [43]. TMDs offer an un-

[1] Andre Geim and Konstantin Novoselov were jointly awarded the Nobel Prize in Physics in 2010 "for groundbreaking experiments regarding the two-dimensional material graphene."

paralleled playground for device creation, with a wide range of applications from catalytic sensors [44] to optoelectronics [45]. Therefore, it is of great importance to understand the complex electronic interacts in TMDs.

3.2 Introduction to $IrTe_2$

$IrTe_2$ is a very interesting TMD due to it's unusual structural phase transition and doping induced superconductivity [46, 47]. Originally, researchers believed that the structural transition had the fingerprint of a charge density wave (CDW), due to the periodic lattice reconstruction and charge ordering in the low temperature phase. However, angle-resolved photoemission spectroscopy has yet to see the signature gap in the Fermi surface or Fermi surface nesting. Current research has continued to provide evidence against CDWs in $IrTe_2$. However, understanding the mechanism for generating a periodic charge and lattice distortion in this system has remained elusive.

At room temperature, $IrTe_2$'s unit cell consists of eight edge-shared $IrTe_6$ octahedras. Each octahedra lie on the vertices of a rhombohedron forming a trigonal unit cell with $P\bar{3}m1$ space group symmetry (see Fig. 3.3(a)). Layers are stacked along the c axis in a H sequence. We define this unit cell as [1×1×1] with the first two indices in-plane. Most important about $P\bar{3}m1$ is a that it is centrosymmetric space group. $IrTe_2$ easily cleaves

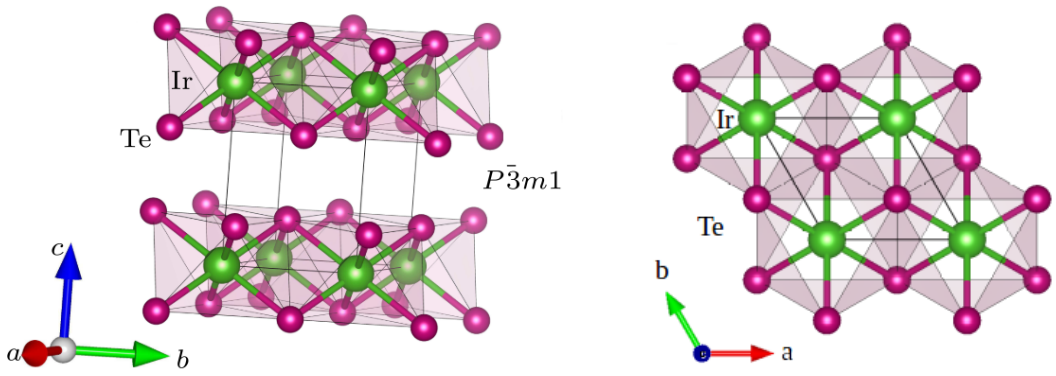

Figure 3.3: $IrTe_2$'s [1×1×1] unit cell in the high temperature phase. Pink and green balls represent Te and Ir atoms respectively. (a) $IrTe_2$ hexagonal unit cell with $P\bar{3}m1$ symmetry. (b) $IrTe_2$'s surface with C_{3v} point group symmetry.

along the $a-b$ plane and the surface has a C_{3v} point group symmetry[2] [16]. The schematic in Figure 3.3(b) illustrates the $IrTe_2$ surface projection in the a-b plane where each Ir atom is surrounded by six Te atoms. A C_{3v} surface symmetry produces a three-fold out-of-plane and a six-fold in-plane rotational anisotropic second harmonic signal.

Our colleagues have performed atomic scale measurements of $IrTe_2$'s microscopic structure using scanning transmission electron microscopy (STEM) and electron diffraction [48]. Figure 3.4(a) is the electron diffraction for the (100) surface. The diffraction spots have a [1×1] pattern in agreement with a trigonal unit cell. High-angle annular dark field STEM (HAADF-STEM) images of $IrTe_2$ (Figure 3.4 (b)) shows vertical columns (along the $c-a$ plane) of stripe-like bright spots with each spot consisting of three points. These points correspond to the Te-Ir-Te layers in the unit cell. The yellow dashed line marks a nearly aligned grain boundary of two different domain regions. Each domain region has a distinct difference in contrast between background and Ir/Te columns.

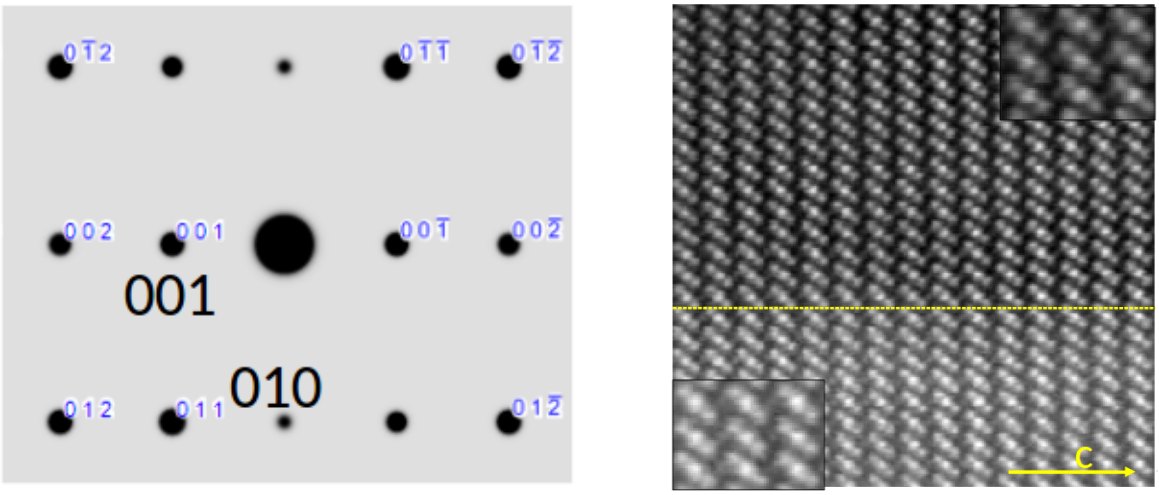

(a) (b)

Figure 3.4: Microscopic structural characterization of $IrTe_2$. (a) Room temperature [1x1] structure measured by electron diffraction for the (100) plane. (b) Room temperature High-angle annular dark field STEM (HAADF-STEM) image where columns of three bright spots are the Te-Ir-Te layers. Yellow dotted line is a grain boundary. Figures from Ref. [48]

[2]Schoenflies notation is a popular spectroscopic notation for expressing point group symmetries. C denotes a cyclic rotational axis. n is the number of mirror planes perpendicular to the axis of rotation. v indicates vertical mirror planes.

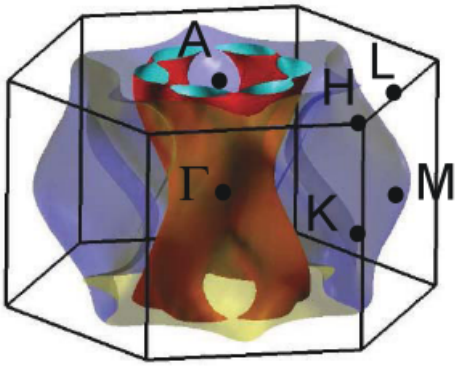

Figure 3.5: $IrTe_2$ high temperature phase Fermi surface. Γ, A, K, H, L, and M are high symmetry points in the Brillouin zone. Large dispersion along the Γ-A direction reveals three-dimensional behavior. Figure adapted from [49].

$IrTe_2$ has a peculiar Fermi surface signifying that $IrTe_2$ is not a traditional layered TMD like its two-dimensional van der Waals counterparts. The Fermi surface depicted in Figure 3.5 was calculated first by Yang et al and then confirmed by Pascut et al. [47, 50]. At room temperature large dispersion can be seen along the c-direction (Γ-A) suggesting electronically $IrTe_2$ is not layered. This calculation is consistent with the interlayer bond spacing being much shorter than in-plane bond distances (3.5016 Å verses 3.5532 Å and 3.9319 Å) indicating $IrTe_2$'s layers are weakly covalent bonded [51].

3.3 $IrTe_2$ Phase Transition

Crystalline structural phase transitions are generally classified by either first-order or second-order based on the continuity of the order parameter[3] [53, 54]. The behavior associated with a first-order phase transition (PT) can be described by the Landau model. At the critical temperature, the system undergoes a symmetry breaking change to reduce the free energy represented by a discontinuity in the order parameter. Associated with first-order transitions is a hysteresis, resulting from the energy needed to overcome a metastable state and induce the transition.

Most interesting about $IrTe_2$ is the complexity, surrounding its T_c ∼280 K charge order/structural phase transition. While no current model can definitely identify the origin of

[3]This classification is known as the "Ehrenfest condition", first introduced by Paul Ehrenfest in 1933 [53].

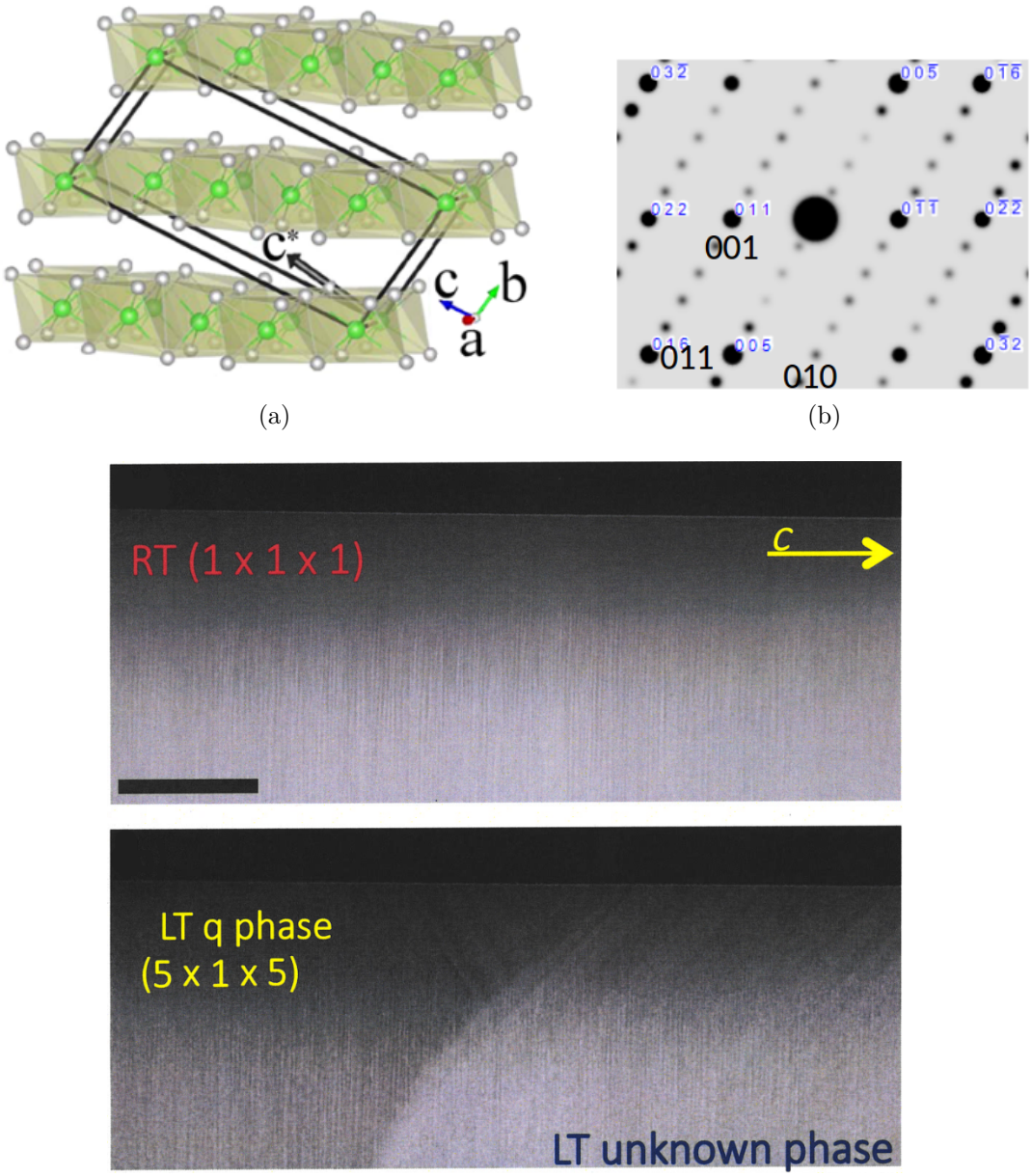

(a) (b)

(c)

Figure 3.6: (a)$IrTe_2$ [5 × 1 × 5] bulk unit cell ($P\bar{1}$ space group). The new c-axis, c*, is not parallel with c in the high temperature phase [50]. (b) $IrTe_2$ [5 × 1 × 5] bulk phase measured with TEM in the low temperature phase characterized by the emergence of three fractional spots between integer spots [52]. (c) Low magnification HAADF-STEM. Top: [1x1x1] room temperature phase shows homogeneous morphology. Bottom: Low temperature phase shows mixed morphology containing the [5x1x5] phase and an unknown phase [48].

the transition, many theories and experimental explanations point towards many physical causes. The high temperature structural phase transition has been shown to suppress and disappear altogether under Pt and Pd substitution on the Ir site [47], coinciding with the emergence of the superconducting transition and possibly identifying the interplay between charge-orbital ordering and superconductivity. Unraveling these mysteries is greatly important the fundamental physics of transitions of materials with periodic charge and lattice ordering.

Below T_c, $IrTe_2$'s undergoes a structural long-range three-dimensional reorganization from a [1×1×1] to [5×1×5] shown in Fig. 3.6(a& b). The unit cell now has triclinic symmetry with the $P\bar{1}$ space group where the c-axis stacking is no longer parallel to the high temperature phase [51]. Both phases have been confirmed with STEM measurements; however, the [5×1×5] phase show a mixed morphology meaning the transition may not be homogeneous throughout the sample as shown in Figure 3.6(c). The most striking feature of the phase transition is a structural modulation of the Ir-Ir bonding, where bonds dimerize with a bulk vector $\mathbf{q} = (\frac{1}{5} \times 0 \times \frac{1}{5})$. Neutron diffraction measurements of the (-2 1 0) subcell peak as a function of temperature (Figure 3.7) reveal the transition is first-order phase transition in the bulk where $IrTe_2$ exhibits a discontinuity and thermal hysteresis of the integer diffraction peak across T_c [55].

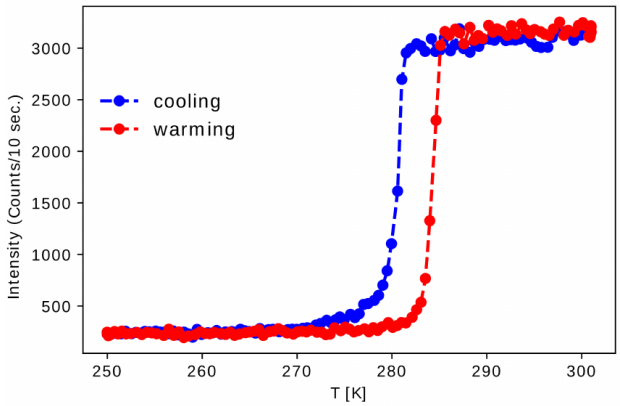

Figure 3.7: $IrTe_2$ low temperature phase structural bulk transition. Temperature dependence of the (-2 1 0) subcell peak measured by neutron diffraction [55]. Blue and red circles represent the cooling and warming processes respectively.

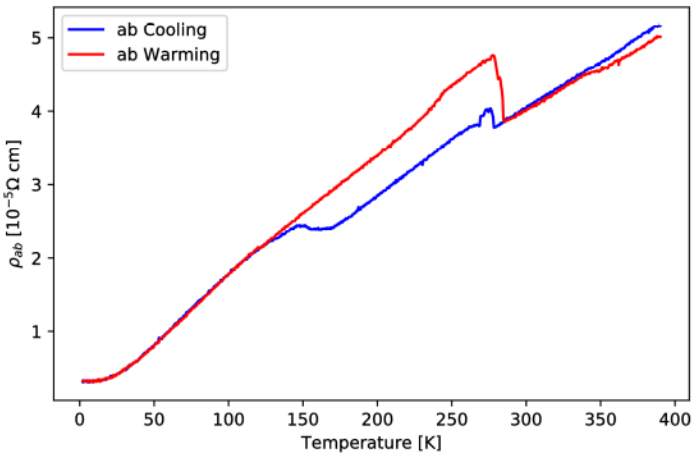

Figure 3.8: Transport measurements for the in-plane resistivity of $IrTe_2$ as a function of temperature. Two transitions are seen in the cooling and one in warming with a very large thermal hysteresis. Figure adapted from [51]

Transport measurements conducted by our research group on $IrTe_2$ single crystals are reported in Figure 3.8 [51]. Throughout the thermal cycle, $IrTe_2$ demonstrates metallic behavior indicated by the constant negative slope in the resistivity. If a Peierls-like CDW transition were present, the resistivity should become insulating. Upon cooling there are two phase transitions, one around $T_c \sim 280$ K and the other around $T_{c2} \sim 170$ K, indicated by the sharp step-like behavior in the resistivity. When warming a large thermal hysteresis is observed and only one phase transition is present around 290 K.

Accompanying the bulk structural transition, photoemission spectroscopy has measured the formation of a charge stripe modulation in the Ir *d* orbitals (Ir 5 d^{3+} - Ir 5 d^{4+}) [56]. Density functional theory calculations in Figure 3.9(a) show a corresponding Fermi surface reorganization, especially along the a-b direction. As $IrTe_2$ undergoes its phase transition it becomes two-dimensional, a stark contrast to the three-dimensional high temperature Fermi surface. Furthermore, no gap opening and no Fermi surface nesting is present in these calculations confirming this is not a charge density wave. First principle calculations for the total density of states and Ir density of states above and below the transition near the Fermi energy were performed by Pascut et al shown in Figure. 3.9(b)

[50]. For both the high and low temperature phase no change in the density of states would indicate an instability driving the transition.

There are many competing models surrounding the origin of the phase transition. Originally, CDW driven by a Peierl's instability was proposed by Yang et al in 2012 [47, 57]. However, previously discussed density functional theory has shown no evidence of gap openings or Fermi surface nesting. Many other models have been proposed, mainly disagreeing over the responsibility of the Ir 5d and Te 5p orbitals. Models range from anionic depolymerization of Te bonds [58], instability in the Te 5p states at the Fermi energy [55], Te 5p and Ir 5d orbital interaction [59], orbital splitting of the Te 5p states [49], and Ir-Ir dimerization [50, 60, 61]. The culmination of all these studies proves there is still much more to discover regarding the mechanism(s) driving the transition.

Of all the theories, two first principle calculations by Cao and Pascut propose conflicting explanations while simultaneously producing similar results near the Fermi surface [50, 55]. Cao et al. calculations demonstrate that the Ir 5d - Te 5p bands are strongly hybridized. As a result, nominal iconic models ($Ir^{4+}Te_2^{2-}$) can not be used. Large reductions in the Ir DOS around the Fermi energy while retaining Ir-Te hybridization indicates the Te 5p states as cause of the distortion [55]. Pascut et al. were able to eliminate electron correlations as

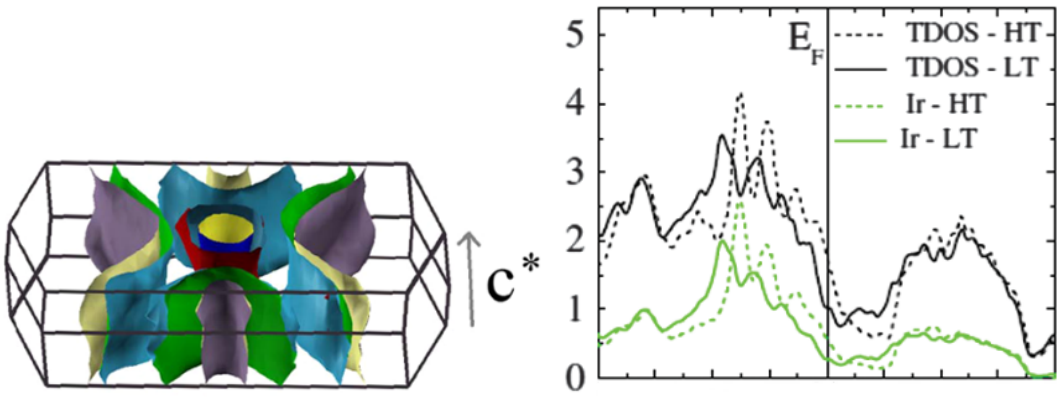

(a) (b)

Figure 3.9: (a) $IrTe_2$ low temperature phase Fermi surface. (b) Total and Iridium density of states near the Fermi energy for the high and low temperature phases. Figure adapted from [50]

primary contributors to the transition, and increased density of states from Ir-Ir bonding conclude that the origin is Ir-Ir dimerization [50].

3.4 Second Harmonic Generation Experimental Results

To try and understand the origin of the phase transition, it is important to isolate the surface electronic response, motivating SHG studies. $IrTe_2$ single crystals were provided by our research group at Louisiana State University. Single crystals were grown using the self-flux method described by Cao et al [51]. Powder x-ray diffraction measurements are shown in Fig. 3.10. Peaks correspond to constructive interference of diffracted x-rays when the Bragg condition is satisfied. Sharp Bragg peaks prove the sample is high-quality and stoichiometric while being single phase.

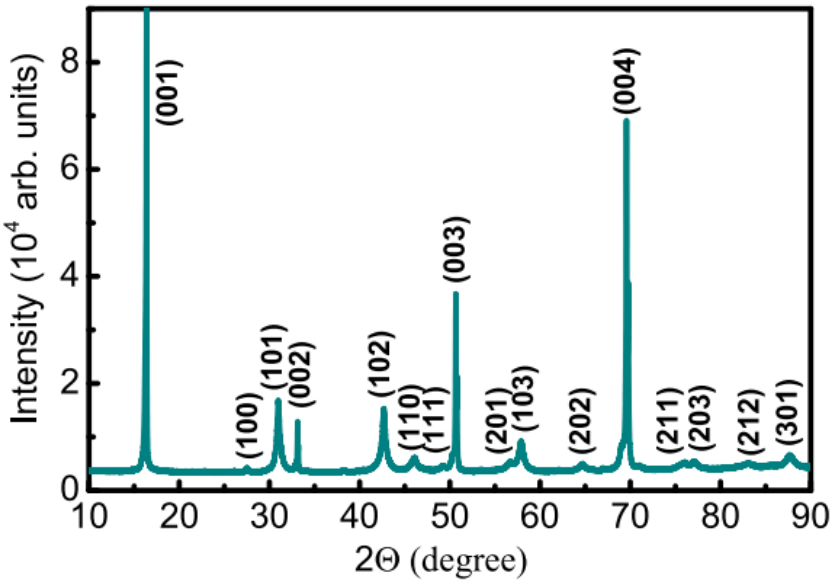

Figure 3.10: $IrTe_2$ powder x-ray diffraction for the high temperature phase [51].

The optical setup used to collect the rotational second harmonic generation is previously discussed in Section 2.1. A 120 micrometer spot size and a fluence of ~5 mJ/cm^2 was sufficient for good signal to noise without damaging the $IrTe_2$ surface. The laser was focused at an incident angle of 55° relative to the surface normal. For RASHG studies $IrTe_2$ was azimuthally rotated about the surface normal (001), which is perpendicular to

the (110) cleaving plane. Samples were cleaved in air using the scotch tape method one to two hours before measurements.

Figure 3.11(a & b) are the rotational-SHG of $IrTe_2$ as a function of azimuthal rotation angle at room temperature. The green dots are the raw second harmonic counts and purple lines are the theoretical fits. From Fig. 3.11(a) the polar plot for P-input P-output (PP) polarized radiation exhibits a three-fold symmetry characterized by three intense lobes spaced at 120° intervals. Between each intense lobe is a small intensity lobe. All the large intensity lobes are of equal value, and the same for the small intensity lobes. S-input S-output (SS) polarized light has a six-fold symmetry with 6 equal intensity lobes spaced 60 degrees apart. Any deviations in peak intensity from the SS lobes can be explained through alignment and optical artifacts. The PP signal has the highest intensity, so both plots are normalized to maximum PP signal. As a result, the intensity scale for SS is roughly one half of the intensity of PP.

Using symmetry tensor analysis for a reduced C_{3v} point group, the theoretical fits for the rotational SHG in Equations 3.1 and 3.2 were derived. Derivations of these equations

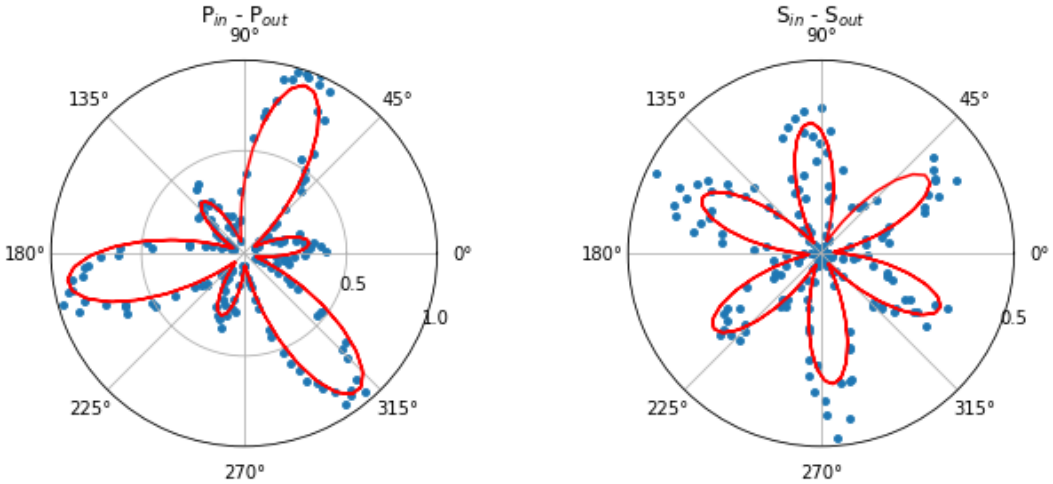

(a) (b)

Figure 3.11: $IrTe_2$ rotational second harmonic generation polar plots taken at room temperature. Blue dots are the intensity normalized to maximum PP. The red lines are the theoretical fits. (a) & (b) are the P_{input}-P_{output} and S_{input}-S_{output} polarization geometries respectively.

can be found in Appendix A,

$$I_{PP}(2\omega) = B|c_1 - c_3\cos(3\phi)|^2 \tag{3.1}$$

$$I_{SS}(2\omega) = B|c_3\sin^2(3\phi)| \tag{3.2}$$

where $B = AI^2(\omega)$ is a scalar amplitude, $c_1 \propto \chi_{zzz} + \chi_{zxx} + \chi_{xxz}$, and $c_3 \propto \chi_{xxx}$. From the fit equations, both PP and SS fit well with a R^2 value of 0.91 and 0.94 respectively. The nonlinear susceptibility values of $c_1 = 0.33$ and $c_3 = -1.06$ are extracted from the fits.

Based on the fit equations 3.1 and 3.2, the following conclusions can be made: (1) P polarized fundamental light can excite both in and out-of-plane (Ir-Te) electronic responses c_1 and c_3, but out-of-plane responses dominate the signal as evident by the three-fold instead of a six-fold generated by $\sin^2(3\phi)$ (2) S-polarized electric fields can only excite in-plane (Te-Te) electronic states making c_3 sensitive only to the in-plane electronic response. By comparing the fits to the C_{3v} crystal surface in Fig. 3.3 (b), it is evident that the in-plane and out- of-plane responses originate from electrons with the symmetry of the high temperature phase and are in agreement with the expected C_{3v} point group. This is confirmed with low energy electron diffraction measurements from the same batch of samples (see Fig. 3.12) showing a [5 × 1] surface symmetry [52].

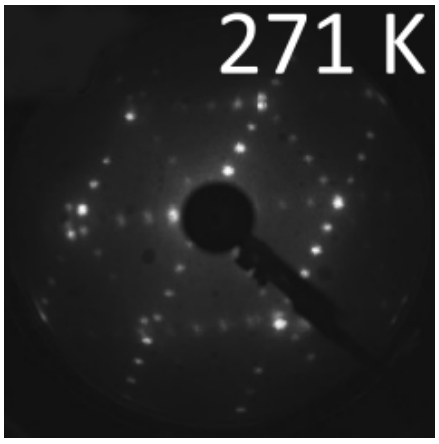

Figure 3.12: $IrTe_2$ low energy electron diffraction taken at 271 K. A [5 × 1] surface symmetry is seen by 3 fractional spots in between the [1 × 1] high temperature spots. Figure adapted from Ref. [52].

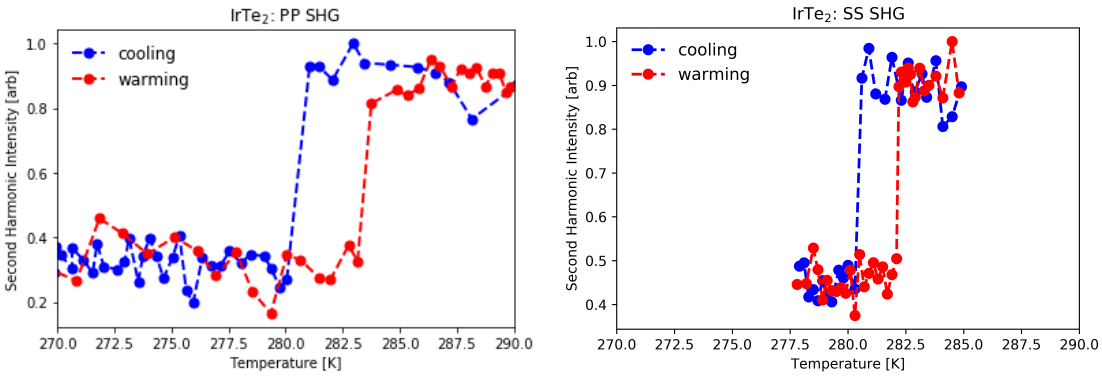

(a) (b)

Figure 3.13: $IrTe_2$ SHG temperature sweeps near T_c at two different polarization geometries: (a) P_{input}-P_{output} (b) S_{input}-S_{output}. Blue curves represent the cooling processes and red represent the warming process.

To study the surface electronic phase transition, $IrTe_2$ was cooled under vacuum described by the experimental setup in Sec. 2.2. The second harmonic was continuously measured while cooling across T_c and warming above T_c. Both the PP and SS polarization geometries were measured. At $T_{c,cooling}$ ~280 K there is a sharp decrease in the second harmonic due to an electronic symmetry phase change (Fig. 3.13(a)). The SHG remains constant throughout further cooling after the transition. When the process is reversed and the sample is heated, a first-order behavior is observed in the intensity at $T_{c,heating}$ ~282 K. After the phase transition back to the high temperature phase, the SHG intensity returns to its initial value. The resulting background seen after the transition is likely caused by surface imperfections and disorder resulting from the phase transition [62]. The transition temperature hysteresis between the heating and cooling is ΔT ~2 K. For the heating and cooling processes, the transition occurs within <0.2 K, which is an experimental limit by the temperature step process discussed in Sec.2.2. Fig. 3.13(b) shows the SS temperature evolution. Identical behavior in both the ΔT and temperature sharpness (within the experimental uncertainty) imply in and out-of-plane respond the same. Both transitions are repeatable throughout many cooling and warming cycles. After a complete thermal cycle, the high temperature C_{3v} surface symmetry is recoverable at room temperature.

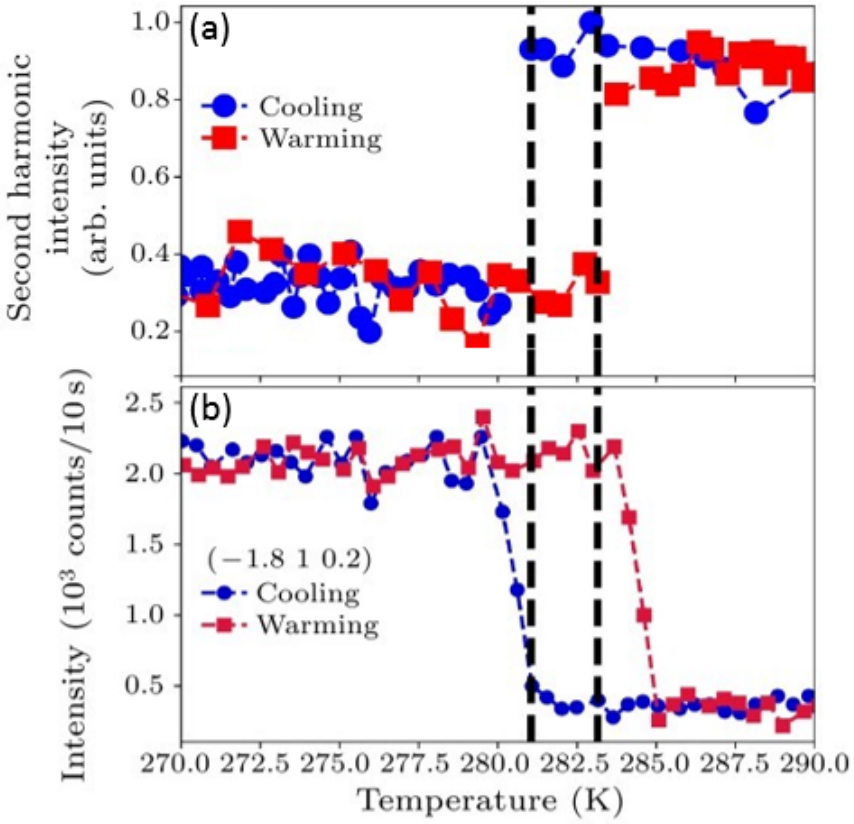

Figure 3.14: Temperature dependent phase transition of $IrTe_2$ near T_c as observed by (a) P_{input}-P_{output} polarized SHG. (b) Structural modulation of the (-1.8 1 0.2) peak measured by neutron diffraction. Data used from Ref. [55]. Vertical lines mark the onset of the transition as seen by SHG.

The triclinic crystal class has two space groups (P1 and P$\bar{1}$) and each space group has been reported for $IrTe_2$ [51, 63]. The P1 space group has C_1 point group symmetry and is noncentrosymmetric. However for P$\bar{1}$, the point group is S_2 which is centrosymmetric. For C_1, every element of the second order susceptibility is independent and nonzero. Furthermore, for application S_2 point group symmetry, tensor theory indicates that all second order susceptibility elements should go to zero, i.e. a significant reduction in the second harmonic intensity [16]. Typically for SHG, noncentrosymmetric structures produce much larger second harmonic intensities than centrosymmetric, contrary to the intensity decrease in Fig. 3.13. Therefore, the resulting intensity decrease of the second harmonic most likely corresponds to the transition into the centrosymmetric space group, P$\bar{1}$ with a surface symmetry of S_2. Elimination of all tensor elements contributions to SHG support the identical behavior of PP and SS. Although all tensor elements should go to zero for a homogeneous sample at low temperature, the nonzero intensity seen in SHG can be explained by the mixed [5 $\times$ 1 $\times$ 5] phase from Figure 3.6(c). The conclusion of SHG agrees with x-ray diffraction measurements take from the same batch of single crystals at low temperatures of a bulk P$\bar{1}$ space group [51].

To gain insight into the nature of the charge ordered/structural transition, we need to compare the SHG (Fig. 3.14(a)) with bulk structural measurements. The three-dimensional structural transition (Fig. 3.14(b)) probed via neutron scattering also shows a first-order transition in the fractional order diffraction spot (1.8 1 0.2). From the bulk structural transition, the ΔT is $\sim$2 K and while it takes 1 - 2 K for the transition to complete. A crucial point is that in all three measurements the ΔT $\sim$2 K hysteresis is roughly identical, meaning subtle structural differences between surface and bulk are not critical to the electronic surface properties and the transitions occur simultaneously. However, the thermal change of the second harmonic response ($<$0.2 K) is significantly shorter compared to the structural transition ($\sim$0.8 K). The sharpness of the surface electronic transition

relative to the bulk transition for both heating and cooling signifies the electronic transition seems to precedes the structural transition.

3.5 Conclusion and Future Work

In summary, using second harmonic generation the electronic nature of $IrTe_2$'s temperature dependent charge ordered/structural transition was investigated. A sharp transition was observed in the second harmonic when cooling accompanied by hysteric behavior upon warming. RASHG measurements imply that the transition changes the surface symmetry from C_{3v} in the high temperature phase to S_2 in the low temperature phase. In the case for SHG, the phase transition is immediate within the temperature resolution. Comparing the second harmonic transition to the structural transition measured by neutron scattering, the surface electronic transition is four times shorter, meaning that relative to a slower bulk the surface electrons react much faster in temperature. Due to the immediate nature of the surface electronic transition seen though SHG, the electronic transition seems to precede the structural transition.

The next step in this project is to measure the RASHG at low temperatures around and after the 280 K transition as well as repeat the previous transition under ultra-high environments. To do this, the UHV system and RASHG design proposed in Section 2.3 is being constructed. This setup will allow us to also cleave in the [5 $\times$ 1] phase and compare, where the Fermi surface (Fig. 3.9(a)) shows enhanced two-dimensional behavior compared to the [5 $\times$ 1]. By studying all the phase transitions using RASHG and LEED with a true clean surface, uncertainties imposed by surface oxidation and reconstruction will be avoided. This can also be extended to look at the phase transition/superconductivity relation using RASHG to observe changes in the electronic symmetry and phase transition with doping.

Chapter 4
Ultrafast Carrier Dynamics and Acoustic Phonons in $La_{0.67}Sr_{0.33}MnO_3/SrTiO_3$ Heterostructures

The following chapter uses ultrafast time-resolved spectroscopic techniques to study new novel dynamics and acoustic phonons in thin film heterostructures.

4.1 Introduction to Transition Metal Oxides

Transition metal oxides (TMOs) are a class of materials distinguished by their physical properties and functionality arising from complex interplay between transition metal ions and oxygen atoms. When combined with oxygen atoms to make a compound, coupling between the d bands and oxygen p bands produce opposing interactions within the band structure. Competition between Coulomb repulsion (localizing effect) and hybridization with the oxygen p bands (delocalizing effect) greatly affects the electron mobility in the system [65]. Small changes in either the ion or the oxygen tunes the bandwidth creating a new ground state and vastly different structures, phases, and properties. The functionality results from nonlinear coupling between charge, orbital, spin, and lattice degrees of free-

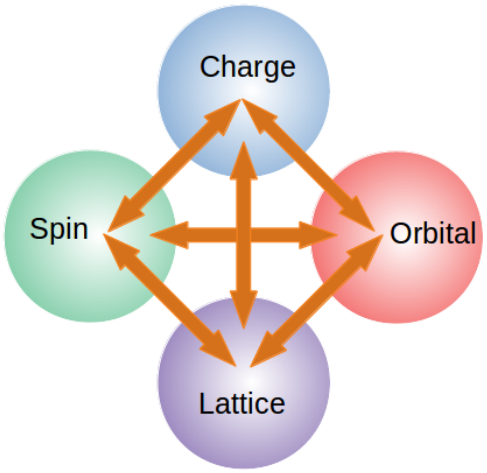

Figure 4.1: Nearly degenerate ground states in transition metal oxide compounds leads to coupling between charge, spin, orbital, and lattice degrees of freedom.

The work in this chapter is published as: J. E. Taylor, R. A. Khoury, K. Zhao, M. Saghayezhian, L. H. Haber, E. W. Plummer, "Ultrafast Carrier Dynamics in Self-Assembled $La_{1-x}Sr_xMnO_3$ Heterostructures," Frontiers in Optics / Laser Science, OSA Technical Digest (Optical Society of America, 2018), paper JW3A.47 [64].

dom, as illustrated by Fig. 4.1. An outcome of these coupled degrees of freedom are unusual properties such as colossal magnetoresistance in manganites[1] [66], two-dimensional electron gas at interfaces [67], metal-insulator transitions, Mott insulator states [68], magneto-elastic coupling, electronic phase separation, etc. Explaining the interplay among electron correlations proves very challenging. It is often necessary to produce materials with high-quality under growth conditions such that individual couplings can be manipulated, in order to understand why new properties emerge. Interfaces between two different TMO materials are even more fascinating producing phenomena that can not be found in bulk compounds alone namely two-dimensional electron gas at interfaces [67], high-T_c superconductivity between insulating oxides [69], and multiferroic behavior [70].

4.1.1 Perovskite and Thin Films

Perovskites are a special class of TMOs with the general formula ABO_3. Rare earth atoms populate the A site while B sites are populated by transition metal cations. Six oxygen atoms form a BO_6 oxygen octahedra around each B site atom. Perovskites can

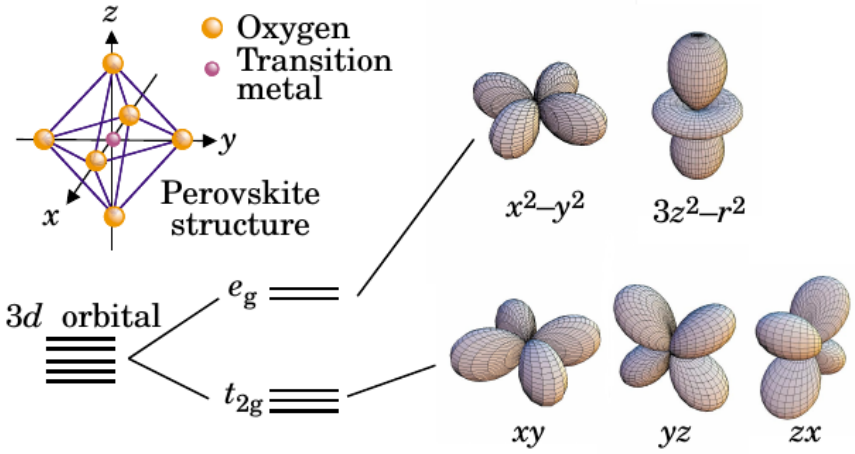

Figure 4.2: Schematic of the octahedra in the perovskite structure, where the red sphere is the central transition metal and orange spheres are the oxygen atoms. In a localized molecular orbital picture, the $3d$ orbital of the transition metal is split by the crystal field into the e_g and t_{2g} orbitals. Figure from Ref. [65].

[1] Albert Fert and Peter Grünberg were jointly awarded the Nobel Prize in Physics in 2007 "for the discovery of Giant Magnetoresistance."

form many different structural symmetries due to the tilt and rotation of the oxygen cage[2]. Not only does the octahedron cage dictate the structure of the perovskite, but it also determines the phonon and electronic band structure and excitation spectra. The network of oxygen atoms creates crystal field which splits the five-fold degenerate $3d$ orbital into the higher energy two-fold e_g (x^2-y^2 and $3z^2$-r^2 orbitals) and lower energy three-fold degenerate t_{2g} (xy, yz, and zx orbitals), schematically in Figure 4.2 [65]. Depending on the compound, elongation of the octahedra can occur which further split the degeneracy of the e_g and t_{2g} orbitals, known as a Jahn-Teller distortion.

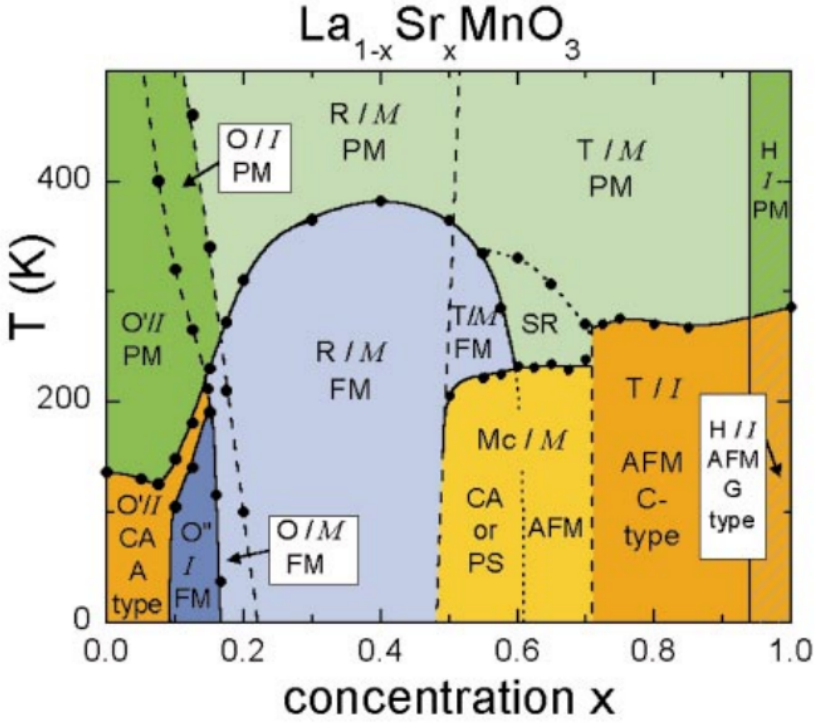

Figure 4.3: $La_{1-x}Sr_xMnO_3/SrTiO_3$ bulk phase diagram as a function of temperature and strontium concentration. PM, FM, AFM, CA - paramagnetic, ferromagnetic, antiferromagnetic, canted antiferromagnetic. I, M - insulating, metallic. O, R, H, T, Mc - orthorhombic, rhombohedral, hexagonal, tetragonal, monoclinic. Solid lines designate phase boundaries. Figure adapted from Ref. [72].

[2]23 unique oxygen octahedral tilt combinations encompassing 15 different space groups have been identified, motivating A. Glazer to develop a classification method just for structural identification based on tilt alone [71].

$La_{1-x}Sr_xMnO_3$ (LSMO) is a perovskite manganite of great interest due to a wide array of physical properties and phases achievable through A site chemical substitution. To demonstrate this point, the bulk phase diagram is displayed in Figure 4.3 [72]. Beginning with the parent compound $LaMnO_3$ (x=0), increasing the concentration of strontium doping evolves the electronic, magnetic, and structural phases simultaneously. In the ground state $LaMnO_3$ is an antiferromagnetic insulator with an orthorhombic structure, but when 20% strontium is introduced, it is now rhomboheral, metallic, and ferromagnetic. Among manganites, $La_{0.67}Sr_{0.33}MnO_3$ is special in that it has the highest Curie temperature (extending past room temperature), near 100% spin polarization [73] and half-metallicity [74].

Confining perovskites to thin films heterostructures is a major interest of material scientists, generating new functionality manifested from broken symmetry and dimensional confinement. Manipulation of the octahedral cage alters the B-O-B orbital overlap altering the bands and orbital occupancy near the Fermi energy. A proven method to accomplish this is through strain tuning. Strain tuning consists of systematically controlling material properties through means including: lattice mismatch between the substrate and film, A or B site doping, film thickness, etc. New properties such as a thickness dependent metal-insulator transition [75] and reemergent magnetic order [76] have been observed in thin films, and interface properties can even dictate properties in the bulk film [21]. Here at LSU, we have the ability to grow high-quality thin films, which are characterized with atomically-resolved electron microscopy, as well as macroscopic characterization of physical properties, allowing a rich playground for our research.

4.2 $La_{0.67}Sr_{0.33}MnO_3/SrTiO_3$ Heterostructures - Physical Properties

Our research group at LSU has grown epitaxial $La_{0.67}Sr_{0.33}MnO_3$ on $SrTiO_3$ (001) substrates (LSMO/STO)[3] using pulsed laser deposition focusing on the growth process. During growth, defects (oxygen vacancies) are manipulated through changes in the ambient oxygen pressure generating various functional behavior not reported before for LSMO/STO

[3]Throughout the remainder of this thesis LSMO/STO is always assumed to be at x=33% concentration unless stated otherwise.

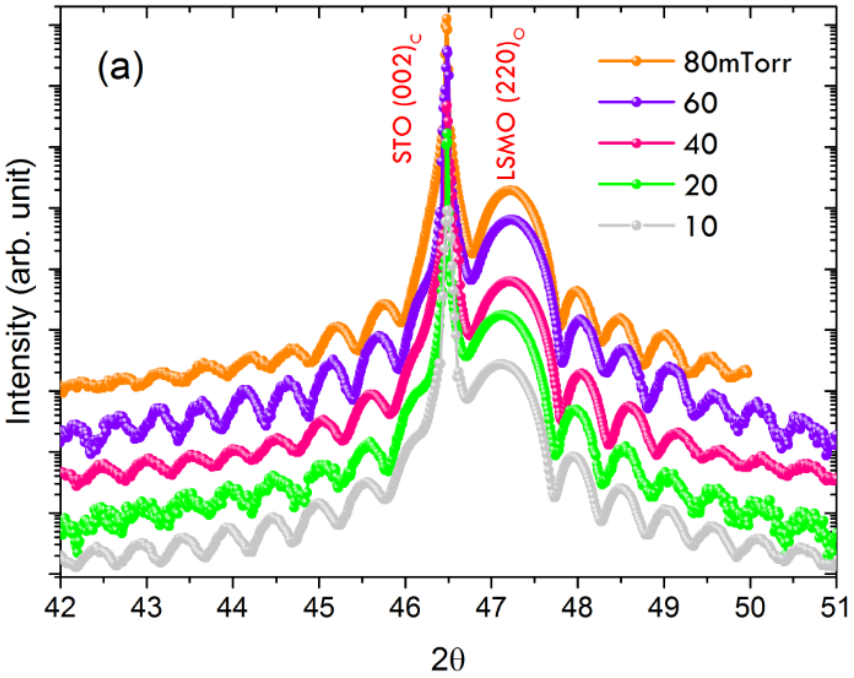

Figure 4.4: X-ray diffraction as a function of growth oxygen pressure for LSMO/STO heterostructures. Well-defined fringe peaks surrounding the STO (002) and LSMO (220) peaks indicate high-quality film growth with a sharp interface. Figure adapted from Ref. [77]

thin films. Typically, LSMO/STO is grown under 80 mTorr oxygen pressure, however, at LSU we have successfully grown LSMO/STO down to 10 mTorr. X-ray diffraction as a function of oxygen pressures is shown in Figure 4.4. From the XRD, there are three features: the STO (002) substrate peak, the LSMO (220) film peak, and surrounding fringe peaks. Sharp well-defined fringe peaks prove high-quality layer-by-layer film growth with a good interface. Most important is that macroscopic measurements show no substantial change in microscopic structure, apart from an increasing lattice constant with decreasing oxygen pressure. These are all high-quality epitaxial films.

In sharp contrast to the XRD data, atomically-resolved electron microscopy show a fundamental difference in films grown with different oxygen pressure. Figure 4.5(a)&(b) are atomically-resolved high-angle annular dark field STEM (HAADF-STEM) and angular bright field STEM (ABF-STEM), out-of-plane lattice constant (OOP), and oxygen octahedral tilt (OOT) for 40 mTorr and 80 mTorr oxygen pressure LSMO/STO samples

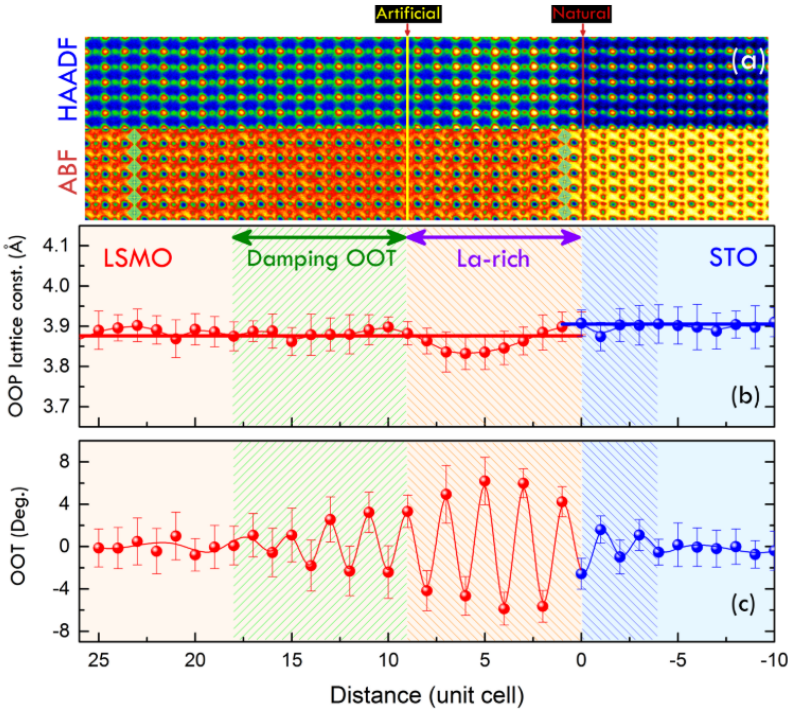

(a)

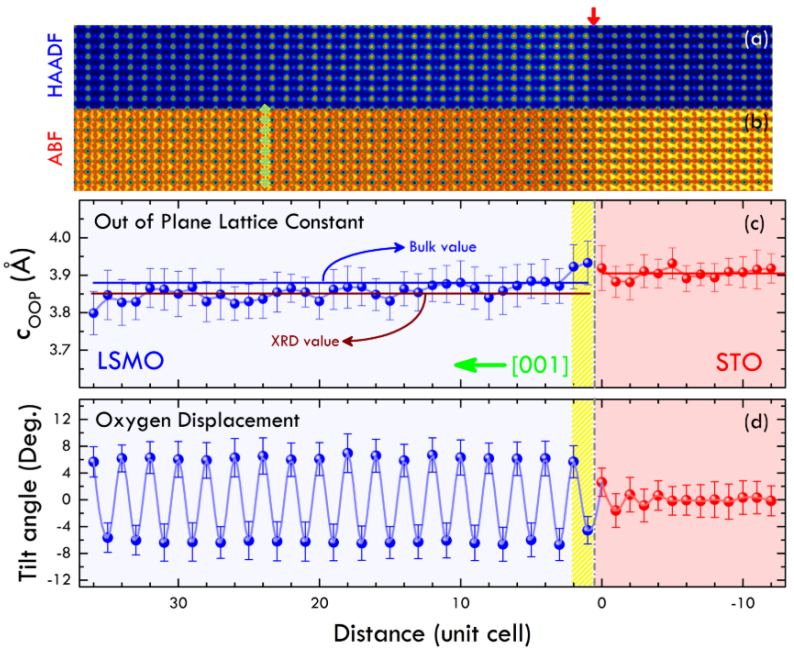

(b)

Figure 4.5: $La_{0.67}Sr_{0.33}MnO_3/SrTiO_3$ scanning transmission electron microscopy (STEM) showing the bight field, dark field, out-of-plane (OOP) (c-axis) lattice constant, and oxygen octahedral tilt (OOT) under two growth conditions. (a) 40 mTorr oxygen pressure. (b) 80 mTorr oxygen pressure. Figures adapted from Ref. [77]

respectively [77]. By comparison, the two samples possess drastically different structures, especially near the interface. Near the interface for 40 mTorr grown LSMO, HAADF-STEM shows increased La stoichiometric concentration from 0 uc to 7-8 uc above the interface. Coinciding is a decrease in the out-of-plane lattice constant throughout the lanthanum rich region. Measurements of the oxygen octahedral tilt (OOT) reveal that the decrease in OOP is due to the large 6° variation in OOT. As the film becomes thick (above 18 uc), tilt dampens and stabilizes the *c*-axis lattice constant to the bulk value.

STEM for 80 mTorr is very different with a constant alternating OOT progressing throughout the entirety of the thin film. There are no regions of extreme stoichiometric gradients. An apparent outcome specific to low oxygen pressure growth is the formation of a pseudo-multilayer inside the thin film between the natural STO interface and the "artificial" interface (area of stoichiometric lanthanum). As discussed in Sec. 4.1, physical changes of the MnO_6 octahedron plays a major role in the electronic magnetic properties of perovskite manganites, and the different structural and chemical compositions near the interface imply that physical properties differ drastically between these LSMO samples.

In general, ferromagnetism in itinerant metallic systems requires a spin-resolved band structure calculation. However, the mechanism as applied to LSMO can be understood by a simple chemical model governed by interplay between the $LaMnO_3$ Mn^{3+} and $SrMnO_3$ Mn^{4+} oxidation states. To compensate and lower the total energy, the oxygen p orbitals in the B-O-B network acts as a medium for Mn ion sharing between the e_g orbitals. This interaction is called the double-exchange. Electronically, the density of states shift to the $d_{x^2-y^2}$ orbital, which favors antiferromagnetic ordering [75]. For 40 mTorr growth conditions, spontaneous magnetic reversal (SMR) and inverted hysteresis (IH) are both present below the Curie temperature T_c, due to the interface reconstruction and antiferromagnetic interaction. LSMO grown under normal conditions does not have spontaneous magnetic reversal or inverted hysteresis, only a ferromagnetic state that increases with temperature [77].

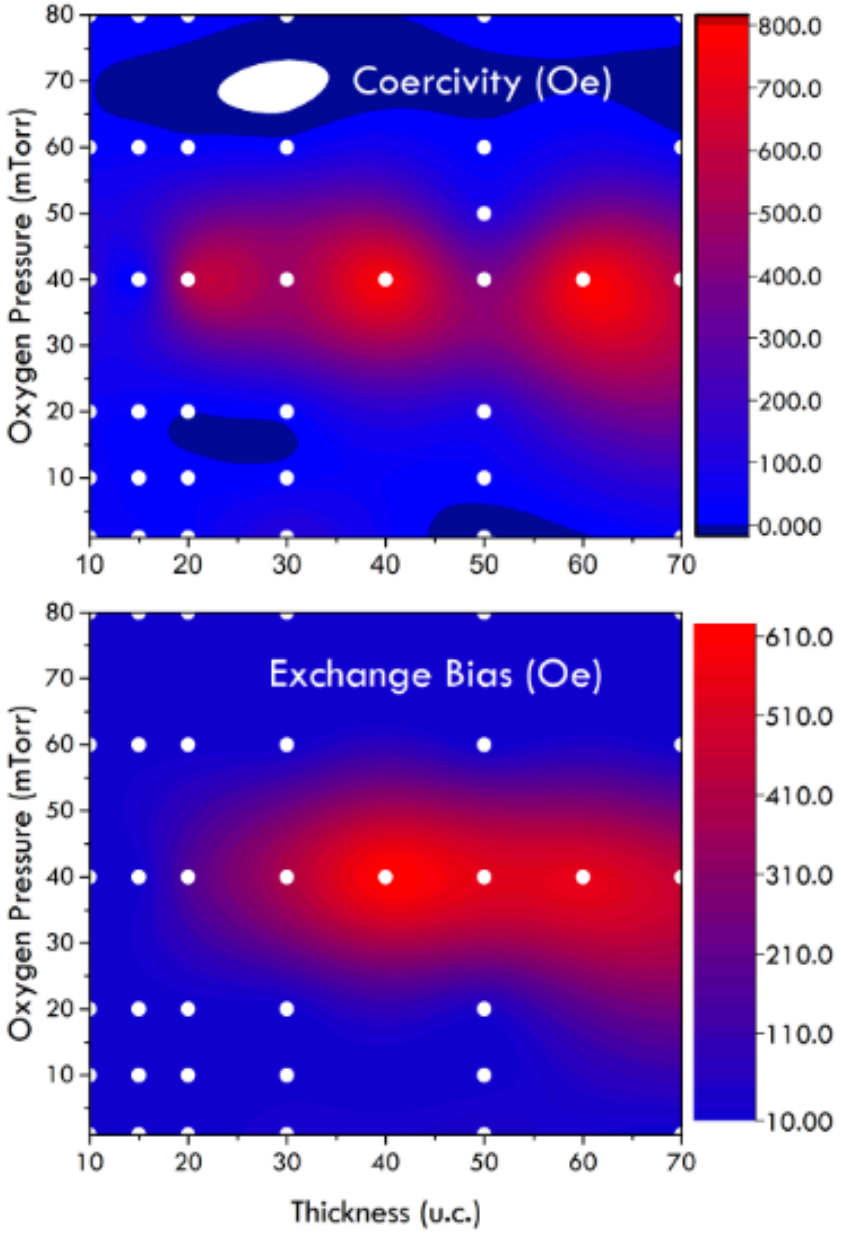

Figure 4.6: 50 uc $La_{0.67}Sr_{0.33}MnO_3/SrTiO_3$ magnetic phase diagrams for exchange bias and coercivity as a function of LSMO unit cell thickness and oxygen growth pressure. Emergence of coercivity and exchange bias are only present above 20 unit cells when grown in a small range of oxygen pressures around 40 mTorr. Figure adapted from Ref. [77]

All of LSMO physical properties discussed so far only exist within a narrow window of LSMO thickness and oxygen pressure. By growing and testing many films, a thickness and oxygen pressure phase diagram was able to be constructed for the interface exchange bias and coercivity presented in Figure 4.6. At low numbers of LSMO unit cells (below 20 uc), both coercivity and exchange bias are absent. Once 20 uc thickness is achieved, exchange bias and coercivity reemerge. Deviations in oxygen pressure away form 40 mTorr also remove these properties.

Based off the interaction between the hard antiferromagnetic interface layer and the soft ferromagnetic bulk, LSMO shows great promise for a spin-like mechanism in a magnetic switching device. For devices used in electronic applications, understanding the thermoelastic properties are essential for implementation. Using ultrafast dynamics, carrier dynamics and their subsequent lattice coupling can be characterized, providing in principle information about elastic properties and thermal diffusion of excited electrons to new ground states.

4.3 Ultrafast Pulse Interactions With the Electrons and Lattice

Bulk light-matter interactions are well described classical phenomena governed by the Fresnel equations where material properties such as the index of refraction explains a majority of the behavior. For small energy densities (continuous wavelength laser) the rate of electronic excitation is very low, so low that the rate of relaxation is slower than the typical electron-phonon coupling times [78]. At slow electronic excitation rates, thermal diffusion from the electrons to the lattice is negligible, and characterizing the lattice diffusion alone is sufficient for understanding heat transport. However for pico and femtosecond pulses, the energy density of each pulse can be greater than six orders of magnitude larger than continuous wavelength lasers of the same average energy density [79]. In combination with the large energy density, the temporal width of the pulse is much smaller than lattice response time. As a result, the energy of the pulse is absorbed by the near surface electrons, generating a highly nonequilibrium distribution around the Fermi energy, similar to

the density of states shown in Figure 4.7(a) [79]. The maximum energy of the displaced density of states depends on the absorbed photon energy $h\nu$. Energy is absorbed by the surface electrons up to the penetration depth of a material, ζ

$$\zeta = \frac{\lambda}{2\pi k} \tag{4.1}$$

where k is the imaginary portion of the index of refraction and λ is the wavelength of the laser.

Initially following excitation, excited electrons undergo ballistic motion. During ballistic motion, electrons propagate deep into the bulk at speeds near the Fermi velocity ($\approx 10^6$m/s) and dissipate their energy through inelastic collisions. Ballistic range for electrons is estimated to be on the order of optical penetration depth for metals[4]. After ballistic motion and energy dissipation, near Fermi level electrons thermalize to form a hot electron bath near the surface, with a thermal gradient (nanometer range for metals) directed away from the surface into the bulk traveling at speeds less than (10^4 m/s) (Figure 4.7(b)). Through thermal diffusion, electrons normalize to some temperature T_e. At this time, electrons near the Fermi level still have the largest change in occupancy, where the total occupancy change is $2kT_e$ [81]. Since the lattice does not have time to respond and thermal diffusion through electron-electron collisions are independent of the lattice, the system can be described now by two independent baths: an electron bath at T_e and a lattice bath of T_l. For metals, the increased number of free carriers allows for very quick electron diffusion.

Finally, these two baths begin to couple as the hot electron bath begins to redistribute its remaining energy into the lattice via electron-phonon coupling. The much hotter electron bath slowly diffuses through the lattice, creating a heat diffusion wave into the bulk, subsequently raising the lattice temperature (albeit much less than the initial electron temperature). Figure 4.7(c) demonstrates this interaction. Through diffusion, electrons and lattice reach thermal equilibrium and the final excited density of states around the Fermi

[4]For reference, ballistic transport in gold has been reported as deep as 100 nm [80]

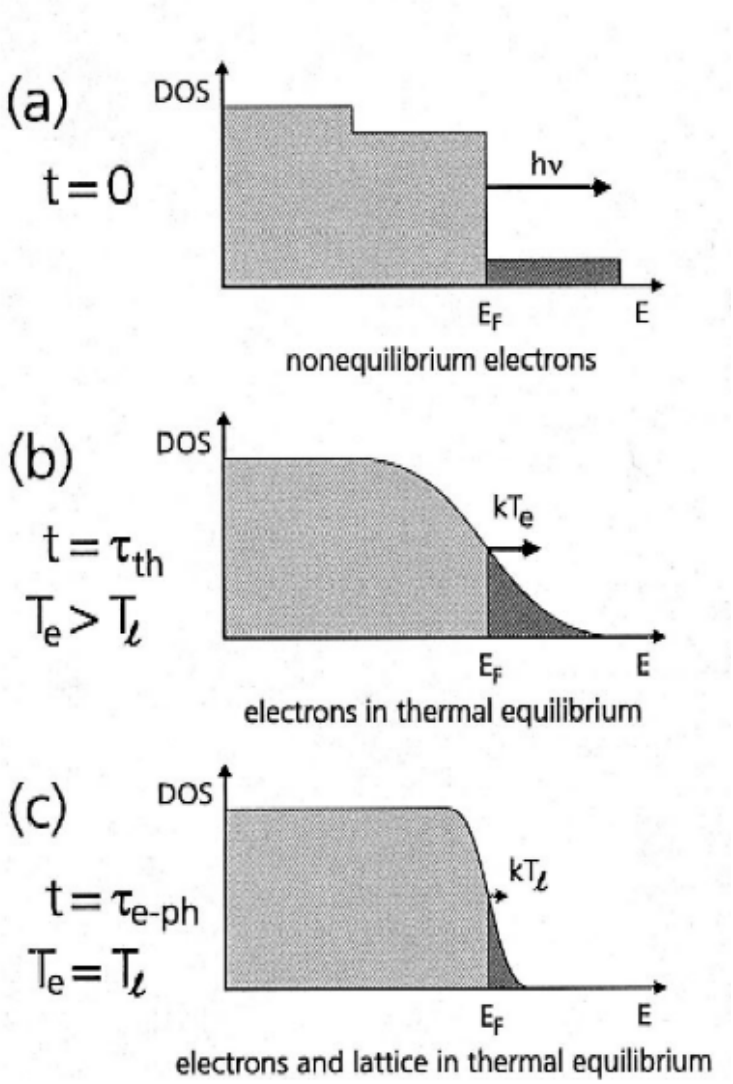

Figure 4.7: Schematic representation of the material response following ultrafast optical pumping. (a) At time zero, the density of states becomes highly nonequlibrium following photoexcitation. (b) Electron temperature normalizes, partially relaxing the density of states around the Fermi level. (c) Resulting density of states after electrons have reach thermal equilibrium with underlying lattice. Figure adapted from [79]

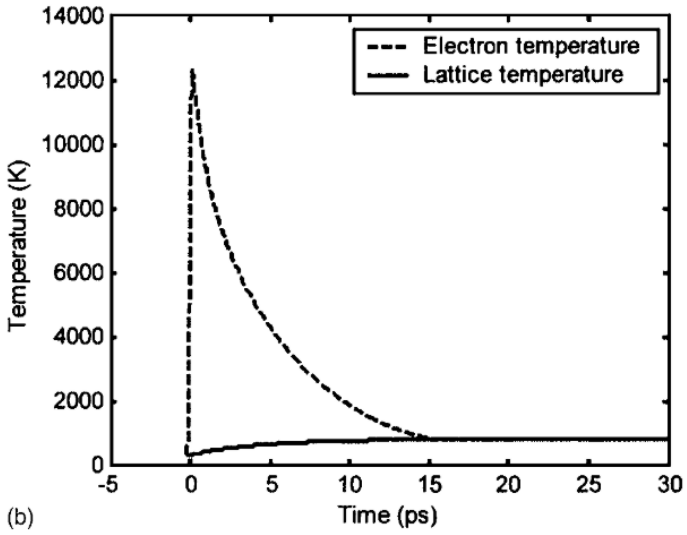

Figure 4.8: Schematic example of the temperature evolution of the electrons (dashed line) compared to the lattice (solid line). The electronic temperature reacts immediately at time zero and redistributes energy back into the lattice. Figure adapted from [82]

level is dictated by the final lattice temperature T_l. The interplay between the electron temperature and lattice temperature is demonstrated by Fig. 4.8. Photoabsorption by the electrons can increase the electronic temperature orders of magnitude larger than the lattice. Thermalization of the electrons is much faster, largely due to the increased mobility of the carriers and probability of scattering .

To capture this description in a quantitative model, Anisimov et al. in 1974 proposed the two-temperature model [83]. The two-temperature model attempts to decouple the competition between the excited electrons produced via the photoelectric effect and the thermal decay processes listed above. Under the two-temperature model we must assume that T_e and T_l are much larger than the Debye temperature but much smaller than the Fermi temperature. Furthermore, we are worried about gradients perpendicular to the surface which are much larger than parallel gradients. Based off the two-temperature model when a pulse hits a material surface, it induces a dynamical coupling between the near Fermi level electrons and the underlying lattice. Initially free electrons within the optical penetration depth are excited by the optical pulse. The surface provides a source of

momentum such that momentum is conserved. These responses are modeled by the time coupled equations:

$$C_e(T_e)\frac{\partial Te}{\partial t} = \nabla[k_e(T_e)\nabla T_e] - G(T_e - T_l) + S(z,t) \quad (4.2)$$

$$C_l(T_l)\frac{\partial T_l}{\partial t} = G(T_e - T_l) \quad (4.3)$$

where C_e and C_l are the heat capacities of the electrons and lattice, G is the electron-phonon coupling constant[5], S is the laser source term, and k_e is the free electron heat conductivity derivable through Drude modeling. The laser source term is dependent on the spatial and temporal profile of the laser pulse. In general these coupled equations must be solved numerically, although due to complexities in modeling most materials, direct extraction of time dependent heat capacities and electron lattice temperatures is still very challenging. There are of course significant drawbacks in the two-temperature model for metals as the two-temperature model can not accurately describe high fluencies where the electron temperature approaches the Fermi temperature [82]. Most importantly in a metal the excitation is resonant all the time.

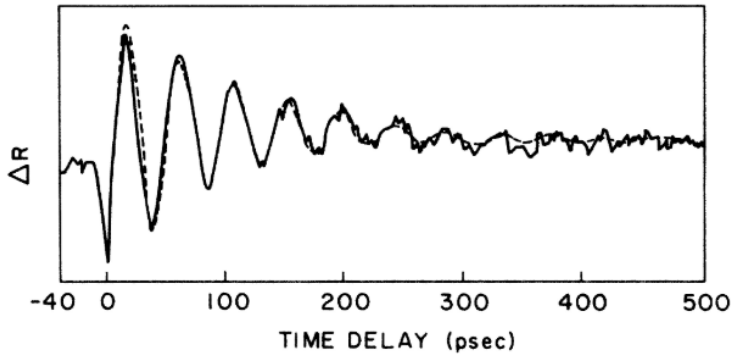

Figure 4.9: Change in reflectivity in bulk α-As_2Te_3 with an oscillation period of 44.8 ps. Figure adapted from Ref [84]

4.4 Generation of Coherent Acoustic Phonons

Coherent generation of phonons has been demonstrated in a large variety of materials in the GHz to THz range. The first report of coherent longitudinal acoustic phonons was conducted by C. Thompsen and collaborators in 1986, where modulations in the optical reflectivity with a period of 44.8 ps were observed in α-As_2Te_3, see Figure 4.9 [84].

In broad terms, the generation of acoustic phonons can be described as follows. The initial impact of the pump beam provides a momentum transfer from the pulse (at the surface which is a source of momentum) in addition to the quick photoabsorption by the electrons. Once the pump strikes the sample, a coherent longitudinal acoustic wave is created at the surface, illustrated as the dashed line in Figure 4.10. The strain from the acoustic wave in turn modulates the physical properties (i.e. refractive index, dielectric, susceptibility, etc.) of the material as it propagates. The acoustic wave travels deep into the bulk at the speed of sound, which can be described by Eq. 4.4 as a function of the

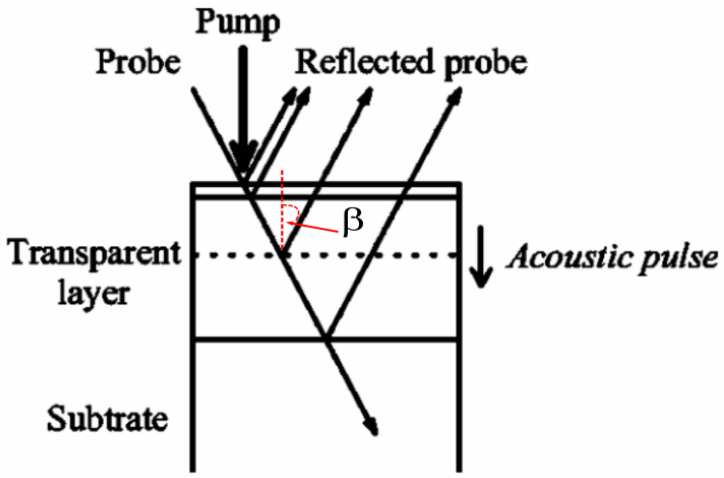

Figure 4.10: Schematic of the detection of acoustic pulses with an optical probe. As the acoustic pulse (represented by the dotted line) traverses from the surface to substrate modulating the refractive index, the optical probe reflects off the acoustic pulse at different depths. Pulse interaction does not alter the angle of the reflected probe, only the intensity. Figure adapted from Ref [85].

[5]For metals, G is approximately 1- 1000 x 10^{15} W m^{-3} K^{-1}.

wave vector q and oscillation frequency f,

$$v_s = \frac{2\pi f}{q}. \tag{4.4}$$

The phonon wave vector given by Eq. 4.5 is only dependent on the refractive index n and the energy of the probe λ_p. β refers to the probe angle with respect to the interlayer reflection off the coherent phonon relative to the surface normal.

$$q = \frac{4\pi n \cos(\beta)}{\lambda_p} \tag{4.5}$$

When the probe pulse interacts with longitudinal acoustic waves in the bulk, the probe pulse and acoustic pulse interact interferrometicly such that the acoustic pulse modulates the intensity of the probe. The change in the probe pulse reflection due to interaction with the acoustic pulse is referred to as Brillouin backscattering. Detecting acoustic phonons is accomplished indirectly through the changes in the probes wave vector coupling to the phonon wave vector at various points inside the bulk. As the acoustic pulse propagates the

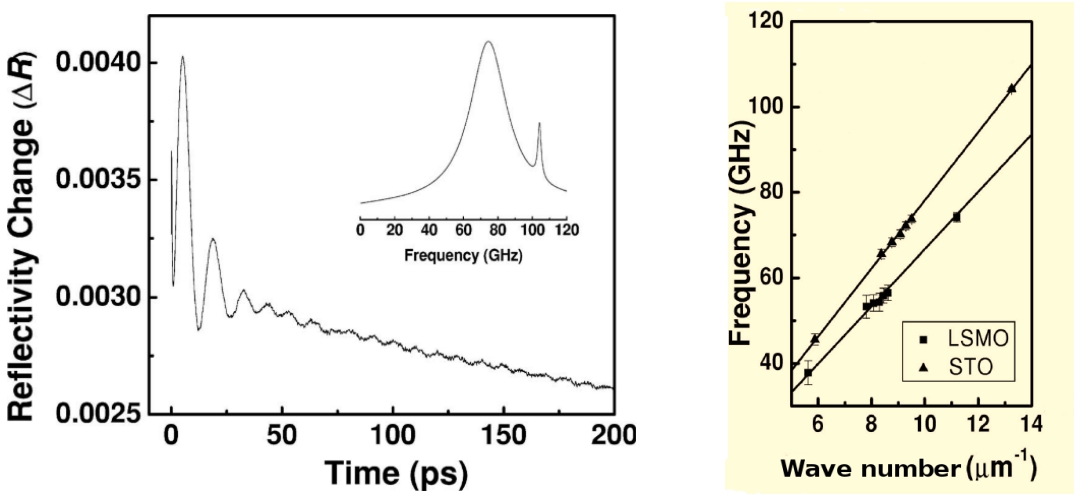

(a) (b)

Figure 4.11: Transient reflectivity for 200 nm LSMO/STO heterostructures at 295 K. (a) Time-resolved reflectivity change with acoustic phonon oscillations. Inset is the fast Fourier transformation of the reflectivity with frequencies of 74.2 and 104.2 GHz (b) Longitudinal acoustic phonon dispersion of LSMO/STO films. Figure adapted from Ref [86].

strain field modulates the refractive index in an oscillatory nature while slowly dephasing. After interacting with the probe pulse, acoustic phonons appear as the change in reflectivity as damped sinusoidal functions of the form given in Eq. 4.6.

$$S(t) = Ae^{-\frac{t}{\tau}} \sin(2\pi t f + \phi) + y0 \tag{4.6}$$

In Eq. 4.6, A is the amplitude and scales with the intensity of the pulse, τ is the damping time, f is the Brillouin oscillation frequency, ϕ is the phase, and $y0$ is the offset.

For optical setups that allow tunable probe photon energy, the linear phonon dispersion near the Brillouin zone center can be mapped. Acoustic phonons near zone center will have a linear dependence of the phonon oscillation frequency f vs phonon wave vector q with the slope being the sound velocity in Eq. 4.4. A beautiful example is the work conducted by Ren et al on LSMO/STO heterostructures [86]. Using probe energies from 3.1 eV (400 nm) to 2.16 eV (547 nm) transient reflectivity measurements for 200 nm thick thin films display characteristic oscillatory patterns of acoustic phonon generation. One of these curves using a 400 nm prove is shown in Figure 4.11(a) with the inset being the fast Fourier transform of the reflectivity. From the fast Fourier transform, two oscillation frequencies are identified. Figure 4.11(b) is the probe energy dependence of each frequency. The slope of each linear phonon dispersion gives the sound velocities of $\mathrm{v}_{LSMO} = 6500 \pm 300$ m/s and $\mathrm{v}_{STO} = 7800 \pm 100$ m/s.

4.4.1 Types of Coherent Acoustic Phonons

Acoustic phonons formed from elastic modulation of the bulk can be model with semi-classical theory. Bulk motion can described by a classical damped harmonic oscillator while the optical pulse source term requires a quantum approach. Overall the equation of motion in one dimension can be written as Eq. 4.7,

$$\frac{\partial^2 u}{\partial t^2} - C_\alpha^2 \frac{\partial^2 u}{\partial z^2} = \frac{1}{\rho} \frac{\partial \sigma(z,t)}{\partial z} \tag{4.7}$$

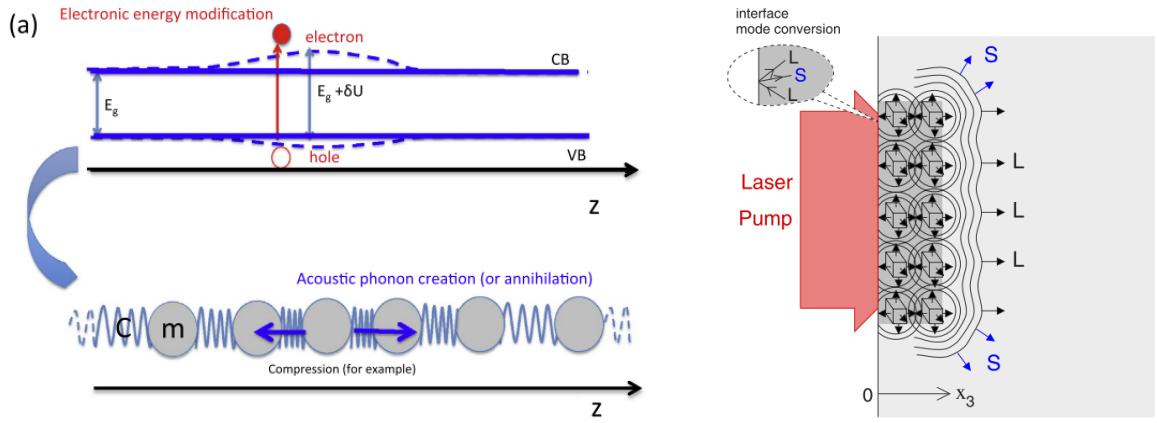

(a) (b)

Figure 4.12: Schematic diagram of coherent acoustic photon generation (a) Deformation potential process - Photoabsorption alters the electronic distribution near the Fermi energy changing the electronic potential felt by the lattice and creating phonons. Figure adapted from Ref [87]. (b) Thermoeleastic process - Photoabsorption heats the electrons generating a thermal expansion in the lattice. Longitudinal coherent oscillations serve as decay channels for energy dissipation in the collinear direction to the laser pump. Figure adapted from Ref [88].

where u, ρ, and σ are the particle displacement, mass density, and photoinduced stress [87]. For Eq. 4.7, the photoinduced stress term encompasses all microscopic mechanisms for coherent acoustic phonon generation, the two most common are deformation potential and thermoelastic stress. In metals with highly mobile itinerant electrons, thermoelastic stress is the more common method, while the deformation potential model is more common in semiconductor systems.

Under the deformation potential model, photoexcited electrons at the surface in combination with the momentum transfer from the impact of a laser pulse couple to the lattice and create an elastic compressive strain parallel to the surface normal. From a chemistry perspective, the change in electronic density by creation of electron-hole pairs near the Fermi energy modify the orbital overlap and bond angle, in turn displacing the lattice and creating phonons. On a macroscopic scale, a long range lattice deformation resembling standing waves propagate from the surface to the substrate, represented in 4.12(a) [87]. The crystal walls and substrate form a set of boundary conditions for the available stand-

ing longitudinal acoustic standing wave modes. The second mechanism is thermoelastic strain illustrated in Figure 4.12(b). Beginning at the surface, elevated electronic temperatures cause a thermal expansion of the underlying lattice and build up a thermal pressure. Atoms vibrate as a collection of point sources transferring thermal energy to near neighbor sites decaying through acoustic and optical phonon generation. Coherent lattice motion collinear to the pump laser create longitudinal phonons while motion towards the edges of the thermal distribution create shear strains.

4.5 Ultrafast Reflectivity Results and Discussion

Elastic thermal and strain behavior is extremely important for developing functional devices. Coherent acoustic phonon measurements serve a valuable role as complementary bulk analysis of dynamical properties compared to static physical properties characterization such as transport, magnetization, and susceptibility. Elastic properties of metals also reflect the presence of defects, disorder, and interatomic bond altering as changes in the phonon frequency and altered dephasing rates [89]. LSMO/STO as discussed in Sec. 4.2 is an ideal candidate for study due to its unique pseudo-multilayer structure and strongly correlated electron and lattice coupling. LSMO/STO along with other artificially structured materials are frequently investigated by very powerful methods capable of probing the ground state, but an important challenge is to probe excited states, especially those far from equilibrium. With the growth capabilities of LSU, similar materials with different ground state can be created. Ultrafast reflectivity measurements can be used to study these systems in highly non-equilibrium exited states and to observe subsequent dynamical behavior [13, 90] on the timescales of electronic (attosecond) and atomic motion, offering insight on the nature of both elastic properties and phonon behavior. [91].

Using the pump-probe optical setup described in Section 2.4, ultrafast carrier dynamics for 70 uc of $La_{0.67}Sr_{0.33}MnO_3$ on a $SrTiO_3$ substrate capped with 10 uc of $SrTiO_3$ are investigated. Both pump and probe pulses are 800 nm (1.55 eV) photons and the probe energy was held at a constant power of 5 μJ. The pump power varied 40 μJ to 8μJ with a

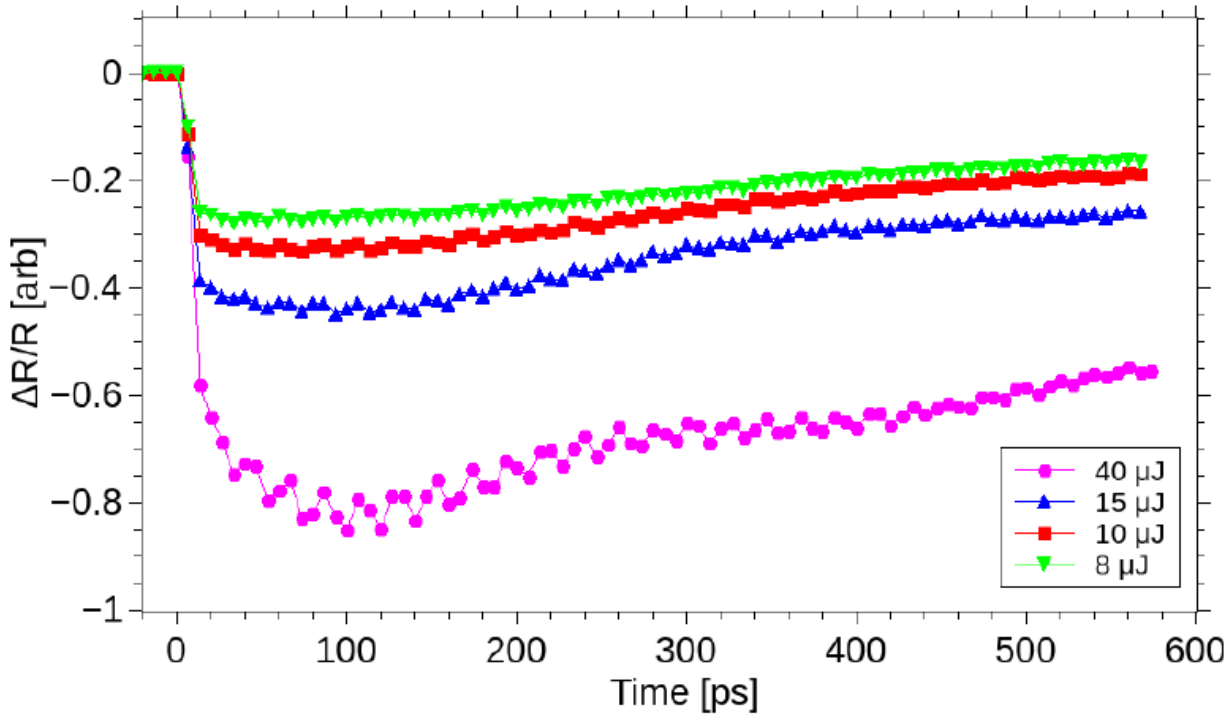

Figure 4.13: $La_{0.67}Sr_{0.33}MnO_3/SrTiO_3$ reflectivity for various pump powers. Pink circles, blue triangles, red squared, and green inverted triangles correspond to 40 μJ, 15 μJ, 10 μJ, and 8 μJ pump powers respectively. Plots are normalized to the peak value of 40 μJ.

neutral density filter. The probe was normally incident and the pump was approximately 45° with respect to the surface normal. Time steps of 6.66 ps were selected to time-resolve the low frequency coherent oscillations. Optimizing the time steps for probing long time-scales creates a trade-off in decreased signal-to-noise for resolving faster oscillation frequencies. Optical conductivity measurements by Quijada et al report a broad absorption peak centered around 1.55 eV assigned to the excitation from the Jahn-Teller split Mn e_g band [92]. Determination of positive or negative change in reflectivity depends on the probe radiation energy relative to the intraband transition. In this case, the pump and probe wavelength both correspond to a direct excitation, therefore absorption of the probe pulse will cause a decrease in the reflected signal.

Figure 4.13 shows all of the reflectivity curves for each pump power. An obvious feature is the power dependence of the initial intensity at time-zero, which is a direct outcome of the increased energy density of the optical pump creating a larger number of

absorbed electrons. Ballistic electron motion occurs very quickly (order of 10s to 100s of femtoseconds) so we assume fast electron processes occur within an individual time step and is excluded from further discussion. The second key feature is the appearance of a delayed $\Delta R/R$ peak with increasing pump power, denoted as a rise time originating from a delay in the electronic-lattice thermalization when using large optical energy densities. Beginning at time-zero, oscillations are superimposed throughout and are independent of the electronic behavior, occurring prior to completion of electronic thermalization.

To isolate the superimposed coherent oscillations, the reflectivity was fit to an exponential decay model and subtracted. To fit, the three term exponential decay in Eq. 4.8 was used, starting at time-zero. Due to the significant rise time ($\sim$ 100 ps), a third fast

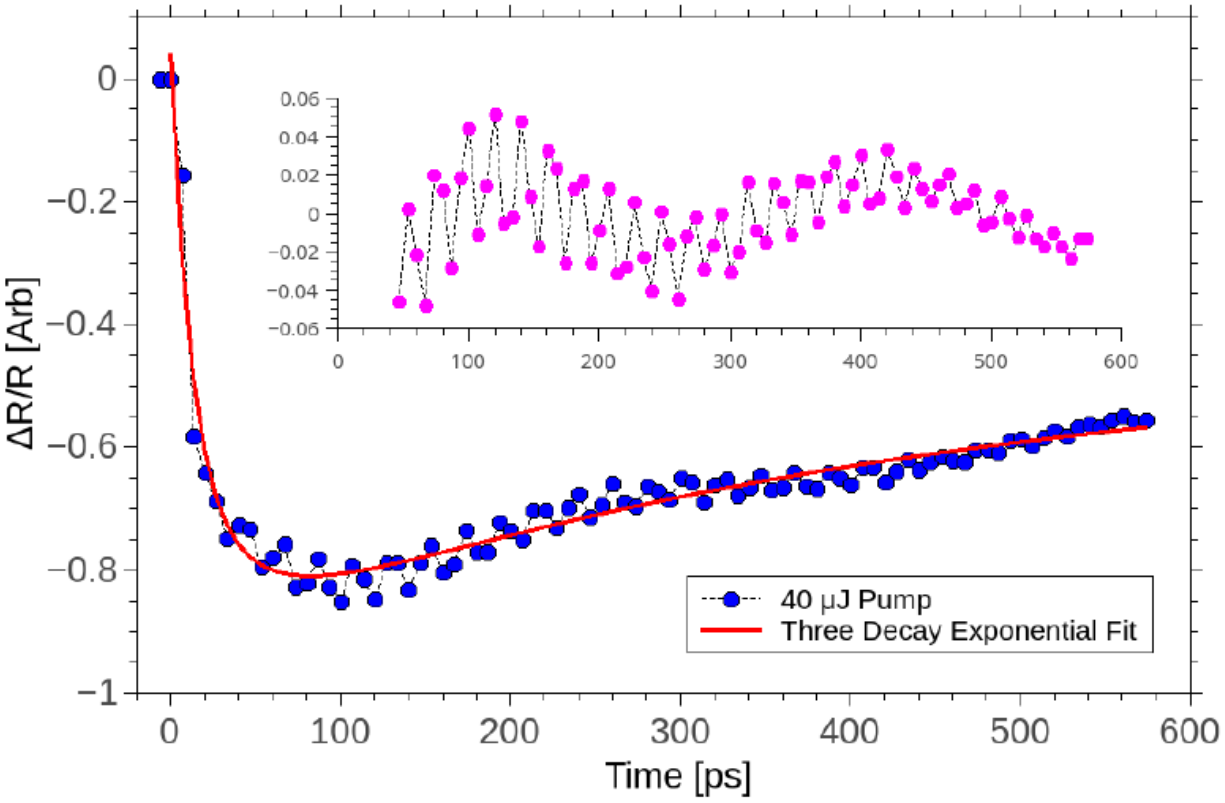

Figure 4.14: $\Delta R/R$ for $La_{0.67}Sr_{0.33}MnO_3/SrTiO_3$ with a pump power of 40 μJ. Blue dots and black dashed lines are the raw data. The red solid line is the three decay exponential fit. Inset: Residuals of the raw data with the subtracted fit.

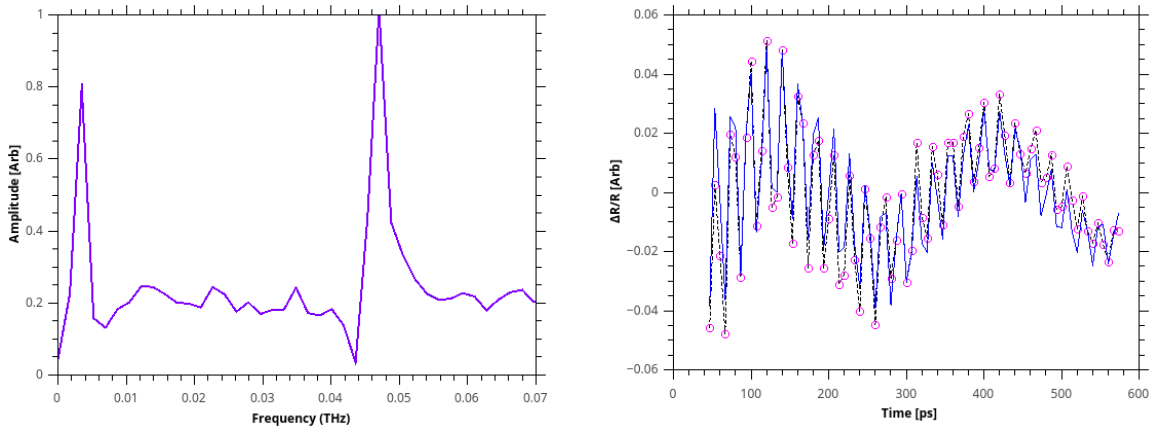

(a) (b)

Figure 4.15: (a) Fourier transforms for the residuals for both the 40 μJ pump power fit. High amplitude frequencies are visible around 46 GHz and 3.6 GHz. (a) Two damping sinusoidal fit for the 40 μJ residuals using the frequencies extracted from the Fourier transform.

exponential must be added.

$$\frac{\Delta R}{R} = \left(A_1 e^{-\frac{t}{\tau_1}}\right)_{fast} + \left(A_2 e^{-\frac{t}{\tau_2}} + A_3 e^{-\frac{t}{\tau_3}}\right)_{slow} \tag{4.8}$$

In principle, the two temperature model is reliable after electron thermalization completes, and due to the addition of coherent oscillations, the exact time for completion has a high degree of uncertainty. Therefore, the fast amplitude and lifetime represent the electronic dynamics prior to thermal equilibrium. The slow dynamics relate to the electron-lattice and lattice decay processes. Long electron rise times and three decay exponential fitting is consistent with previous studies of LSMO/$YBa_2Cu_3O_{7-\delta}$/LSMO heterosctructures [93].

The raw data and exponential decay fit for the 40 μJ pump is shown in Figure 4.14. Time constants of $\tau_1 = 11$ s, $\tau_2 = 35$ s, and $\tau_3 = 400$ s produce a fit with good agreement to the data. By subtracting the exponential fit, the residuals containing the coherent oscillations are obtained and presented as the inset in Figure 4.14. The residuals are comprised of multiple frequencies. From the FFT in Figure 4.15(a), there are two large peaks located at 46 GHz and 3.4 GHz. Discussion on the origin of these frequencies will be discussed after pump power trends are presented. Compared to Re et al in Reference [86], our full

Pump [μJ]	40	15	10	8
τ_1 [ps]	11 ± 5	9 ± 1	8.8 ± 0.9	9 ± 0.6
A_1 [arb]	0.6 ± 0.4	0.41 ± 0.05	0.33 ± 0.02	0.30 ± 0.01
τ_2 [ps]	35 ± 37	40 ± 20	70 ± 30	94 ± 40
A_2 [arb]	0.3 ± 0.4	0.12 ± 0.05	0.09 ± 0.02	0.07 ± 0.02
τ_3 [ps]	400 ± 200	480 ± 40	440 ± 40	430 ± 60
A_3 [arb]	-0.48 ± 0.05	-0.386 ± 0.008	-0.30 ± 0.01	-0.30 ± 0.03

Table 4.1: Exponential fitting parameters for all pump powers.

Pump [μJ]	40	15	10	8
A_1 [arb]	0.046 ± 0.004	0.012 ± 0.002	0.010 ± 0.001	0.007 ± 0.001
f_1 [GHz]	46.41 ± 0.07	46.23 ± 0.09	46.17 ± 0.07	46.24 ± 0.08
τ_1 [ps]	340 ± 50	460 ± 100	420 ± 80	390 ± 80
A_2 [arb]	0.021 ± 0.003	0.020 ± 0.002	0.0061 ± 0.0008	0.0046 ± 0.0007
f_2 [GHz]	3.60 ± 0.01	2.33 ± 0.05	1.87 ± 0.04	1.88 ± 0.04
τ_2 [ps]	2000 ± 1000	470 ± 80	5000 ± 6000	2000 ± 1000

Table 4.2: Decay sinusoidal fitting parameters for all pump powers.

width at half maximum of each peak is significantly more sharp (2-3 GHz) compared to previous Fourier transforms of LSMO phonons (20 GHz) [86]. We can relate this difference to the film quality. For poor quality films, the coherence of acoustic oscillations becomes broadened due to defects and other scattering mechanisms altering the coherent oscillatory frequency in the film [94].

Using the frequencies as initial parameters, the two oscillations were fit using the damping sinusoidal oscillation function in Eq. 4.6. Figure 4.15(b) is the fit of the residuals with the double sinusoidal fit. From the damping sinusoidal fit, the fast oscillation was fit to a frequency of 46 ± 8 GHz with a dephasing time of 330 ± 90 ps and the slow oscillation was fit to frequency of 3.6 ± 0.2 GHz and a dephasing time of 1000 ± 1000 ps. The large uncertainty for the slow oscillation dephasing is most likely due to only having one period to fit. Each of the remaining pump powers were also analyzed in the same manner. Tabulated values for all powers of the exponential fits can be found in Table 4.1 and Table 4.2 for the sinusoidal decay fits.

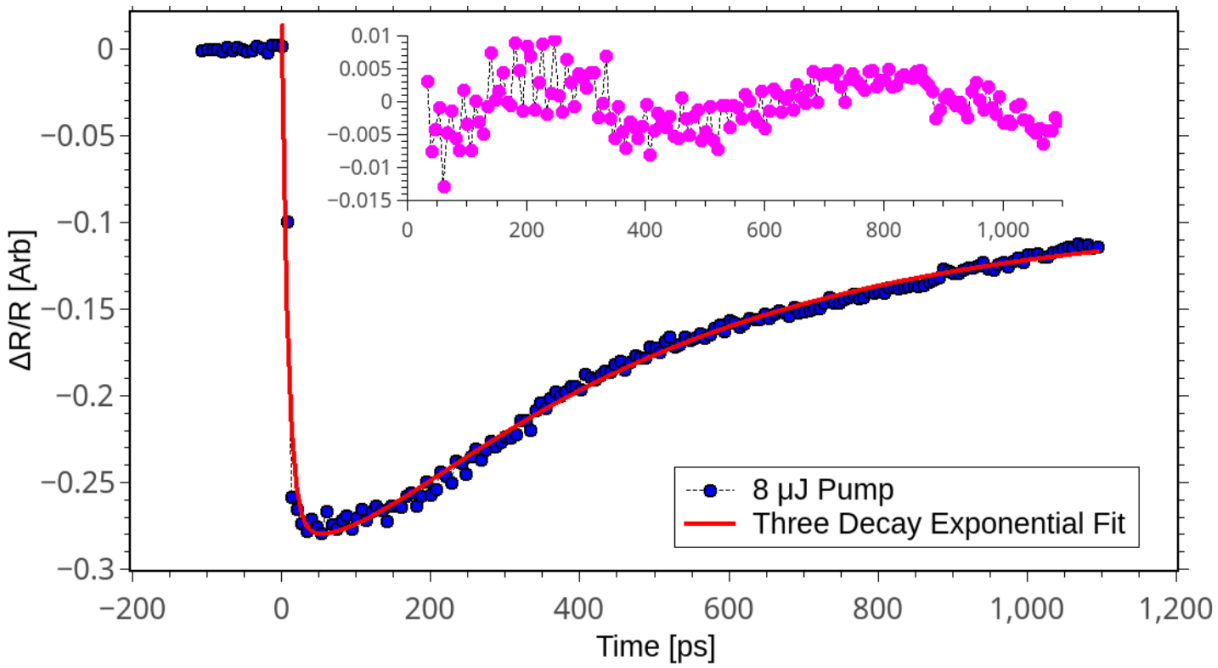

Figure 4.16: $\Delta R/R$ for $La_{0.67}Sr_{0.33}MnO_3/SrTiO_3$ with a pump power of 8 μJ. Blue dots and black dashed lines are the raw data. The red solid line is the three decay exponential fit. Inset: Residuals of the raw data with the subtracted fit.

It is important to carefully inspect the reflectivity curve for the lowest pump power 8 μJ, shown in Fig. 4.16 to contrast behavior displayed by the 40 μJ reflectivity curve. Following time-zero, the intensity of the peak intensity is decreased compared to the 40 μJ pump curve by over two-thirds. Most important is the reduction of the rise time, where electron rise time reduces from 100 ps to 25 ps. From the exponential fits, this corresponds with the decreasing trend of the fast exponential amplitude and the increase of the τ_2 lifetime (35 ps to 94 ps). For all four pump powers, the long lifetime τ_3 remained constant. Taking the Fourier transform of the residuals, Figure 4.17(a), we notice the same 46 GHz frequency seen in the 40 μJ pump power case, but the low frequency has shifted form 3.6 GHz to 1.8 GHz. Additionally, the magnitudes of higher frequency oscillation is decreased compared to the lower frequency oscillation. By fitting the residuals the high frequency oscillation is 46.24 $\pm$ 0.08 GHz with a damping time of 390 $\pm$ 80 ps and the low frequency oscillation is 1.88 $\pm$ 0.04 GHz with a damping time of 2000 $\pm$ 1000 ps. For the 8 μJ reflectivity curve, the time length of the scan was double compared to the 40 μJ pump

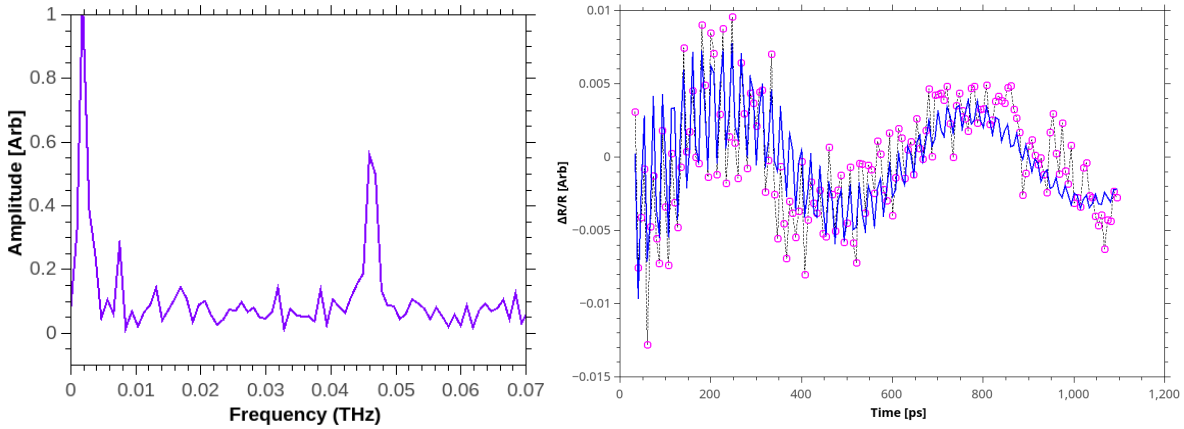

(a) (b)

Figure 4.17: (a) Fourier transforms for the residuals for both the 8 μJ pump power fit. High amplitude frequencies are visible around 46 GHz and 1.8 GHz. (a) Two damping sinusoidal fit for the 8 μJ residuals using the frequencies extracted from the Fourier transform.

power scan granting better statistics for the low frequency oscillation, although longer time scans to 2-3 ns are required to capture more periods.

Correlations between the oscillation frequency and amplitude as a function of pump power are examined in Figure 4.18(a)&(b). From Figure 4.18(a) the fast oscillation frequency does not change when changing the pump power within the uncertainty of the fit. On the other hand, the slow oscillation doubles in frequency, from 1.8 GHz at 8 μJ to

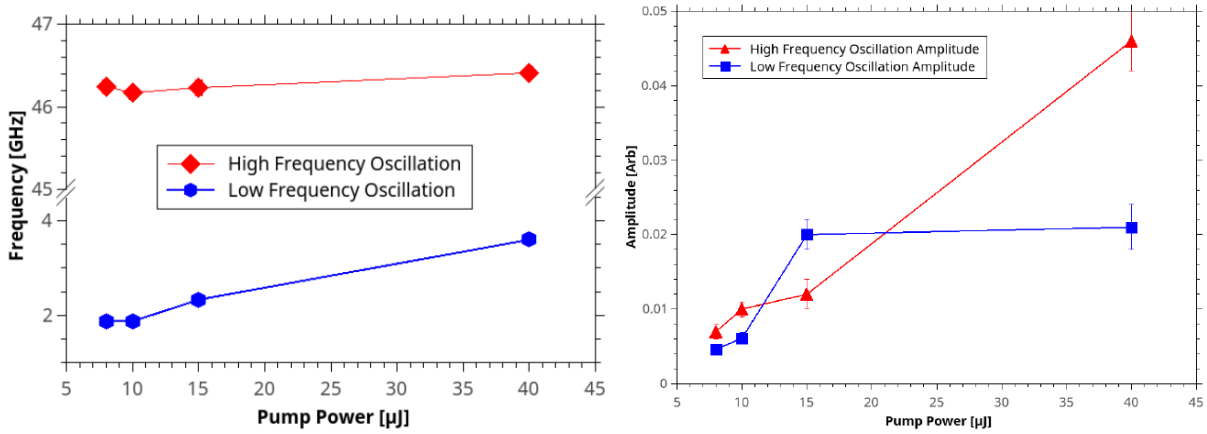

(a) (b)

Figure 4.18: (a) Power dependence of the high frequency and low frequency oscillations. Fourier transforms for the residuals for both the (b) Frequency amplitude of the high frequency and low frequency oscillations.

3.6 GHz at 40 μJ. Both oscillation amplitudes decrease with pump power. Looking at the power dependencies, we can infer possible origins of each oscillation. The most likely candidate for the high frequency oscillation is the generation of a longitudinal acoustic phonon as described by the processes in Section 4.4. Using Eq. 4.4, we can convert each frequency to a sound velocity with the index of refraction for STO as $n_{STO} = 2.35$ [95] and LSMO as $n_{LSMO} = 2.06$ [86]. The value for LSMO is only an estimate because the multiple regions in LSMO will surely have different indexes. We estimate the sound velocities of STO as $\mathrm{Vs}_{STO} = 7829$ m/s and LSMO as $\mathrm{Vs}_{LSMO} = 8900$ m/s. For STO, the value is in agreement with previous reported values from Ren and Zhang [86, 96]. Our sound velocity for LSMO is much faster than the reported value of 6500 m/s by Ren et al [86]. Even though the data agrees with the sound velocity for STO, we can not rule out the origin of the frequency as generated by LSMO. To identify if the heterostructure region responsible for the acoustic phonon, we need to measure the dispersion with additional probe energies. Repeating the calculation for the low frequency oscillation using sound velocities using both n_{STO} and n_{LSMO} yields sound velocities in the ranges of 350 - 700 m/s. By comparison of known sound velocities, this is on par with air (330 m/s), which is unphysical for a metallic system.

The low frequency oscillation, by the best of our knowledge, has not been reported in the literature for LSMO heterostructures. Based on the following arguments, we are reasonably certain that the origin is not from acoustic phonon generation:

1. The calculated sound velocity is unphysical for a metallic system.

2. The frequency exhibits a pump power dependence. In Equations 4.4 and 4.5, the only optical input capable of changing the acoustic phonon frequency is the probe energy, not the intensity.

3. The low frequency oscillations begin only after completion of the rise time, meaning it is sensitive to the electronic temperature. By contrast, the presumed high frequency acoustic phonon appears immediately after time-zero, regardless of the rise time.

We can however speculate several mechanisms to explain the low frequency oscillation as well as experimental methods for verification. One possible explanation is the long-range structural modulation of the probe pulse due to interference between the two distinct tilt regions in LSMO. This film, unlike films in the literature, is unique such that tilt and non-tilt structures coexist within the same film previously discussed in Figure 4.5. Interactions or interference of the strain pulse traveling through the tilt regions (with different indexes of refraction) may be the cause for the unexpected measured frequency. Varying the LSMO thickness and growth conditions will result in different oscillation frequencies, especially for small number of LSMO unit cells which interrupt the oxygen octahedral tilt region.

A second mechanism for dynamics on this timescale is magnetic domain wall formation caused by the cooling of the magnetic and recreating of magnetic ordering, melted by the laser pulse. Recent studies on domain wall formation in Co/Pt structures report velocities of 530 m/s in the range of the velocity for the low frequency oscillation [97]. Under the model of annihilation and recreation of magnetic domains, a power dependence of the peak electron temperature and cooling processes are expected and in agreement with the reported oscillation. Spin dynamics are commonly manipulated via the pump polarization by changing the orbital occupancy of the excited electrons, so if spin dynamics are the cause for the low frequency oscillation, a circularly polarized pump will change the reflected signal. Additionally, photoinduced oscillations can not only arise from lattice vibrations discussed previously, but also mechanisms such as orbital waves [98] and polarons [96], which are further methods of investigation for our LSMO/STO heterostructures.

4.6 Conclusion For Ultrafast Reflectivity and Preliminary Work

In conclusion, time-resolved ultrafast reflectivity was used to observe carrier and lattice dynamics in $La_{0.67}Sr_{0.33}MnO_3/SrTiO_3$ thin film heterostructures. Power dependent studies show an enhancement of electronic rise time with increasing pump power, as well as increases in phonon dephasing lifetimes. Two oscillatory modulations to the exponential decay are reported. The fast frequency at 46 GHz is pump power independent and

attributed to acoustic phonon generation of either the LSMO or STO. The low frequency oscillation has a pump power dependence, varying in frequency from 1.8 GHz (8μJ pump) to 3.6 GHz (40μJ pump). The low frequency oscillation is anomalous and can not be explained by the coherent acoustic phonon model. Additional thickness dependent, pump polarized dependent, and oxygen pressure dependent studies are needed to conclude the long frequency phonon origin.

4.6.1 Preliminary Second Harmonic Generation Studies of LSMO/STO Interfaces

Alongside bulk reflectivity measurements, we are using RASHG to study the electronic symmetry at the interface of 40 mTorr grown LSMO/STO (001) heterostructures presented in Section 4.2. Preliminary results indicate an anomalous electronic symmetry at the interfaces of LSMO/STO heterostructures which are different than the expected C_{4v} electronic symmetry of the $SrTiO_3$ substrate. RASHG experiments were conducted at room temperature in atmosphere using the experimental setup described in Sec. 2.1. The fundamental beam has an incident angle of 45° and a power of 10 μJ per pulse.

The polar plots generated by RASHG for the $SrTiO_3$ (001) substrate are shown in Figure 4.19. All three plots show isotropic behavior with respect to the crystal azimuthal orientation. PP has the largest intensity by a factor of four compared SP and 10 compared to PS. The bulk structure STO is cubic (centrosymmetric) with a surface electronic symmetry of C_{4v}. From symmetry tensor analysis for a C_{4v} point group, the fit equations for PP, PS, and PP are given in Eq 4.9.

$$I_{PP} = |a_1|^2 \qquad I_{SP} = |a_2|^2 \qquad I_{PS} = I_{SS} = 0 \tag{4.9}$$

From Eq. 4.9 all the terms are constants with no θ dependence, in agreement with the RASHG data. Our results are also in agreement with previous studies of STO (001) reported by RuiQiang et al in Reference [99].

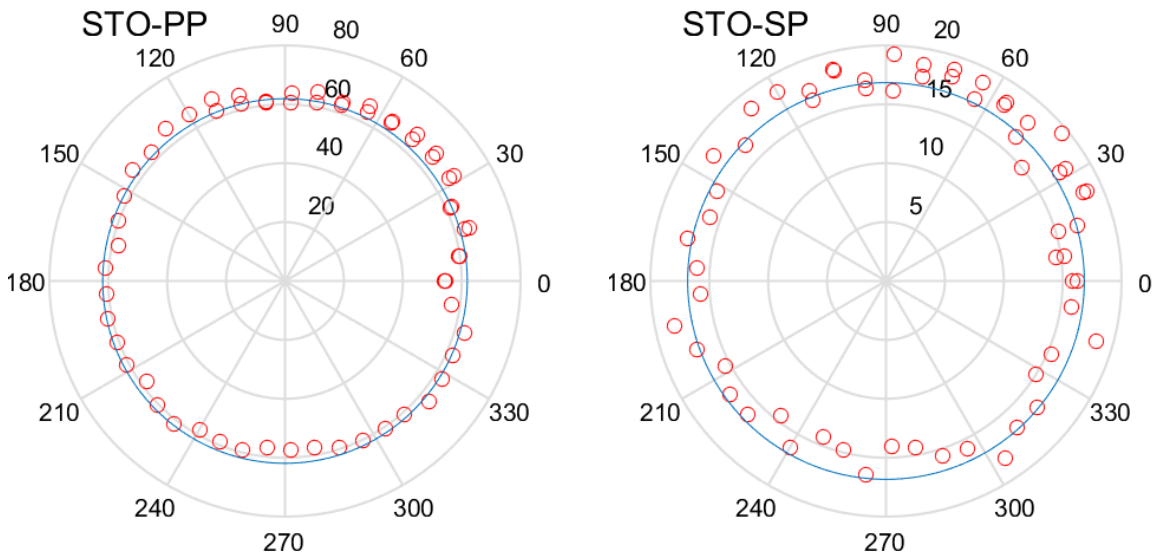

(a)

(b)

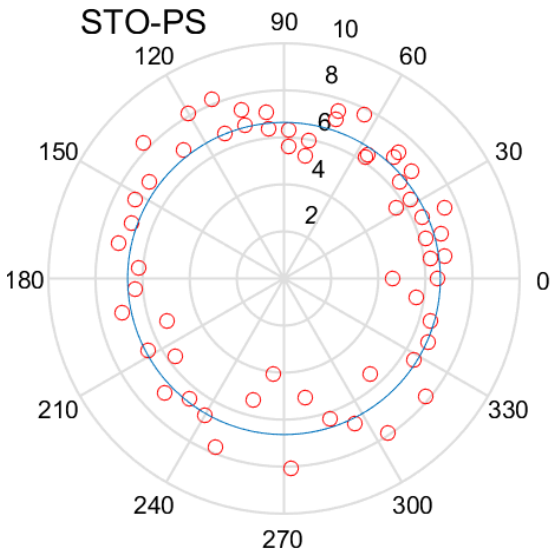

(c)

Figure 4.19: Polar plots for $SrTiO_3$ under different polarization geometries. Raw data are open red circles and blue line is an isotropic fit. (a) P-input P-output (b) S-input P-output (c) P-input S-output.

Next, the we used RAHSG to look at the electronic symmetry for the same 40 mTorr samples used in reflectivity. Both PP and PS show four-fold behavior with an isotropic offset. The angle difference in maximum intensity of large lobes in PP and PS is roughly 45°, and the maximum intensity of PP is almost 5 times larger than PS. To the best of our knowledge there are no second order surface point group symmetries which can produce the four-fold patterns seen in both polarization sets.

To explain the origin of the four-fold response, we have explored a few mechanisms. First we conducted systematic heating of the LSMO while monitoring the second harmonic during rotation to check for inclusion of a magnetic susceptibility tensor elements Eq. 1.15. However, heating LSMO did not affect the symmetry. Next, we tried to isolate the origin of the symmetry as either the surface or interface by growing thick samples (>220 uc) and capping with amorphous gold. In both cases, the four-fold symmetry remain unchanged, indicating the electronic symmetry is indeed from the LSMO/STO interface. Additionally, changing the surface of LSMO rules out the possibility of a contaminated surface gener-

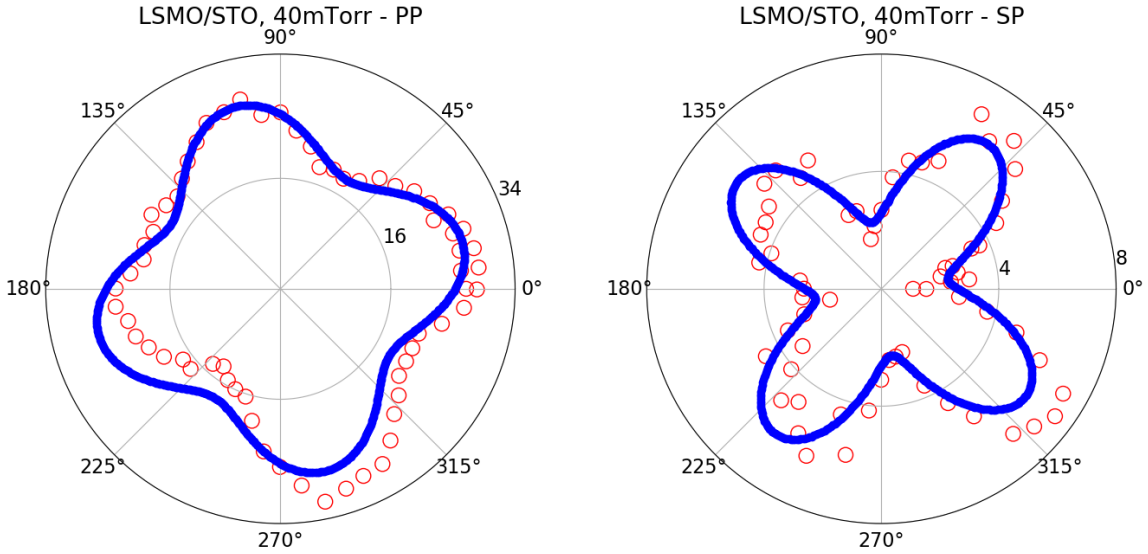

(a) (b)

Figure 4.20: Polar plots for $La_{0.67}Sr_{0.33}MnO_3/SrTiO_3$ grown at 40 mTorr under different polarization geometries. Raw data are open red circles and blue line is a four-fold fit. (a) P-input P-output polarization geometry (b) S-input P-output polarization geometry

ating the signal. Furthermore, RASHG for both 40 mTorr and 80 mTorr produce similar four-fold patterns. These preliminary results demonstrate the importance of coupling interface specific electronic measurements with the microscopic structure measurements such as STEM in order to better characterize properties near the interface of heterostructures. Currently, we are working to finalize RASHG measurements for materials across the phase diagram in Figure 4.6, to see if any electronic symmetry changes are directly related to the material processing.

Chapter 5
Metal-Insulator Transition in $(Bi_{1-x}Sb_x)_2Se_3$ Probed by Rotational Anisotropy Second Harmonic Generation

5.1 Introduction to Topological Materials

The realization of topological behavior in three-dimensional materials has captivated the scientific community beginning with the discovery of the quantum Hall effect (QHE) in the 1980s[1] [100]. In the mid 2000s, the quantum Hall effect model was extended to describe a system with a spin-momentum locked phase protected by time reversal symmetry [101, 102]. Unlike QHE, the quantum spin Hall effect does not require an external magnetic field, but it does require the strong spin orbit coupling strength produced by heavier atomic elements. The first experimental observation of the quantum spin Hall effect was successfully done by Berneig and Conig in HgTe/CdTe quantum wells [103]. Around the same time Fu, Kane, and Mele laid out the theoretical groundwork for the modern topological insulators [104]. $Bi_{1-x}Sb_3$ was the first experimental proof of a topological insulator paving the path to the modern experimental field.

Topological insulators are characterized by a topological surface state with spin currents of opposite chirality, illustrated by the simple representation in Figure 5.1 [105]. Edge

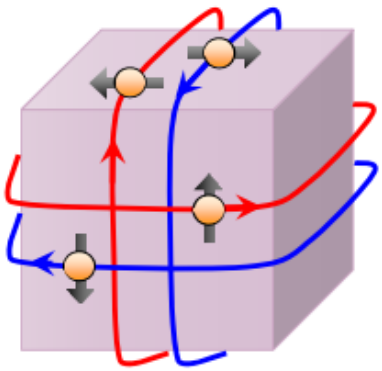

Figure 5.1: Generalized concept of opposite two-dimensional spin currents on the surface of a three-dimensional bulk insulator. Figure adapted from [105]

[1]David Thoules, Duncan Haldane, and Michael Kosterlitz were jointly awarded the Nobel prize in Physics in 2016 "for theoretical discoveries of topological phase transitions and topological phases of matter".

state currents are immune to impurities and backscattering and protected by time reversal symmetry. If the system is inversion symmetric, strong spin orbit coupling ($\mathbf{L} \cdot \mathbf{S}$) inverts the conduction and valence band, creating a time-reversal protected topological surface state. A signature of Bloch electrons traveling around the Fermi surface is a π Berry phase, leading to a half integer quantum spin Hall effect. Conducting surface currents give rise to many applications through manipulation of spin currents while retaining bulk insulating characteristics. Topological insulators are therefore major interests in spintronics and quantum computing.

5.1.1 Bi_2Se_3

Bi_2Se_3 has a layered rhombohedral crystal structure ($R\bar{3}m$ space group), consisting of 5 atoms per unit cell (Se1-Bi1-Se2-Bi1'-Se1') arranged in layers illustrated in Figure 5.2(a). Atoms form one layer which stack sequentially along the c-axis creating a set a quintuple layers. Within each quintuple layer strong covalent bonding couples atomic layers, however van Der Waals bonds between Se1 and Se1' layers holds together quintuple layers. As a result of the quintuple layer bonding, Bi_2Se_3 cleaves easily along the $a - b$ (001) plane. The unit cell is centrosymmetric about the Se2 layer, which allows the rhombohedral bulk structure to possess a trigonal C_{3v} symmetry at the surface. The top-down projection of the surface symmetry is demonstrated in Figure 5.2(b). The A site is created by the Se1 and Bi1' layers, B site by the Bi1 and Se1' layers, and C site by the Se2 layers. The C_{3v} surface symmetry is demonstrated by Xia et al. using low energy electron diffraction, shown in Figure 5.2(c) [106]. The high symmetry direction $\bar{\Gamma}$-$\bar{K}$ aligns with the zone center to A sites while the $\bar{\Gamma}$-$\bar{M}$ direction aligns with zone venter to B and C sites.

Bi_2Se_3 is arguably the most famous topological insulator boasting room temperature topological behavior. Compared to other popular candidates such as Bi_2Te_3 and $Bi_{1-x}Sb_x$, Bi_2Se_3 has the largest band gap (0.3 eV) resulting in a nearly perfect single Dirac cone in the center of the bandgap represented by the schematic in Figure 5.3(b). The Brillouin zone and surface projection are shown in Figure 5.3(a). An example of the Dirac cone is seen

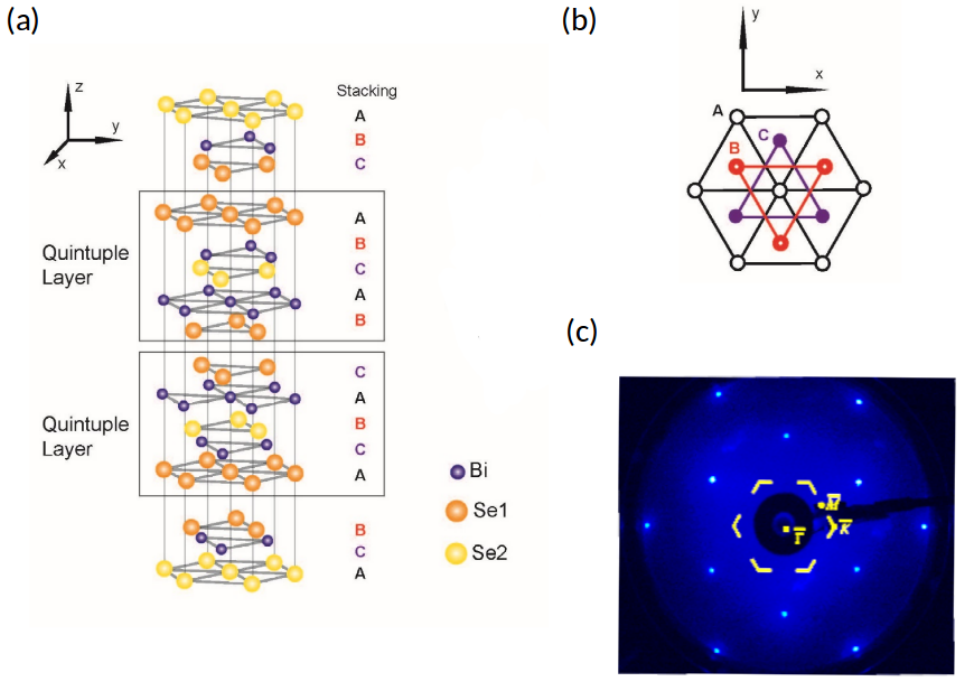

Figure 5.2: (a)Rhombohedral crystal structure of Bi_2Se_3 with stacked quintuple layers denoted by the black squares. Quintuple layered structure consisting of Se1-Bi1-Se2-Bi1'-Se1' layers (b) Top down view (looking down z-axis) of the Bi_2Se_3 surface C_{3v} surface. Layers contributing to A, B and C sites are labeled in (a). (c) Low energy electron diffraction of Bi_2Se_3 at room temperature. First Brillouin zone and surface high symmetry points are labeled in yellow. Figures adapted from Ref. [106]

in Figure 5.3(c), where Jia et al have used angle-resolved photoemission spectroscopy to measure the band structure along the $\bar{M}$-$\bar{\Gamma}$-$\bar{M}$ cross section. The bulk conduction band and linear surface Dirac bands join to form a Dirac point with a binding energy of 0.3 eV located in the zone center. Bi_2Se_3's electronic behavior is dominated by the $5p$ orbitals near the Fermi energy and has a very large spin orbit coupling strength λ_0 ($H = \lambda_0 \mathbf{L}\cdot\mathbf{S}$), $\lambda_0 = 1.3$ eV [107]. The topological surface state has been shown to be very robust, allowing coexistence with a surface superconducting gap [108] and two-dimensional electron gas [109].

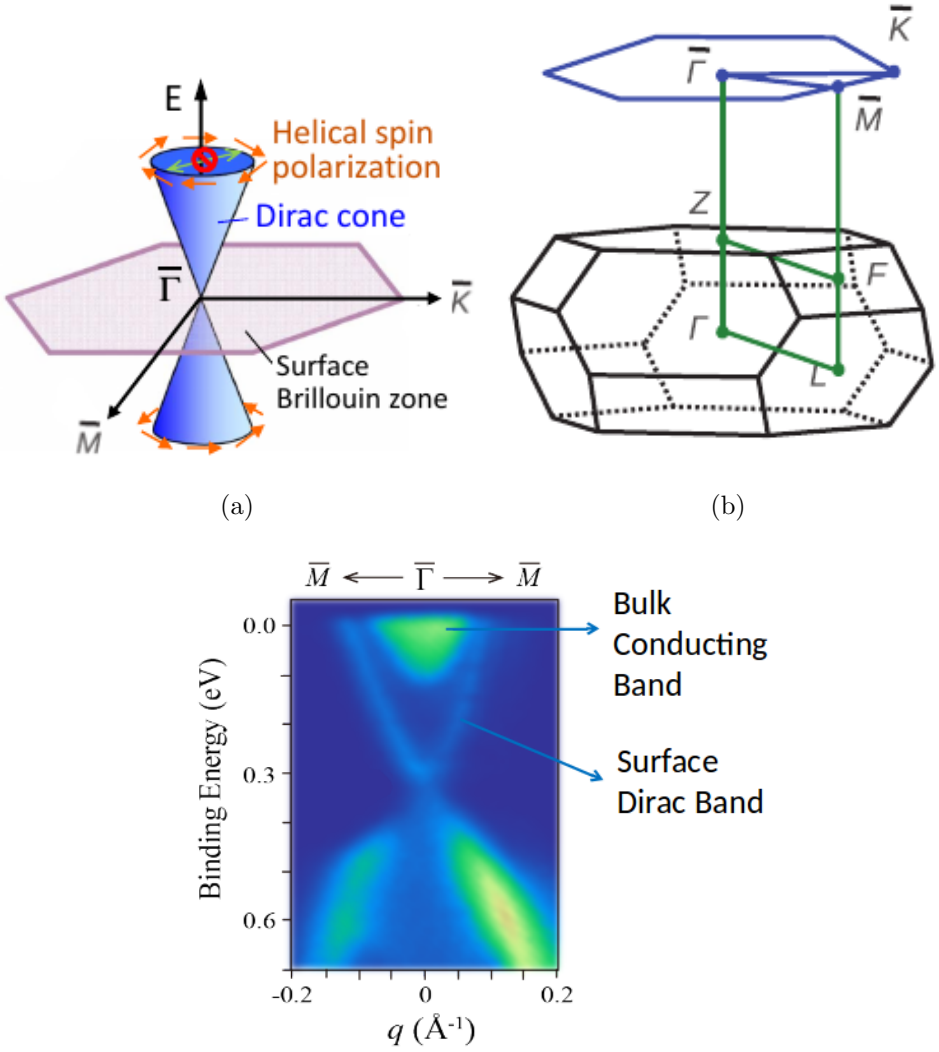

Figure 5.3: (a) Two dimensional Dirac cone located at zone center of the surface Brillouin zone. Electrons travel around the edges with opposing spin polarization [105]. (b) Bi_2Se_3 Brillouin zone for a R$\bar{3}$m space group. High symmetry k space points are Γ, Z, F, and L. Blue hexagon is the two-dimensional surface projection with high symmetry points $\bar{\Gamma}$, $\bar{M}$, and $\bar{K}$ [110]. (c) Bi_2Se_3 band structure in the $\bar{M}$ - $\bar{\Gamma}$ - $\bar{M}$ plane with a Dirac point ~0.3 eV [106].

5.2 Antimony Doping Dependence in $(Bi_{1-x}Sb_x)_2Se_3$ Compounds

Sb_2Se_3 is a trivial insulator (i.e. band insulator without a Dirac cone), known for its spin-polarized conducting surface states [111]. In the bulk, Sb_2Se_3's crystal structure is comprised of a network of chain-like Sb-Se bonds along the c-a plane. Together, these chains

create a crystal with centrosymmetric orthorhombic symmetry (Pbnm) and D_{2h} space group (Figure 5.4(a)) [112]. The (001) surface of Sb_2Se_3 has been measured with both scanning tunneling microscopy and low energy electron diffraction (Figures 5.4(c)&(d)), showing stark contrasts to the surface measured in Bi_2Se_3 [113]. Atomic-resolved STM indicates Sb_2Se_3 has a well-ordered surface, with white and black arrows elucidating surface defects caused by antimony (white arrow) and Se-vacancies (black arrow). LEED patterns show a rectangular surface lattice structure with rows of diffraction spots along the $q_{\|}$ direction.

There is much debate over the electronic structure of Sb_2Se_3, but the band gap is estimated band gap at 1.3 - 1.7 eV for single crystals [114]. Electronically, Sb_2Se_3 is very similar to Bi_2Se_3 with 3 p orbitals near the Fermi energy. Antimony is found in the same column of the periodic table as Bi, except it is one row prior. Reduction in the atomic number reduces the spin orbit coupling strength to $\lambda_0 = 0.4$ eV and as a result, Sb_2Se_3 does not have the spin orbit strength to invert the conduction band minimum and valence band maximum at the Γ point, which is necessary to produce topological behavior.

It is no surprise that the combination of two structurally and electronically dissimilar systems such as Sb_2Se_3 and Bi_2Se_3 produce an exotic phase diagram when combined. By doping antimony into $(Bi_{1-x}Sb_x)_2Se_3$, a metal-insulator transition as well as a topological phase transition has been observed. Isoelectronic Sb doping effectively tunes the Fermi energy across the bandgap from the conduction band minimum to the valence band maximum. As a result, the topological phase transition can be understood in the framework of spin orbit tuning [110]. In addition to the topological crossover, the two surface structures presented by electron diffraction in Figures 5.2(c) and 5.4(d) suggest a surface symmetry change will occur when doping.

The phase transition has been studied extensively both theoretically and experimentally for thin films and single crystals, but often times yield very conflicting results. Density functional theory calculations performed by Liu and Vanderbilt with the PBE generalized gradient approximation (GGA) while taking into account electron exchange correlations

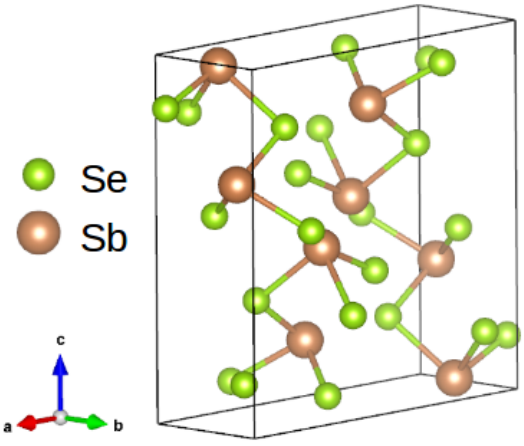

(a)

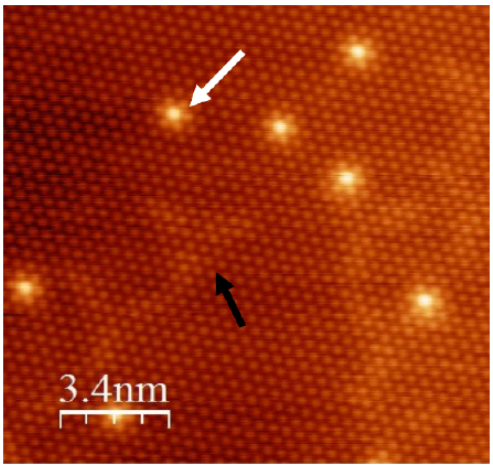

(b)

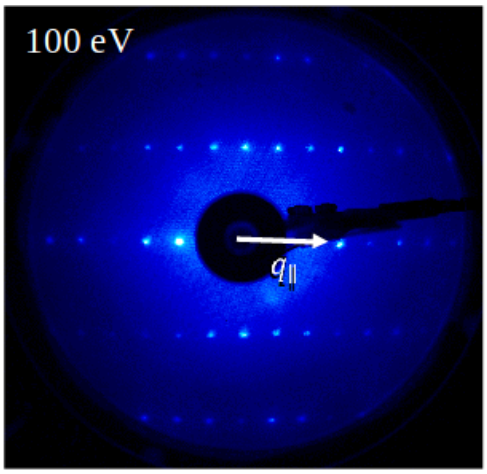

(c)

Figure 5.4: (a) Bulk orthorhombic (Pbnm) crystal structure of Sb_2Se_3. (b) Atomic-resolved scanning tunneling microscopy image the Sb_2Se_3 surface. White and black arrows elucidate defects caused by antimony and selenium vacancies respectively [106] (c) Low energy electron diffraction of Sb_2Se_3 showing a rectangular lattice with diffraction spots along the $q_{\|}$ direction. [113]

[110]. Calculations of the density of states for $(Bi_{1-x}Sb_x)_2Se_3$ produce homogeneous hybridization of the Bi $6p$, Sb $5p$, and Se p orbitals around the Fermi energy. Because of the homogeneity, their disorder/impurity substitution model predicts a linear band gap decrease with increasing doping concentration x. Trivializing the topological phase transition only to the spin orbit coupling strength is consistent with the large scale study of both topological and trivial insulators by Zhang et al [107]. Liu and Vanderbilt's results in Figure 5.5 predict at a critical doping of $x = 65\%$ the Brillouin zone center band gap undergoes a crossover transition from a topological insulator (positive $\Delta\Gamma$ (eV)) to trivial insulator (negative $\Delta\Gamma$ (eV)). Follow up density functional calculations by Abdalla et al in 2015 also use PBE-GGA functionals and predict linear band gap evolution with changes in doping [115]. However, Abdalla predicts a very different crossover concentration at $x = 0.4$ showing theoretically there is no clear consensus explaining the topological transition. In both first-principle calculations, Liu and Abdalla assume Sb_2Se_3 to have a rhombohedral symmetry and a fully relaxed structure.

To solve the discrepancy between theoretical predictions, Devidas et al conducted magneto-transport measurements on synthesized $(Bi_{1-x}Sb_x)_2Se_3$ single crystals to determine the Landau level diagram and the effects of selenium vacancies [116]. Shubnikov de-Haas (SdH) oscillations were observed at low temperatures (4.2 K) for in-plane (H$\|$ab)

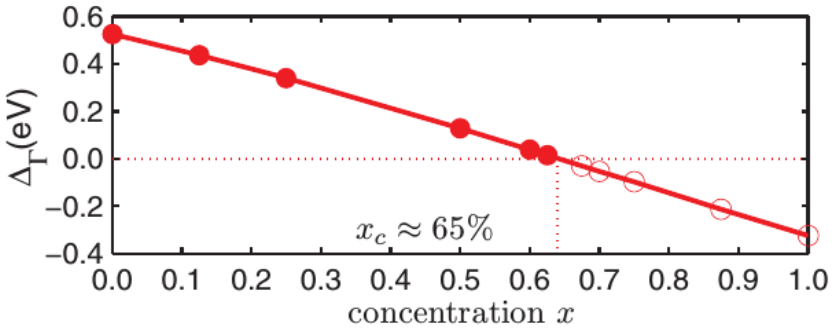

Figure 5.5: First principle calculations by Liu and Vanderbilt for the bandgap, $\Delta\Gamma$, as a function of impurity doping x in $(Bi_{1-x}Sb_x)_2Se_3$ compounds. $x = 65\%$ indicates a transition from topological insulator to non-topological insulator. Figure adapted from [110]

and out-of-plane (H||c) field configurations. Throughout doping percentages of 0% to 50%, Sdh oscillations were present in the H||c configuration, but only emerged in the H||ab configuration after 50%, where a three-dimensional Fermi surface emerges. After extracting the concentration dependent oscillation frequencies in Figure 5.6(a), Landau level fan diagram analysis was used to determine the Berry phase shown in Figure 5.6(b). For a topological surface state, the Landau level intercept should be 0.5, corresponding to a π Berry phase. At the critical concentration of $x = 0.3$, the intercept deviates far from the ideal Berry phase value, which is only possible if there is a topological crossover.

In $(Bi_{1-x}Sb_x)_2Se_3$ thin films there is a similar story. Lee et al conclude the metal-insulator transition is at $x = 20\%$ by using Raman spectroscopy to track phase transition emergent Sb-Sb and Sb-Se vibrational modes [117]. Zhang et al use magneto-transport to pin both the metal-insulator and topological transition at $x = 30\%$ [118]. Liu characterizes molecular beam epitaxy grown films using angle-resolved photoemission spectroscopy (ARPES) up to $x = 50\%$. At 50%, mixed orthorhombic and rhombohedral phases are present in the x-ray diffraction, but ARPES still detects the topological surface states [119]. Satake et al grow $(Bi_{1-x}Sb_x)_2Se_3$ alloyed films on a Bi_2Se_3 buffer layer with a InP(111) sub-

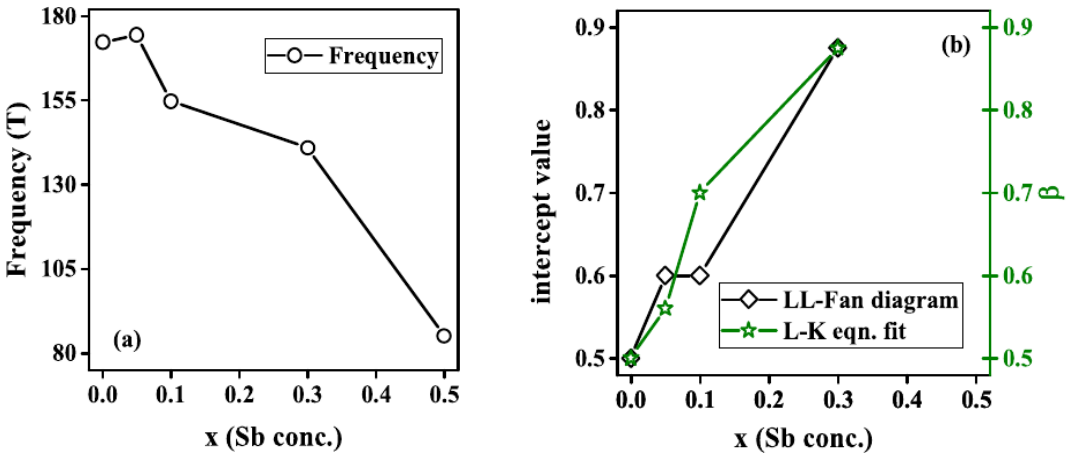

(a) (b)

Figure 5.6: (a) Shubnikov de-Haas oscillation frequency as a function of chemical doping. (b) Landau level fan diagram analysis the SdH oscillation frequencies. Intercept of 0.5 indicates a π Berry phase. Figures adapted from [116]

strate up to a Sb concentration of $x = 80\%$, while retaining topological non-trivial behavior up to $x = 070\%$ [120].

From all the theoretical and experimental studies demonstrated above, it is evident that there is still much unknown regarding the interplay between the topological phase transition and the metal-insulator transition in $(Bi_{1-x}Sb_x)_2Se_3$ alloyed compounds. From the literature, no one has conducted a controlled surface study looking only at the electronic response. Using RASHG, we directly probe the surface electronic symmetry as a function of antimony doping to monitor consequent surface evolution.

5.3 RASHG Experiment and Results

Rotational anisotropy second harmonic generation measurements been conducted for $(Bi_{1-x}Sb_x)_2Se_3$ for the following chemical compositions: $Bi_{0.1.97}Sb_{0.03}Se_3$, $Bi_{1.4}Sb_{0.6}Se_3$, and $Bi_1Sb_{0.8}Se_3$. On $x = 3\%$ an d $x = 60\%$ samples, energy dispersive x-ray spectroscopy (EDAX) and electron microprobe measurements were done using samples from the same growth batch to confirm the single crystal chemical composition, while only EDAX was conducted on $x = 80\%$. The deviation from the nominal concentration value at $x = 80\%$, is due to the large error from the EDAX measurement. Electron microprobe measurements are needed for $x = 80\%$ to confirm the concentration values. To check the structure of our compounds, LEED and x-ray diffraction measurements to identify the surface and bulk symmetry and check for mixed phases are being conducted. These compounds represent doping concentrations near the parent compound, just before the topological phase transition, and after the predicted topological crossover based on Liu's calculation [110]. The experimental setup for RASHG is identical to the measurements for the $IrTe_2$ in the high temperature phase and the LSMO/STO thin films. A laser power of 10 μJ per pulse was used for the fundamental beam. For consistency, the same experimental conditions (laser power, incident angle, polarization angles) were used for each polarization and doping percentage.

RASHG plots for antimony doping of $x = 3\%$ is shown in Figure Fig. 5.7(a)&(b). Green points correspond to the raw experimental data and the purple lines are the theoretical fits for a C_{3v} surface symmetry modified by an additional isotropic term. We believe the isotropic signal is a result of too much incident power which is close, but still below, the damage threshold of the sample. We are working on extending our sensitivity to move to lower powers. Derivations of the fit equations can be found in Appendix A. For all polarization combinations and doping concentrations, second harmonic intensities are normalized to the maximum intensity from PS at $x = 3\%$. For the P_{input}-P_{output} geometry, a three-fold intensity is present with large intensity lobes at 0°, 120°, and 240° and small lobes at 60°, 180°, and 300°. Similarly, P_{input}-S_{output} geometry has a six-fold pattern with maximums every 60° starting around 40°. PP fit well to the expected three-fold with nonlinear susceptibility fit coefficients of $a^{(1)} = 0.12$ and $a^{(2)} = 0.59$. PS was also fit the theoretical six-fold pattern and nonlinear susceptibility fit coefficient ofs $a^{(1)} = 0.12$ and $a^{(2)} = 0.56$ were extracted. We conclude that our low concentration doping plots yield the same symmetry as the parent compound reported by Hsieh et al [121].

Next we conduct the same measurement on a compound with an antimony doping of $x = 60\%$, plots are in Figure 5.8(a)&(b). In the P_{input}-S_{output} geometry, we see no change in the electronic symmetry. From the six-fold fit, we also get the same susceptibility fit coefficient $a^{(2)} = 0.55$ meaning there is no electronic deviation from rhombohedral symmetry and no surface reconstruction has occurred. There is however, a slight variation in the electronic symmetry in the P_{input}-P_{output} geometry occurring as an increase in the small lobe intensity relative to the large lobe intensity. This change is reflected in the PP fit coefficients where $a^{(1)}$ decreased to 0.07 and $a^{(2)}$ increased to 0.64.

RASHG for the highest antimony concentration $x = 80\%$ shows a striking change in electronic symmetry compared to $x = 3\%$ and $x = 60\%$ (Figure 5.9). Deviations from the three-fold PP polarization more resembles a near six-fold with small intensity lobes almost equal to the large intensity lobes. Fitting to a three-fold produces coefficients of

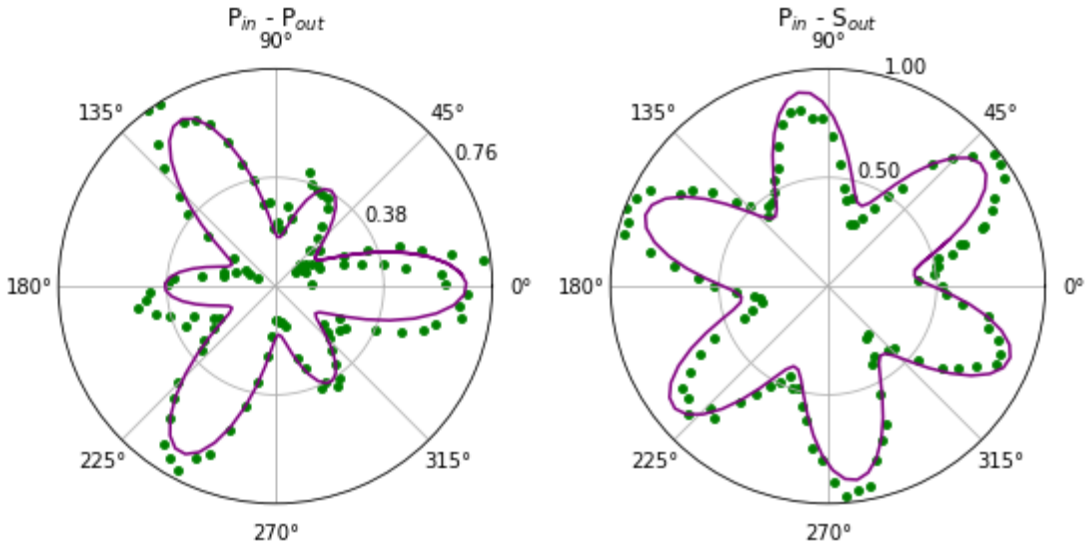

(a) (b)

Figure 5.7: Polar plots for $Bi_{1.97}Sb_{0.03}Se_3$. Green points are the raw SHG and the purple lines are the theoretical fits (a) P_{in}-P_{out} polarization geometry. (b) P_{in}-S_{out} polarization geometry.

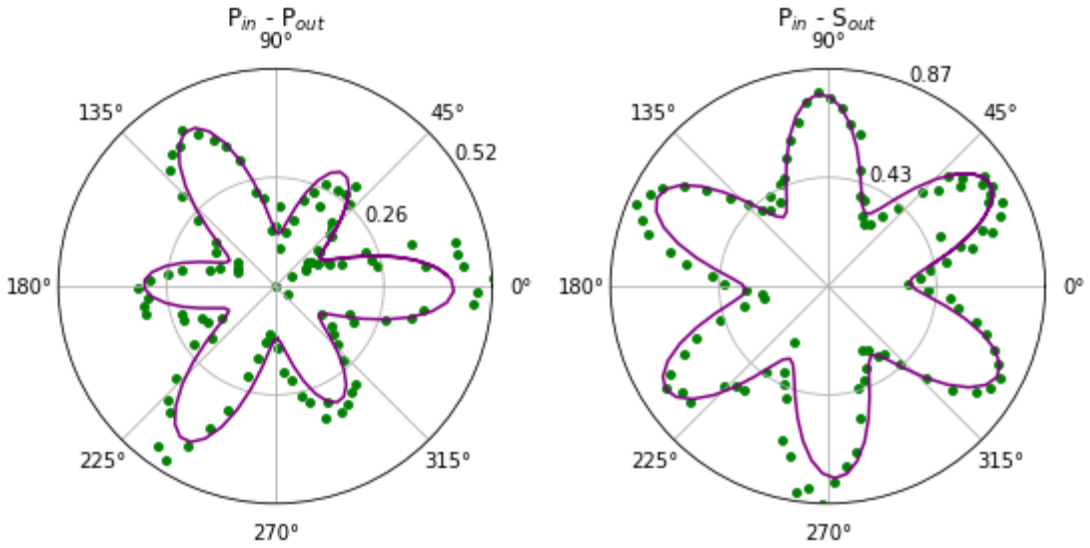

(a) (b)

Figure 5.8: Polar plots for $Bi_{1.4}Sb_{0.6}Se_3$. Green points are the raw SHG and the purple lines are the theoretical fits (a) P_{in}-P_{out} polarization geometry. (b) P_{in}-S_{out} polarization geometry.

$a^{(1)} = 0.02$ and $a^{(2)} = 0.76$. PS also shows a significant change in symmetry from six-fold

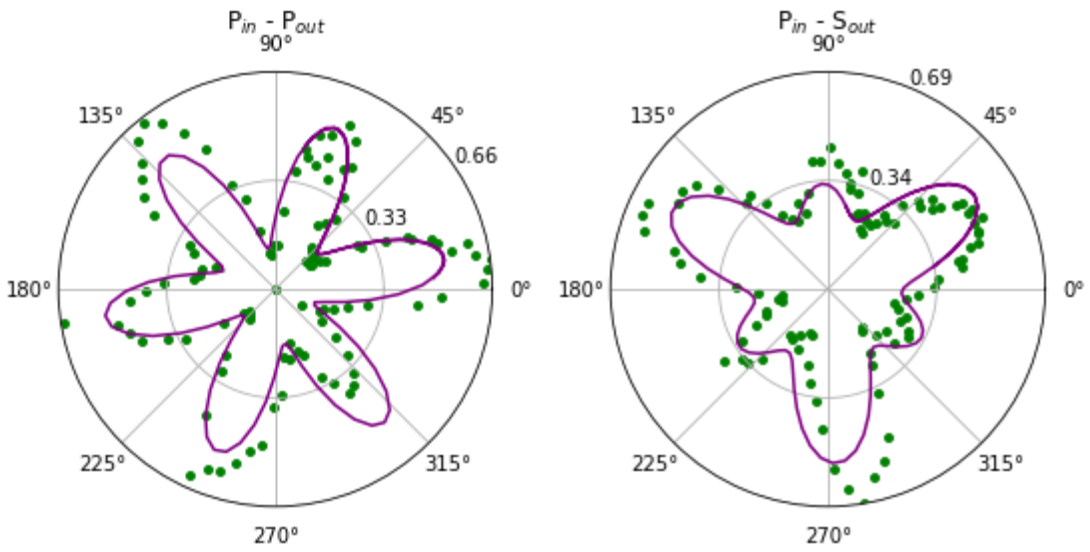

(a) (b)

Figure 5.9: Polar plots for $Bi_1Sb_{0.8}Se_3$. Green points are the raw SHG and the purple lines are the theoretical fits (a) P_{in}-P_{out} polarization geometry. (b) P_{in}-S_{out} polarization geometry.

to a three-fold symmetry. When fit with a three-fold, we extract the nonlinear coefficient $a^{(2)} = 0.65$.

Nonlinear susceptibility fit coefficients for all doping concentrations are plot in Figure 5.10, with PP in (a) and PS in (b). Based off the modeling in Appendix A, the $a^{(1)}$ coefficient originates predominately from the out-of-plane (OOP) second order susceptibility tensor elements, $a^{(1)} \propto \chi_{zzz}+\chi_{zxx}+\chi_{xxz}$, and $a^{(2)}$ originates from the in-plane (IP) tensor elements, $a^{(2)} \propto \chi_{xxx}$. Understanding the origin of the coefficients allows us to draw a few conclusions. First for PP, doping gradually increases the in-plane response, while reducing the out-of-plane-response. In PS, the IP response stays constant at low doping, while showing large increase at $x = 80\%$. At $x = 80\%$, the electronic symmetry can no longer be described by a C_{3v} surface. Second, these results would suggest a surface electronic symmetry change has occurred.

One other possible explanation for the symmetry change is the presence of mixed phases on the surface, which are smaller than the spot size of the laser ($\sim$100-150 μm). SHG does

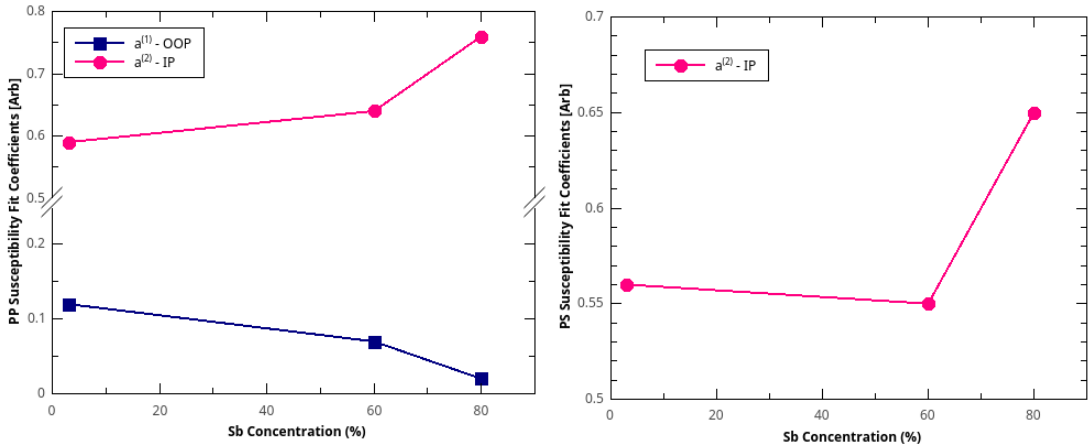

(a) (b)

Figure 5.10: Fit coefficients PP and PS fitting. $a^{(1)}$ is the out-of-plane (OOP) coefficient and $a^{(2)}$ is the in-plane (IP) coefficient (a) PP polarization geometry (b) PS polarization geometry

not have atomic resolution and can not separate signal contributions from multiple domains or phases within the spot size. LEED or STM in conjunction with SHG would be necessary to confirm this theory. Although the results presented in Figure 5.10 are compelling for an electronic symmetry change on the surface, more doping concentrations around 80% are still needed to identify symmetry trends close to the topological phase transition predicted by Liu and Vanderbilt (from 76% - 83%) and more accurately determine the abrupt nature of the IP coefficient.

5.4 Conclusion

In summary, RASHG was used to identify the electronic symmetry of $(Bi_{1-x}Sb_x)_2Se_3$ compounds at doping percentages of $x = 3\%, 60\%,$ and 80%. For low doping concentrations, 3% and 60%, the electronic symmetry closely resembles the symmetry of the parent compound reported in the literature [121]. At high doping percentage, 80%, a change in symmetry is observed evident by a six-fold change in PP and a three-fold change in PS. These observations can be explained as primarily originating from the in-plane response as an electronic symmetry change on the surface. In order to conclude the transition as topological complementary ARPES or magneto-transport measurements are needed. Ad-

ditional concentrations and corresponding surface structural measurements close to 80% are required to determine the origin of the symmetry change.

References

[1] A. L. Schawlow and C. H. Townes, Physical Review **112**, 1940 (1958).

[2] T. H. Maiman, Nature **187**, 493 (1960).

[3] P. A. Franken, A. E. Hill, C. W. Peters, and G. Weinreich, Phys. Rev. Lett. **7**, 118 (1961).

[4] J. A. Armstrong, N. Bloembergen, J. Ducuing, and P. S. Pershan, Physical Review **127**, 1918 (1962).

[5] K. C. Phillips, H. H. Gandhi, E. Mazur, and S. K. Sundaram, Advances in Optics and Photonics **7**, 684 (2015).

[6] D. Strickland and G. Mourou, Optics communications **55**, 447 (1985).

[7] J. Bardeen and W. H. Brattain, Physical Review **74**, 230 (1948).

[8] C. B. Duke, Proceedings of the National Academy of Sciences **100**, 3858 LP (2003).

[9] E. W. Plummer and R. D. Young, Physical Review B **1**, 2088 (1970).

[10] K. Siegbahn and C. Nordling, Nov. act. uppsaliensis (1967).

[11] A. Ohtomo and H. Hwang, Nature **427**, 423 (2004).

[12] N. Reyren, S. Thiel, A. Caviglia, L. F. Kourkoutis, G. Hammerl, C. Richter, C. Schneider, T. Kopp, A.-S. Rüetschi, D. Jaccard, *et al.*, Science **317**, 1196 (2007).

[13] J. Zhang and R. Averitt, Annual Review of Materials Research **44**, 19 (2014).

[14] Y.-R. Shen, New York, Wiley-Interscience, 1984, 575 p. (1984).

[15] N. Bloembergen, *Nonlinear Optics* (W. A. Benjamin, New York, 1965).

[16] R. W. Boyd, *Nonlinear Optics, Third Edition*, 3rd ed. (Academic Press, Inc., Orlando, FL, USA, 2008).

[17] V. Mizrahi and J. E. Sipe, Journal of the Optical Society of America B **5**, 660 (1988).

[18] R. Paschotta, P. Kürz, R. Henking, S. Schiller, and J. Mlynek, Optics Letters **19**, 1325 (1994).

[19] M. Nisenoff, M. Savage, R. Franken, P. D. Maker, R. W. Terhune, M. Nisenoff, and C. M. Savage, Physical Review Letters **8**, 21 (1962).

[20] M. Fejer, G. Magel, D. Jundt, and R. Byer, IEEE Journal of Quantum Electronics **28**, 2631 (2002).

[21] F. Hellman, A. Hoffmann, Y. Tserkovnyak, G. S. Beach, E. E. Fullerton, C. Leighton, A. H. MacDonald, D. C. Ralph, D. A. Arena, H. A. Dürr, *et al.*, Reviews of modern physics **89**, 025006 (2017).

[22] S. Bhagavantam and P. Pantulu, in *Proceedings of the Indian Academy of Sciences-Section A*, Vol. 66 (Springer, 1967) pp. 33–39.

[23] D. A. Kleinman, Physical Review **126**, 1977 (1962).

[24] S. Kasahara, H. Shi, K. Hashimoto, S. Tonegawa, Y. Mizukami, T. Shibauchi, K. Sugimoto, T. Fukuda, T. Terashima, A. H. Nevidomskyy, *et al.*, Nature **486**, 382 (2012).

[25] K. J. Choi, M. Biegalski, Y. Li, A. Sharan, J. Schubert, R. Uecker, P. Reiche, Y. Chen, X. Pan, V. Gopalan, *et al.*, Science **306**, 1005 (2004).

[26] K. Sato, K. Takanashi, K. Himi, A. Kirilyuk, and T. Rasing, Journal of magnetism and magnetic materials **239**, 351 (2002).

[27] H. Yamada, Y. Ogawa, Y. Ishii, H. Sato, M. Kawasaki, H. Akoh, and Y. Tokura, Science **305**, 646 (2004).

[28] Y. Fan, K. Smith, G. Lüpke, A. Hanbicki, R. Goswami, C. Li, H. Zhao, and B. Jonker, Nature nanotechnology **8**, 438 (2013).

[29] D. H. Torchinsky, H. Chu, T. Qi, G. Cao, and D. Hsieh, Review of Scientific Instruments **85**, 083102 (2014).

[30] J. Harter, L. Niu, A. Woss, and D. Hsieh, Optics letters **40**, 4671 (2015).

[31] S. Manzeli, D. Ovchinnikov, D. Pasquier, O. V. Yazyev, and A. Kis, Nature Reviews Materials **2**, 17033 (2017).

[32] R. Coleman, B. Giambattista, P. Hansma, A. Johnson, W. McNairy, and C. Slough, Advances in Physics **37**, 559 (1988).

[33] J. A. Wilson, F. Di Salvo, and S. Mahajan, Advances in Physics **24**, 117 (1975).

[34] J. E. Taylor, Z. Zhang, G. Cao, L. H. Haber, R. Jin, and E. W. Plummer, Chinese Physics Letters **35**, 097102 (2018).

[35] R. L. Withers and J. A. Wilson, Journal of Physics C: Solid State Physics **19**, 4809 (1986).

[36] A. H. Castro Neto, Physical Review Letters **86**, 4382 (2001).

[37] Y. Ma, L. Kou, X. Li, Y. Dai, S. C. Smith, and T. Heine, Physical Review B **92**, 085427 (2015).

[38] A. C. Neto, Physical Review Letters **86**, 4382 (2001).

[39] M. N. Ali, J. Xiong, S. Flynn, J. Tao, Q. D. Gibson, L. M. Schoop, T. Liang, N. Haldolaarachchige, M. Hirschberger, N. Ong, *et al.*, Nature **514**, 205 (2014).

[40] G. Moody, J. Schaibley, and X. Xu, Journal of the OpticalSociety of America B **33**, 1 (2016).

[41] K. Novoselov, D. Jiang, F. Schedin, T. Booth, V. Khotkevich, S. Morozov, and A. Geim, Proceedings of the National Academy of Sciences **102**, 10451 (2005).

[42] D. Lloyd, X. Liu, J. W. Christopher, L. Cantley, A. Wadehra, B. L. Kim, B. B. Goldberg, A. K. Swan, and J. S. Bunch, Nano Letters **16**, 5836 (2016).

[43] W. Choi, N. Choudhary, G. H. Han, J. Park, D. Akinwande, and Y. H. Lee, Materials Today **20**, 116 (2017).

[44] M. Pumera and A. H. Loo, TrAC Trends in Analytical Chemistry **61**, 49 (2014).

[45] Q. H. Wang, K. Kalantar-Zadeh, A. Kis, J. N. Coleman, and M. S. Strano, Nature nanotechnology **7**, 699 (2012).

[46] S. Pyon, K. Kudo, and M. Nohara, Journal of the Physical Society of Japan **81**, 053701 (2012).

[47] J. Yang, Y. Choi, Y. S. Oh, A. Hogan, Y. Horibe, K. Kim, B. Min, and S. Cheong, Physical Review Letters **108**, 116402 (2012).

[48] Y. Zhu and W. Zhen, Personal Communication.

[49] A. F. Fang, G. Xu, T. Dong, P. Zheng, and N. L. Wang, Scientific Reports **3**, 1153 (2013).

[50] G. L. Pascut, K. Haule, M. J. Gutmann, S. A. Barnett, A. Bombardi, S. Artyukhin, T. Birol, D. Vanderbilt, J. J. Yang, S. W. Cheong, and V. Kiryukhin, Physical Review Letters **112**, 086402 (2014).

[51] G. Cao, W. Xie, W. A. Phelan, J. DiTusa, and R. Jin, Physical Review B **95**, 035148 (2017).

[52] C. Chen, J. Kim, Y. Yang, G. Cao, R. Jin, and E. Plummer, Physical Review B **95**, 094118 (2017).

[53] P. Ehrenfest, *Phasenumwandlungen im ueblichen und erweiterten Sinn, classifiziert nach den entsprechenden Singularitaeten des thermodynamischen Potentiales* (NV Noord-Hollandsche Uitgevers Maatschappij, 1933).

[54] H. E. Stanley, *Phase transitions and critical phenomena* (Clarendon Press, Oxford, 1971).

[55] H. Cao, B. C. Chakoumakos, X. Chen, J. Yan, M. A. McGuire, H. Yang, R. Custelcean, H. Zhou, D. J. Singh, and D. Mandrus, Physical Review B **88**, 1 (2013).

[56] K.-T. Ko, H.-H. Lee, D.-H. Kim, J.-J. Yang, S.-W. Cheong, M. Eom, J. Kim, R. Gammag, K.-S. Kim, H.-S. Kim, *et al.*, Nature communications **6**, 7342 (2015).

[57] R. E. Peierls, *Quantum theory of solids* (Clarendon Press, 1996).

[58] Y. S. Oh, J. J. Yang, Y. Horibe, and S. W. Cheong, Physical Review Letters **110**, 1 (2013).

[59] B. Joseph, M. Bendele, L. Simonelli, L. Maugeri, S. Pyon, K. Kudo, M. Nohara, T. Mizokawa, and N. Saini, Physical Review B **88**, 224109 (2013).

[60] M. J. Eom, K. Kim, Y. J. Jo, J. J. Yang, E. S. Choi, B. I. Min, J. H. Park, S. W. Cheong, and J. S. Kim, Physical Review Letters **113**, 1 (2014).

[61] H. S. Kim, T.-H. Kim, J. Yang, S.-W. Cheong, and H. W. Yeom, Physical Review B **90**, 201103 (2014).

[62] T. Mauerer, M. Vogt, P. J. Hsu, G. L. Pascut, K. Haule, V. Kiryukhin, J. Yang, S. W. Cheong, W. Wu, and M. Bode, Physical Review B **94**, 1 (2016).

[63] Q. Li, W. Lin, J. Yan, X. Chen, A. G. Gianfrancesco, D. J. Singh, D. Mandrus, S. V. Kalinin, and M. Pan, Nat. Commun. **5**, 5358 (2014).

[64] J. E. Taylor, R. A. Khoury, K. Zhao, M. Saghayezhian, L. H. Haber, and E. W. Plummer, in *Frontiers in Optics / Laser Science* (Optical Society of America, 2018) p. JW3A.47.

[65] Y. Tokura, Physics Today **56**, 50 (2003).

[66] A. P. Ramirez, Journal of Physics: Condensed Matter **9**, 8171 (1997).

[67] J. Mannhart, D. H. A. Blank, H. Y. Hwang, A. J. Millis, and J.-M. Triscone, MRS Bulletin **33**, 1027 (2008).

[68] C. Alexander, G. Cao, V. Dobrosavljevic, S. McCall, J. Crow, E. Lochner, and R. Guertin, Physical Review B **60**, R8422 (1999).

[69] A. Gozar, G. Logvenov, L. F. Kourkoutis, A. T. Bollinger, L. A. Giannuzzi, D. A. Muller, and I. Bozovic, Nature **455**, 782 (2008).

[70] A. C. Turnock, H. P. Eugster, S.-W. Cheong, and M. Mostovoy, Nature Materials **6**, 13 (2007).

[71] A. Glazer, Acta Crystallographica Section B: Structural Crystallography and Crystal Chemistry **28**, 3384 (1972).

[72] J. Hemberger, A. Krimmel, T. Kurz, H.-A. K. Von Nidda, V. Y. Ivanov, A. Mukhin, A. Balbashov, and A. Loidl, Physical Review B **66**, 094410 (2002).

[73] M. Bowen, M. Bibes, A. Barthélémy, J.-P. Contour, A. Anane, Y. Lemaıtre, and A. Fert, Applied Physics Letters **82**, 233 (2003).

[74] J.-H. Park, E. Vescovo, H.-J. Kim, C. Kwon, R. Ramesh, and T. Venkatesan, Nature **392**, 794 (1998).

[75] Z. Liao, F. Li, P. Gao, L. Li, J. Guo, X. Pan, R. Jin, E. Plummer, and J. Zhang, Physical Review B **92**, 125123 (2015).

[76] H. Guo, Z. Wang, S. Dong, S. Ghosh, M. Saghayezhian, L. Chen, Y. Weng, A. Herklotz, T. Z. Ward, R. Jin, S. T. Pantelides, Y. Zhu, J. Zhang, and E. W. Plummer, Proceedings of the National Academy of Sciences , 201706814 (2017).

[77] M. Saghayezhian, *Manipulating physical properties of complex materials by processing*, Ph.D. thesis, Louisiana State University (2017).

[78] R. Schoenlein, W. Lin, J. Fujimoto, and G. Eesley, Physical Review Letters **58**, 1680 (1987).

[79] J. Hohlfeld, S.-S. Wellershoff, J. Güdde, U. Conrad, V. Jähnke, and E. Matthias, Chemical Physics **251**, 237 (2000).

[80] J. Hohlfeld, J. Müller, S.-S. Wellershoff, and E. Matthias, Applied Physics B **64**, 387 (1997).

[81] K. H. Bennemann, *Non-linear optics in metals*, 98 (Oxford University Press, 1998).

[82] L. Jiang and H.-L. Tsai, Journal of Heat Transfer **127**, 1167 (2005).

[83] S. Anisimov, B. Kapeliovich, and T. Perelman, Zh. Eksp. Teor. Fiz **66**, 375 (1974).

[84] C. Thomsen, H. T. Grahn, H. J. Maris, and J. Tauc, Physical Review B **34**, 4129 (1986).

[85] R. Côte and A. Devos, Review of Scientific Instruments **76**, 1 (2005).

[86] Y. Ren, M. Trigo, R. Merlin, V. Adyam, and Q. Li, Applied physics letters **90**, 251918 (2007).

[87] P. Ruello and V. E. Gusev, Ultrasonics **56**, 21 (2015).

[88] T. Pezeril, P. Ruello, S. Gougeon, N. Chigarev, D. Mounier, J.-M. Breteau, P. Picart, and V. Gusev, Physical Review B **75**, 174307 (2007).

[89] H. Ogi, T. Shagawa, N. Nakamura, M. Hirao, H. Odaka, and N. Kihara, Physical Review B **78**, 134204 (2008).

[90] M. Gandolfi, G. L. Celardo, F. Borgonovi, G. Ferrini, A. Avella, F. Banfi, and C. Giannetti, Physica Scripta **92**, 034004 (2017).

[91] B. Mansart, D. Boschetto, a. Sambri, R. Malaquias, F. Miletto Granozio, U. Scotti di Uccio, P. Metcalf, and M. Marsi, Journal of Modern Optics **57**, 959 (2010).

[92] M. Quijada, J. Černe, J. Simpson, H. Drew, K. Ahn, A. Millis, R. Shreekala, R. Ramesh, M. Rajeswari, and T. Venkatesan, Physical Review B **58**, 16093 (1998).

[93] L. Peng, C. Cai, D. H. Xu, and Y. Liu, JETP Letters **99**, 27 (2014).

[94] A. M. Lomonosov, A. Ayouch, P. Ruello, G. Vaudel, M. R. Baklanov, P. Verdonck, L. Zhao, and V. E. Gusev, ACS Nano **6**, 1410 (2012).

[95] M. Cardona, Physical Review **140**, A651 (1965).

[96] B. Liu, W. Niu, X. Ruan, C. Zhu, X. Wang, L. He, W. Liu, E. Turcu, F. Wang, R. Zhang, *et al.*, Physica Status Solidi (RRL)–Rapid Research Letters , 1800657.

[97] P. Sethi, S. Krishnia, W. L. Gan, F. N. Kholid, F. N. Tan, R. Maddu, and W. S. Lew, Scientific Reports **7**, 4964 (2017).

[98] D. Polli, M. Rini, S. Wall, R. Schoenlein, Y. Tomioka, Y. Tokura, G. Cerullo, and A. Cavalleri, Nature Materials **6**, 643 (2007).

[99] R. Zhao, K. Jin, H. Guo, H. Lu, and G. Yang, Science China Physics, Mechanics and Astronomy **56**, 2370 (2013).

[100] K. V. Klitzing, G. Dorda, and M. Pepper, Physical Review Letters **45**, 494 (1980).

[101] C. L. Kane and E. J. Mele, Physical Review Letters **95**, 1 (2005).

[102] B. A. Bernevig and S. C. Zhang, Physical Review Letters **96**, 1 (2006).

[103] B. A. Bernevig, T. L. Hughes, and S.-C. Zhang, Science **314**, 1757 (2006).

[104] L. Fu, C. L. Kane, and E. J. Mele, Physical Review Letters **98**, 106803 (2007).

[105] Y. Ando, Journal of the Physical Society of Japan **82**, 102001 (2013).

[106] X. Jia, S. Zhang, R. Sankar, F.-C. Chou, W. Wang, K. Kempa, E. Plummer, J. Zhang, X. Zhu, and J. Guo, Physical Review Letters **119**, 136805 (2017).

[107] H. Zhang, C.-X. Liu, X.-L. Qi, X. Dai, Z. Fang, and S.-C. Zhang, Nature Physics **5**, 438 (2009).

[108] M.-X. Wang, C. Liu, J.-P. Xu, F. Yang, L. Miao, M.-Y. Yao, C. L. Gao, C. Shen, X. Ma, X. Chen, Z.-A. Xu, Y. Liu, S.-c. Zhang, D. Qian, J.-F. Jia, and Q.-K. Xue, Science **336**, 52 (2012).

[109] M. Bianchi, D. Guan, S. Bao, J. Mi, B. B. Iversen, P. D. King, and P. Hofmann, Nature Communications **1**, 125 (2010).

[110] J. Liu and D. Vanderbilt, Physical Review B **88**, 224202 (2013).

[111] S. Das, A. Sirohi, G. Kumar Gupta, S. Kamboj, A. Vasdev, S. Gayen, P. Guptasarma, T. Das, and G. Sheet, Physical Review B **97**, 1 (2018).

[112] N. Tideswell, F. Kruse, and J. McCullough, Acta Crystallographica **10**, 99 (1957).

[113] X. Jia, Personal Communication.

[114] R. Vadapoo, S. Krishnan, H. Yilmaz, and C. Marin, Physica Status Solidi (B) **248**, 700 (2011).

[115] E. Padilha José, R. H. Miwa, L. B. Abdalla, A. Fazzio, and T. M. Schmidt, Journal of Physics: Condensed Matter **27**, 255501 (2015).

[116] T. R. Devidas, E. P. Amaladass, S. Sharma, A. Mani, R. Rajaraman, C. S. Sundar, and A. Bharathi, Materials Research Express **4**, 026101 (2017).

[117] C. H. Lee, R. He, Z. Wang, R. L. Qiu, A. Kumar, C. Delaney, B. Beck, T. Kidd, C. Chancey, R. M. Sankaran, *et al.*, Nanoscale **5**, 4337 (2013).

[118] C. Zhang, X. Yuan, K. Wang, Z.-G. Chen, B. Cao, W. Wang, Y. Liu, J. Zou, and F. Xiu, Advanced Materials **26**, 7110 (2014).

[119] Y. Liu, C. Chong, W. Chen, J.-A. Huang, C. Cheng, K. Tsuei, Z. Li, H. Qiu, and V. Marchenkov, Japanese Journal of Applied Physics **56**, 3 (2017).

[120] Y. Satake, J. Shiogai, D. Takane, K. Yamada, K. Fujiwara, S. Souma, T. Sato, T. Takahashi, and A. Tsukazaki, Journal of Physics: Condensed Matter **30**, 085501 (2018).

[121] D. Hsieh, J. W. McIver, D. H. Torchinsky, D. R. Gardner, Y. S. Lee, and N. Gedik, Physical Review Letters **106**, 2 (2011).

Appendix A
Symmetry Analysis of Tensor Components and Rotational Anisotropy Second Harmonic Generation Fit Equations

This Appendix details the origin of the fit equations in Sec. 3.4.

We begin by defining $\chi^{(2)}_{ijk}$, the second-order susceptibility tensor (27 elements) in the most the general form,

$$\chi^{(S)}_{ijk} = \begin{pmatrix} \begin{pmatrix} \chi_{xxx} \\ \chi_{xxy} \\ \chi_{xxz} \end{pmatrix} & \begin{pmatrix} \chi_{xyx} \\ \chi_{xyy} \\ \chi_{xyz} \end{pmatrix} & \begin{pmatrix} \chi_{xzx} \\ \chi_{xzy} \\ \chi_{xzz} \end{pmatrix} \\ \begin{pmatrix} \chi_{yxx} \\ \chi_{yxy} \\ \chi_{yxz} \end{pmatrix} & \begin{pmatrix} \chi_{yyx} \\ \chi_{yyy} \\ \chi_{yyz} \end{pmatrix} & \begin{pmatrix} \chi_{yzx} \\ \chi_{yzy} \\ \chi_{yzz} \end{pmatrix} \\ \begin{pmatrix} \chi_{zxx} \\ \chi_{zxy} \\ \chi_{zxz} \end{pmatrix} & \begin{pmatrix} \chi_{zyx} \\ \chi_{zyy} \\ \chi_{zyz} \end{pmatrix} & \begin{pmatrix} \chi_{zzx} \\ \chi_{zzy} \\ \chi_{zzz} \end{pmatrix} \end{pmatrix} \tag{A.1}$$

Due to the application of Kleinman's condition, Eq. A.1 can be rewritten as,

$$d_{im} = \begin{pmatrix} d_{11} & d_{12} & d_{13} & d_{14} & d_{15} & d_{16} \\ d_{21} & d_{22} & d_{23} & d_{24} & d_{25} & d_{26} \\ d_{31} & d_{32} & d_{33} & d_{34} & d_{35} & d_{36} \end{pmatrix} \tag{A.2}$$

$IrTe_2$ possesses a centrosymmetric crystal structure with space group is D^5_{3D} with a surface symmetry of C_{3v}. Neumann's principle reduces the 18 independent tensor elements to only four independent nonzero elements, [14, 16]

$$\chi_{xxx} = -\chi_{xyy} = -\chi_{yxy},\ \chi_{zxx} = \chi_{zyy}, \chi_{xxz} = \chi_{yyz}, \chi_{zzz}. \tag{A.3}$$

The resulting d_{im} matrix is thus,

$$d_{im} = \begin{pmatrix} d_{11} & d_{11} & 0 & 0 & d_{15} & 0 \\ 0 & 0 & 0 & d_{15} & 0 & -d_{11} \\ d_{31} & d_{31} & d_{33} & 0 & 0 & 0 \end{pmatrix} \tag{A.4}$$

In the lab, we directly measure the intensity of the second harmonic polarization, therefore, must represent $\chi^{(2)}_{abc}$ of the crystal in terms of the laser coordinates. This can be accomplished by transforming $\chi^{(2)}_{abc}$ from crystal to beam coordinates using a symmetry rotation. We define the coordinate axis for an incident electric field as x, y, z which is rotated by an azimuthal ϕ for a crystal with coordinate axes $\hat{a} = \cos\phi\ \hat{x} + \sin\phi\ \hat{y}$, $\hat{b} = -\sin\phi\ \hat{x} + \cos\phi\ \hat{y}$, $\hat{c} = \hat{z}$.

The symmetry transformation rule for third rank tensors is defined as [14]

$$X^{(2)}_{ijk} = \sum_{l,m,n} R_{il} R_{jm} R_{kn} \chi_{lmn}\ , \tag{A.5}$$

where R_{il}, R_{jm}, and R_{kn} correspond to the transformation operators for an azimuthal rotation ϕ. For azimuthal rotation about a (111) surface the rotation matrix takes the form,

$$R_{kn} = \begin{pmatrix} \cos\phi & -\sin\phi & 0 \\ \sin\phi & \cos\phi & 0 \\ 0 & 0 & 1 \end{pmatrix}. \tag{A.6}$$

In the following lines as an example, we will explicitly work out some of the new susceptibility terms and use the identities for simplification:

$$\cos(3\phi) = \cos^3\phi - 3\sin^2\phi\cos\phi \tag{A.7}$$
$$\sin(3\phi) = -\sin^3\phi + 3\cos^2\phi\sin\phi \tag{A.8}$$

$\chi^{(2)}_{xxx}$:

$$\begin{aligned} \chi^{(2)}_{xxx} &= \sum_{lmn} \chi^{(2)}_{lmn}(\hat{x}\cdot\hat{l})(\hat{x}\cdot\hat{m})(\hat{x}\cdot\hat{n}) \\ &= \chi_{aaa}(\hat{x}\cdot\hat{a})(\hat{x}\cdot\hat{a})(\hat{x}\cdot\hat{a}) + \chi_{abb}(\hat{x}\cdot\hat{a})(\hat{x}\cdot\hat{b})(\hat{x}\cdot\hat{b}) + \chi_{bba}(\hat{x}\cdot\hat{b})(\hat{x}\cdot\hat{b})(\hat{x}\cdot\hat{a}) \\ &\quad +\chi_{bab}(\hat{x}\cdot\hat{b})(\hat{x}\cdot\hat{a})(\hat{x}\cdot\hat{b}) \\ &= \chi_{aaa}\cos^3\phi - \chi_{aaa}\cos\phi\sin^2\phi - \chi_{aaa}\sin^2\phi\cos\phi - \chi_{aaa}\sin^2\phi\cos\phi \\ &= \chi_{aaa}\cos(3\phi) \end{aligned} \tag{A.9}$$

$\chi^{(2)}_{xxy}$:

$$\begin{aligned} \chi^{(2)}_{xxy} &= \sum_{lmn} \chi^{(2)}_{lmn}(\hat{x}\cdot\hat{l})(\hat{x}\cdot\hat{m})(\hat{y}\cdot\hat{n}) \\ &= \chi_{aaa}(\hat{x}\cdot\hat{a})(\hat{x}\cdot\hat{a})(\hat{y}\cdot\hat{a}) + \chi_{abb}(\hat{x}\cdot\hat{a})(\hat{x}\cdot\hat{b})(\hat{y}\cdot\hat{b}) + \chi_{bba}(\hat{x}\cdot\hat{b})(\hat{x}\cdot\hat{b})(\hat{y}\cdot\hat{a}) \\ &\quad +\chi_{bab}(\hat{x}\cdot\hat{b})(\hat{x}\cdot\hat{a})(\hat{y}\cdot\hat{b}) \\ &= -\chi_{aaa}\cos^2\phi\sin\phi - \chi_{aaa}\cos^2\phi\sin\phi + \chi_{aaa}\sin^3\phi - \chi_{aaa}\cos^2\phi\sin\phi \\ &= -\chi_{aaa}\sin(3\phi) \end{aligned} \tag{A.10}$$

$\chi^{(2)}_{xxz}$:

$$\begin{aligned} \chi^{(2)}_{xxz} &= \sum_{lmn} \chi^{(2)}_{lmn}(\hat{x}\cdot\hat{l})(\hat{x}\cdot\hat{m})(\hat{z}\cdot\hat{n}) \\ &= \chi_{aac}(\hat{x}\cdot\hat{a})(\hat{x}\cdot\hat{a})(\hat{z}\cdot\hat{c}) + \chi_{bbc}(\hat{x}\cdot\hat{b})(\hat{x}\cdot\hat{b})(\hat{z}\cdot\hat{c}) + \chi_{ccc}\cancelto{0}{(\hat{x}\cdot\hat{c})}\cancelto{0}{(\hat{x}\cdot\hat{c})}(\hat{z}\cdot\hat{c}) \\ &= \chi_{aac}\cos^2\phi + \chi_{aac}\sin^2\phi \\ &= \chi_{aac} \end{aligned} \tag{A.11}$$

$\chi^{(2)}_{xyx}$:

$$\begin{aligned}
\chi^{(2)}_{xyx} &= \sum_{lmn} \chi^{(2)}_{lmn}(\hat{x}\cdot\hat{l})(\hat{y}\cdot\hat{m})(\hat{x}\cdot\hat{n}) \\
&= \chi_{aaa}(\hat{x}\cdot\hat{a})(\hat{y}\cdot\hat{a})(\hat{x}\cdot\hat{a}) + \chi_{abb}(\hat{x}\cdot\hat{a})(\hat{y}\cdot\hat{b})(\hat{x}\cdot\hat{b}) + \chi_{bba}(\hat{x}\cdot\hat{b})(\hat{y}\cdot\hat{b})(\hat{x}\cdot\hat{a}) \\
&\quad +\chi_{bab}(\hat{x}\cdot\hat{b})(\hat{y}\cdot\hat{a})(\hat{x}\cdot\hat{b}) \\
&= -\chi_{aaa}\cos^2\phi\sin\phi - \chi_{aaa}\cos^2\phi\sin\phi - \chi_{aaa}\cos^2\phi\sin\phi + \chi_{aaa}\sin^3\phi \\
&= -\chi_{aaa}\sin(3\phi) \qquad \text{(A.12)}
\end{aligned}$$

Completing the calculation, finally we arrive to the final form of d_{im},

$$d_{im} = \begin{pmatrix} d_{11}\cos(3\phi) & -d_{11}\cos(3\phi) & 0 & 0 & d_{15} & d_{11}\sin(3\phi) \\ d_{11}\sin(3\phi) & d_{11}\sin(3\phi) & 0 & d_{15} & 0 & -d_{11}\cos(3\phi) \\ d_{31} & d_{31} & d_{33} & 0 & 0 & 0 \end{pmatrix} \qquad \text{(A.13)}$$

The induced second harmonic polarization $P(2\omega)$ is given by,

$$P(2\omega) = \chi^{(2)}_{eff}E_j(\omega)E_k(\omega) = \chi^{(2)}_{ijk}E_j(\omega)E_k(\omega)F^S(\omega)F^S(2\omega) \qquad \text{(A.14)}$$

where $F^S(\omega)$ and $F^S(2\omega)$ are the Fresnel transmission tensors. These serve as constants, so to get the generalized symmetry forms we will ignore them for now. Inserting Eq. A.13,

$$\begin{pmatrix} P_x \\ P_y \\ P_z \end{pmatrix} = \begin{pmatrix} \chi_{xxx}cos(3\phi) & -\chi_{xxx}\cos(3\phi) & 0 & 0 & \chi_{xxz} & \chi_{xxx}\sin(3\phi) \\ \chi_{xxx}\sin(3\phi) & \chi_{xxx}\sin(3\phi) & 0 & \chi_{xxz} & 0 & -\chi_{xxx}\cos(3\phi) \\ \chi_{zxx} & \chi_{zxx} & \chi_{zzz} & 0 & 0 & 0 \end{pmatrix} \begin{pmatrix} E_x^2 \\ E_y^2 \\ E_z^2 \\ 2E_yE_z \\ 2E_xE_z \\ 2E_xE_y \end{pmatrix}$$

Under the assumption that for P output geometries (see Figure 1.8), $E_y = 0$,

$$\begin{aligned}
I_{PP} &= |P_x + P_z|^2 \\
&= B\,|c_1 - c_3\cos(3\phi)|^2 \qquad \text{(A.15)} \\
I_{SP} &= |P_y|^2 \\
&= B\,|d_1 + c_3\cos(3\phi)|^2 \qquad \text{(A.16)}
\end{aligned}$$

Under the assumption that for S output geometries (see Figure 1.8), $E_x = 0$ and $E_z = 0$,

$$\begin{aligned}
I_{SS} &= |P_y|^2 \\
&= B\left|c_3\sin^2(3\phi)\right| \qquad \text{(A.17)} \\
I_{PS} &= |P_x + P_z|^2 \\
&= B\left|c_3\sin^2(3\phi)\right| \qquad \text{(A.18)}
\end{aligned}$$

Appendix B
Additional LSMO/STO Reflectivity Data

B.1 Exponential Fits for Reflectivity Curves

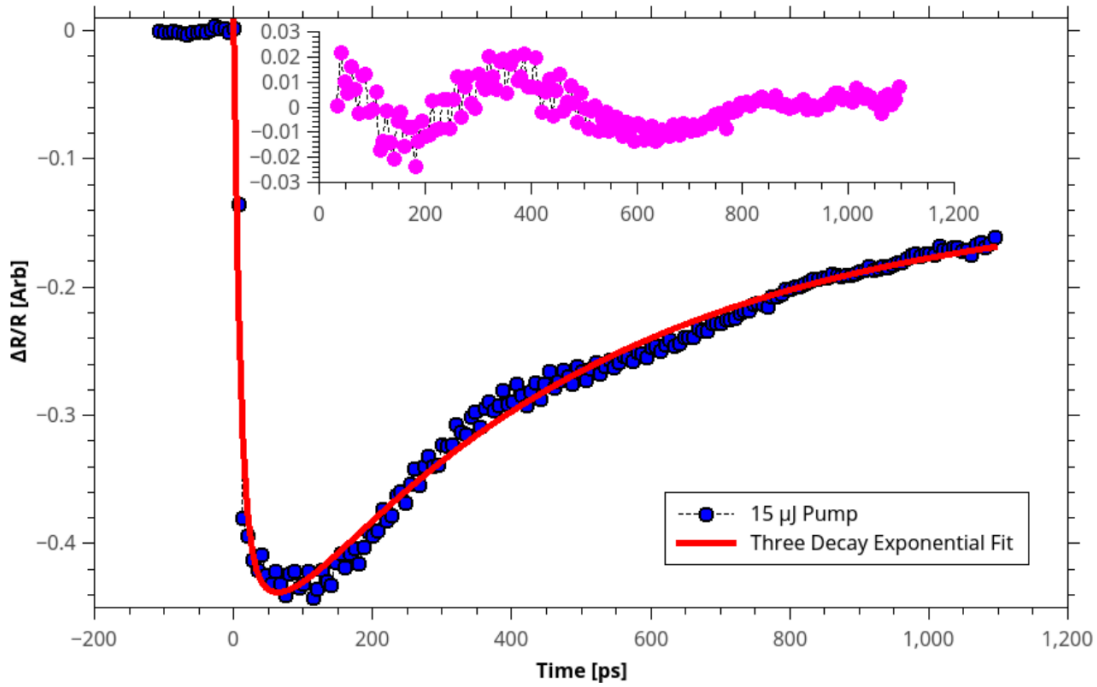

Figure B.1: $La_{0.67}Sr_{0.33}MnO_3/SrTiO_3$ reflectivity curve (blue circles) and fit (red line) with the pump power at 15 μJ. Inset is the fit residuals.

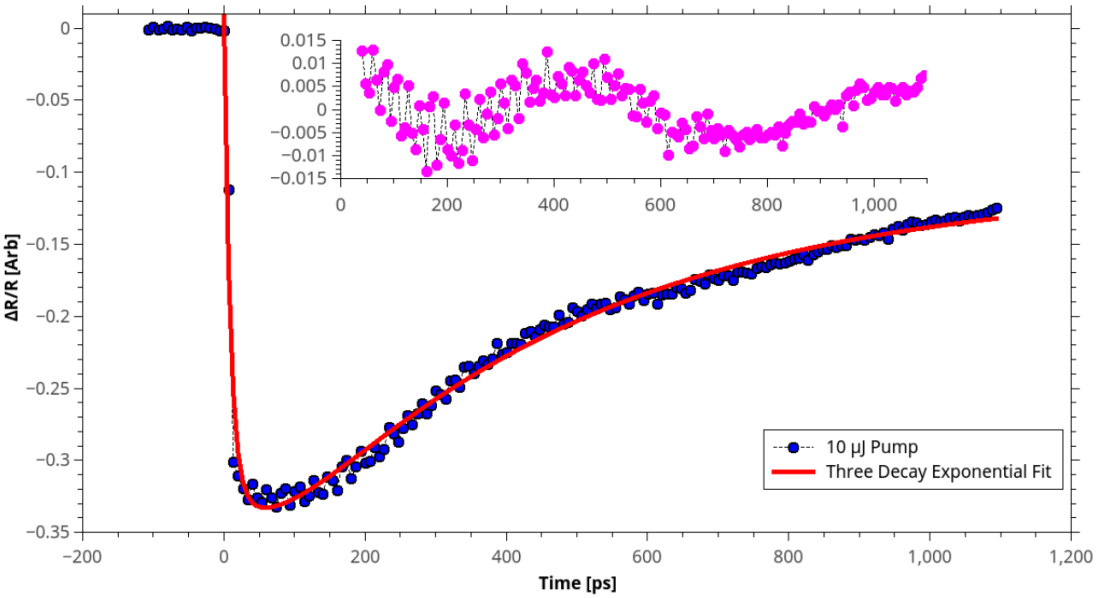

Figure B.2: $La_{0.67}Sr_{0.33}MnO_3/SrTiO_3$ reflectivity curve (blue circles) and fit (red line) with the pump power at 10 μJ. Inset is the fit residuals.

Vita

Joel Taylor grew up in Slidell, Louisiana before beginning college at Louisiana State University. In 2013, he completed his bachelor's degree in Physics with a concentration in Mechanical Engineering. Immediately following undergrad, he started graduate school at Louisiana State University under the advising of Prof. Ward Plummer. He is expected to graduate with a Doctor of Philosophy in Physics focusing on condensed matter and nonlinear optics in August 2019. Joel's recreational interests include reading, traveling, playing piano, and spending time with his close friends and family.